Chemical investigations of spinel lithium manganese oxides.

Albadran, Jafar

Chemical Investigations of Spinel Lithium Manganese Oxides

By

Jafar Albadran B.Sc.

A thesis submitted for the Degree of Doctor of Philosophy to the University of Wales

Department of Chemistry
University of Wales Swansea
2004

To my parents

CONTENTS

DECLARATION

This work has not previously been accepted in substance for any degree and is not being concurrently submitted in candidature for any degree.

Signed ..... **(candidate)**

Date 15.6.04

This thesis is the result of my own investigations, except where otherwise stated.
Other sources are acknowledged by footnotes giving explicit references. A bibliography is appended.

Signed ..... (candidate)

Date 15.6.04

I hereby give my consent for my thesis, if accepted, to be available for photocopying and for interlibrary loan, and for the title and summary to be made available to outside organisations

Signed ..... (candidate)

Date 15.6.04

ACKNOWLEDGMENT

I would like to thank my supervisor, Dr. Kevin Gallagher, who broadened my understanding of research and I gratefully acknowledge the time, effort and dedication he has devoted to this work. Furthermore, I would like to acknowledge his support in keeping this work alive despite all odds. Unfortunately, he is not with us anymore to see the fruit of this work as he died before it could be finished.

I wish to express my sincere appreciation to my other supervisor, Dr. Chris Morley, who kindly agreed to take over and has continued to support me with excellent remarks during the preparation of this manuscript. Without his encouragement this work would never have come this far.

I am really grateful to the Chemistry Department as a whole and especially: John Lewis, Stan Szajda, Gareth Lewis. Thank you for all your help and support.

Finally, I take this opportunity to express my profound gratitude to my beloved parents, my brother Muneer, my wife Zaynab and all my friends for their support, patience and encouragement during the course of my studies.

ABBREVIATIONS

ccp	Cubic Close Packed
hcp	Hexagonal Close Packed
CFSE	Crystal Field Stabilisation Energy
CFT	Crystal Field Theory
B.D.H.	British Drug Houses
B.O.C.	British Oxygen Company
B.E.T.	Brunauer, Emmett, and Teller
G.P.R.	General Purpose Reagent
J.C.P.D.S.	Joint Committee on Powder Diffraction Standards
Q.C.P.E.	Quantum Chemistry Program Exchange
JCPDS-ICDD	Joint Committee on Powder Diffraction Standards - International Center for Diffraction Data
oct.	Octahedral
tet.	Tetrahedral
Tri.	Trigonal

Table of Tables

Table of Figures

SUMMARY

For rechargeable lithium batteries, the most widely used cathode material is $LiCoO_2$, which is gradually being replaced by other lithium metal oxides due to the high cost and toxicity of cobalt. Oxide members of the Li-Mn-O system present themselves as attractive replacement candidates which offer all the properties for good electrode materials in addition to their low cost and low toxicity.

Despite its limited practical capacity of about 120 mA h g^{-1}, $LiMn_2O_4$ is considered to be a very attractive cathode material, mainly due to its ease of manufacturing, low cost and environmental compatibility and it has started to appear in some commercial products. However, $LiMn_2O_4$ suffers from significant capacity fading upon cycling especially at high temperatures. Worldwide research efforts have been devoted toward the understanding of this class of oxides and to produce better materials for battery applications. The work presented in this thesis is part of this effort.

In this work, a preparation method has been developed to obtain a pure, single-phase, and high surface area spinel $LiMn_2O_4$. Characterisation of the product confirmed that it is a thermally stable, single-phase spinel $LiMn_2O_4$ with surface area of 7.6 m^2 g^{-1}. The relatively high surface area found for samples prepared during the course of this study indicates a positive step when compared with those prepared using other techniques.

Another member of the spinel family, λ-MnO_2, has been prepared by the topotactic extraction of lithium from the previously prepared $LiMn_2O_4$. The spinel λ-MnO_2 has further chemically reduced to yield the oxide hydroxide form of manganese. The manganese oxide hydroxide obtained above has not been reported before and has been designated λ-MnOOH to indicate the relationship to its precursor oxide. Both manganese oxides were thoroughly characterised using various analysis techniques. Surface area measurements of the oxides gave 6.3 and 11.2 m^2 g^{-1} for λ-MnO_2 and λ-MnOOH respectively.

Kinetic investigation of the oxidation of normal spinel $LiMn_2O_4$ by chemical extraction of Li^+ revealed` that the extraction process is diffusion-controlled with a diffusion coefficient of 3.35-3.66 x 10^{-7} cm^2 s^{-1} and activation energy of 34.81 – 40.22 kJ mol^{-1}. It was found that due to the low activation energy of reaction, Li^+ is the only diffusing cation in the system and the process is taking place using the lattice's tetrahedral interstitial sites.

The reversibility of the extraction of lithium from $LiMn_2O_4$ in aqueous solutions was investigated. It has been found that it is possible to re-introduce lithium ions into the Mn_2O_4 framework only if Mn^{2+} is present in the solution. It was confirmed by x-ray diffraction that the result of the insertion reaction is the spinel $LiMn_2O_4$.

Other members of the Li-Mn-O system were investigated. Various oxide members were obtained by varying the Li:Mn ratio of the reactants. Some oxide members were successfully synthesised by mixing stoichiometric amounts of Li_2CO_3 and Mn_2O_3. A method to prepare the electrochemically active $LiMnO_2$ was proposed. The oxide was positively identified as orthorhombic $LiMnO_2$ with unit cell dimensions a = 2.790 Å, b = 5.614 Å and c = 4.564 Å. Other oxide members were prepared and characterised by means of x-ray diffraction and thermal analysis techniques.

Introduction

1.1 Introduction

Batteries are one of the most important objects in our everyday lives. The first evidence of batteries comes from archaeological digs in Baghdad, Iraq. This first "battery" was dated to around 250 B.C. and is suggested to have been used in simple operations like electroplating. What is known as the "Baghdad Battery" was constructed from a clay jar containing a copper tube, an iron rod, and some crumbling pieces of bitumen. Electricity was generated using a replica of the above construction when the jar was filled with vinegar or wine [1].

Batteries were re-invented much later by a man named Alessandro Volta (1745-1827) using copper and zinc electrodes. That was followed by the construction of the lead acid battery, which was invented by Planté in 1859. By 1866, Georges Leclanché, a French engineer, patented a new system, using the zinc/manganese oxide in his cell construction.

It was Carl Gassner of Mainz who is credited with constructing the first commercially successful "dry" cell in 1881. Other cell types followed like Ni-Cd which was invented by Jungner in 1899, sodium-sulphur by Yao and Kummer in 1966, lithium primary cells in the 1960's, leading to the present day technology of Ni-MH which appeared in the early 1980's and Li-ion secondary cells which started to appeare in the early 1990's [2].

Batteries exist in primary and secondary designs. Primary batteries are designed so the reactions at the electrodes are not reversible and are therefore discarded after one discharge. On the other hand, secondary batteries are designed so the reactions at the electrodes are reversible and the cells are rechargeable.

Batteries are constructed from three main components: cathodes where the reduction reaction occurs, anodes where the oxidation reaction occurs, and an ion conducting and electronic insulator known as the electrolyte.

The more popular and effective technologies developed over the last 20 years are nickel-based cells, lithium-based cells, along with a few less well-known fast-developing battery technologies. Lithium batteries are ideal for many different applications. They are suitable for any application that requires high voltage and a small package.

For rechargeable lithium non-aqueous batteries, the most widely used cathode material is $LiCoO_2$ [3] which due to its high cost, is being slowly replaced by other lithium containing materials like $LiNiO_2$ [4] and spinel $Li_xMn_2O_4$ [5, 6, 7].

The above metal oxides are known as insertion compounds. An insertion compound is a solid host network incorporating guest ions that can move freely between sites in the host network. The guest ion also can be removed from the host network thus varying the guest ion concentration within the electronic and ionic conducting host material.

Oxide members of the Li-Mn-O system present themselves as attractive candidates that offer all the properties necessary for a good host compound in addition to their low cost and low toxicity. These materials have been given a great deal of attention worldwide and are still being investigated and developed to be used in the future production of lithium ion cells. In the next few sections, reactions in solids will be described and some interesting and relevant solid systems will be reviewed.

1.2 Solid State Reactions

The study of reactions in solids is an important aspect of solid state chemistry, as it underlies many processes in nature and in industry. Although it is now well known that structure and crystal imperfection play an important part in the chemical reactivity of solids, their role is not well understood. A better understanding would benefit many applications of solid state chemistry. One application of great interest is the synthesis of new solid materials.

Solid state reaction depends to a large extent on the arrangement of the chemical constituents in crystals, indeed the crystal structure and defect structure of solids is often more important than the intrinsic chemical reactivity of the constituents. This feature of solid state reactions is typical of topochemical and topotactic reactions, which will be exploited in this work.

The term 'topotactic' is often used to denote the continuity of the structure during changes in composition or symmetry. Bernal [8] describes the topotactic transition as the transformation of the crystalline material into another by internal atomic displacement, with the loss or gain of part of the material, so that the majority of the atomic positions in the original and in the transformed material are substantially the same, and there is agreement, in the dimensions, between the initial and final lattices. If these conditions are satisfied, the transformation can be described as topotactic.

Solid state reactions could be grouped into the following categories.

- Solid decomposition and polymerisation.

- Solid-gas reaction, as in the oxidation of solids by air.
- Solid-solid reaction, as in the synthesis of complex oxides from simple components.
- Solid-liquid reaction, as in intercalation.
- Reactions confined to solid surfaces.

The above solid state reactions could involve one or more elementary steps. These steps include: (i) adsorption and desorption of gaseous or liquid species on the solid surface; (ii) nucleation of a new phase; (iii) transport phenomena through solids.

External factors, e.g. temperature, ambient atmosphere, pressure etc., also have an effect on solid state reactions. It is well known that solid-solid reactions are favoured by a small particle size as the reactivity increases with increasing surface area in contact. The nature of the atmosphere can play a significant role on reactivity if the gas is involved in an exchange reaction with the solid; the formation of a spinel such as $LiMn_2O_4$ is favoured in the presence of air rather than nitrogen, as can be seen in Chapter 3.

In most cases, the product structure differs from that of the initial material, and often decides the route and the rate of reaction. There are many systems, in which the low and high oxidation state oxides are structurally related to an extent that the phase boundary between them becomes undefined or non-existent. One such system is that of iron and oxygen, which contains several oxides in various oxidation states.

1.3 Mixed Metal Oxide Systems

Metal/oxygen systems can adopt a large number of arrangements, starting from the simple AO species to the very complex forms of mixed metal oxides. In the next sections we are going to discuss one oxygen system, namely mixed metal oxides.

Mixed metal oxides have a number of important technological applications. The simplest of these mixed metal oxides has the formula ABO_3 (e.g. $FeTiO_3$). Many mixed metal oxides can be prepared by reacting finely divided and well-mixed powders of the component oxides at high temperatures to allow the gradual diffusion of ions into each other's lattices, this being the well known sintering process.

We can describe the mixed metal oxides as a lattice of closed packed oxide ions with two or more different kinds of metal ions occupying tetrahedral or octahedral holes depending on the metal type and the oxide packing arrangement (ccp, hcp). There are three important mixed oxide structures: perovskite, ilmenite and spinel.

1.3.1 The Perovskite Structure ABO_3

This structure is named after the mineral perovskite $CaTiO_3$. It has an unusual cubic close-packed lattice of oxygen and calcium ions. The very small Ti^{4+} ions occupy the octahedral holes, within which they have some freedom of movement. This structural type requires that the sum of the charges of A and B ions be 6+ and that they be different in size, e.g. $LiNbO_3$. The A atom (Ca) occupies the centre of the unit cell and is co-ordinated to eight B atoms (Ti) at the corners and to twelve oxygens at the midpoints of the cell edges, as can be seen in Figure 1.1.

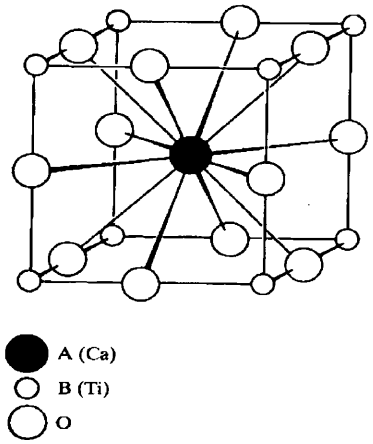

Figure 1.1 The perovskite structure for compounds ABO_3 such as $CaTiO_3$ [9].

1.3.2 The Ilmenite Structure ABO_3

This structure can be found in oxides of the formula ABO_3 when A and B have the same size and a total charge of 6+. The mineral ilmenite $Fe^{2+}Ti^{4+}O_3$ is the prototype compound of this group and has a structure similar to that of corundum. Ilmenite has a hcp array of oxygen atoms and the metal ions occupy a third of the octahedral holes in alternate layers.

1.3.3 The Spinel Structure AB_2O_4

The spinels have the general formula AB_2O_4, named after the mineral spinel $MgAl_2O_4$, where A= Mg^{2+} and B= Al^{3+}. The unit cell contains 32 oxide ions in an almost perfect cubic close-packed array. The overall formula is $A_8B_{18}O_{32}$, so 64 tetrahedral sites and 32 octahedral sites will be generated in the unit cell. If the eight A atoms occupy the

tetrahedral sites, and the sixteen B atoms are placed in the octahedral holes, the structure is that of a normal spinel. A unit cell is illustrated is Figure 1.2.

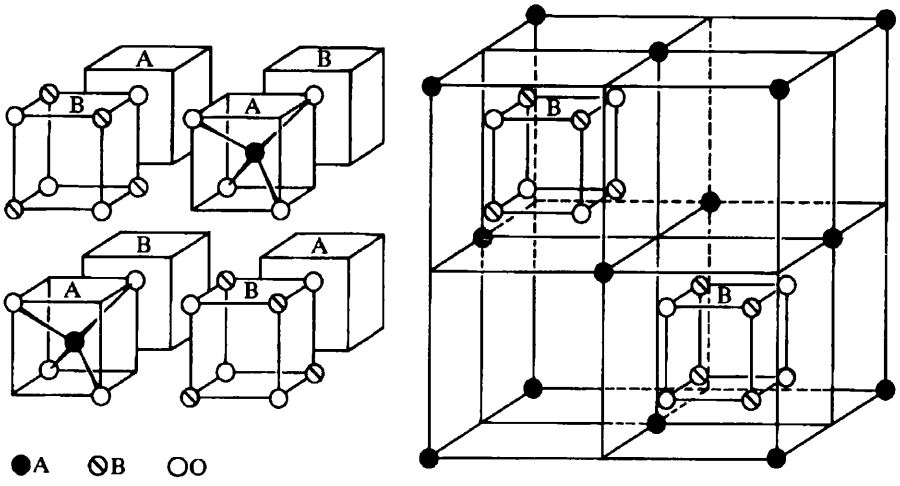

Figure 1.2 The spinel structure, AB_2O_4.

The structure can be thought of as eight octants of alternating AO_4 tetrahedra and B_4O_4 cubes as shown in the left-hand diagram. The O atoms have the same orientation in all eight octants and so build up into a face-centred cubic lattice of 32 ions which co-ordinate A tetrahedrally and B octahedrally. The four A octants contain four A ions and the four B octants sixteen B ions. The unit cell is completed by an encompassing face-centred cube of A ions (•) as shown in the right-hand diagram; this is shared with adjacent unit cells and comprises the remaining four A ions in the complete unit cell $A_8B_{16}O_{32}$. The location of two of the B_4O_4 cubes is shown for orientation.

The spinel structure can be found in different charge combinations depending on the cations present. The possible charge combinations are listed below [10].

2,3	as in	$MgAl_2O_4$
2,4	as in	Mg_2TiO_4
1,3,4	as in	$LiMn_2O_4$
1,3	as in	$Li_{0.5}Al_{2.5}O_4$
1,2,5	as in	$LiNiVO_4$
1,6	as in	Na_2WO_4

In an inverse spinel, the formula can be written as $B(AB)O_4$. This arrangement indicates that half of the B^{3+} ions occupy tetrahedral sites, and the remaining half will occupy the octahedral sites together with the A^{2+} ions. Examples of this type include Fe_3O_4, $MgFe_2O_4$ and $ZnFe_2O_4$. The formulae for normal and inverse spinels can thus be written as:

$$[A^{2+}]_t\,[B^{3+}]_o\,O_4 \qquad\qquad [B^{3+}]_t\,[A^{2+}\,B^{3+}]_o\,O_4$$

where t and o represent tetrahedral and octahedral sites.

Table 1.1 Estimated values of Crystal Field Stabilisation Energies (kJ mol^{-1}) for transition metal oxides [11, 12].

Ion		Octahedral CFSE	Tetrahedral CFSE
Sc^{3+}	d^0	0	0
Ti^{3+}	d^1	87.4	58.5
Ti^{2+}, V^{3+}	d^2	160.1	106.6
Mn^{4+}, Cr^{3+}, V^{2+}	d^3	224.5	66.9
Mn^{3+}, Cr^{2+}	d^4	135.4	40.1
Mn^{2+}, Fe^{3+}	d^5	0	0
Co^{3+}, Fe^{2+}	d^6	49.7	33.0
Co^{2+}	d^7	92.8	61.9
Ni^{2+}	d^8	122.1	35.9
Cu^{2+}	d^9	90.3	26.8
Zn^{2+}	d^{10}	0	0

The different distribution of cations between tetrahedral and octahedral sites may be explained on the basis of Crystal Field Stabilisation Energy (CFSE). Dunitz and Orgel [12] calculated CFSE's for transition metal ions in both octahedral and tetrahedral sites on the basis of spectroscopic measurements, which gave good agreement with observations. Table 1.1 shows the CFSE's for some oxides of the transition metal ions.

Table 1.1 reveals that, for d^0, d^5 and d^{10} ions such as Sc^{3+}, Mn^{2+}, Fe^{3+}, Zn^{2+}, the crystal field stabilisation energy is zero for both configurations. For many other trivalent ions, e.g. V^{3+} (d^2), Cr^{3+} (d^3), and Mn^{3+} (d^4) the preference for octahedral co-ordination is governed by crystal field stabilisation energy, so that 2,3 spinels with these ions will be normal. When divalent ions, e.g. Fe^{2+} (d^6), Co^{2+} (d^7), and Ni^{2+} (d^8) associate with

spherically symmetrical trivalent cations, their additional octahedral crystal field stabilisation energy sometimes overcomes the Madelung factor and results in the divalent ions occupying octahedral sites in an inverse spinel, e.g. $NiFe_2O_4$ and $CoFe_2O_4$.

The use of crystal field stabilisation energy is limited to systems with asymmetric d orbital occupancy, so structures having only ions with d^0, d^5 and d^{10} configurations are excluded. There are about 187 known spinels, mainly oxides, but also including some chalcogenides, halides and cyanides. Of these, there are 80 spinels containing ions with asymmetric d–electron configurations, in which the octahedral/tetrahedral occupancy can be predicted using the CFSE model. Another scheme is needed to explain this phenomenon for the remainder.

Prediction based on a structure map using the s and p orbital pseudopotential radii for the metals A and B as indices was introduced, as can be seen in Figure 1.3 [13, 14]. Using these indices gave a good separation between normal and inverse structures. The model has four normal structures falling within the inverse structure region, two of them being very poorly characterised systems. Mixtures of normal and inverse structures are found on the borderlines between the well-defined regions. This scheme concludes that the electronic demands of the valence s and p orbitals play the main role in deciding the co-ordination number. When the driving force for one arrangement is about the same as for the other (near the boundary region), d orbital effects becomes the deciding factor. If we neglect the spinel examples on the borderline, which CFT can treat, the structure map model has a success rate of 98 % [13].

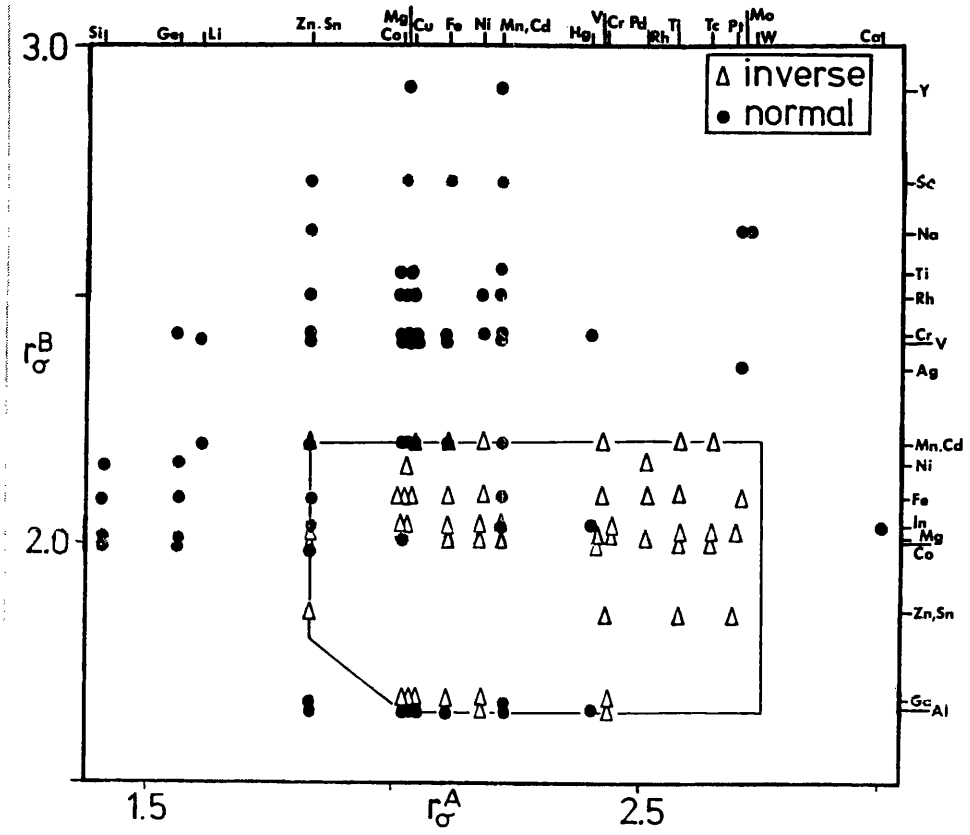

Figure 1.3 Structure map for the spinels using the pseudopotential radii combination r^A_σ and r^B_σ indices [13].

1.4 Spinel Manganese Oxides

To have a clear view of the lithium manganese oxide spinel system, an isothermal slice of the ternary Li-Mn-O phase diagram that relates specifically to the position of phases with spinel, defect-spinel and rock salt structures, is shown in Figure 1.4.a. An enlarged section of the shaded region of the diagram is given in Figure 1.4.b [15]. Stoichiometric and defect spinel phases in the Li-Mn-O system are located within the Mn_3O_4-$Li_4Mn_5O_{12}$-λ-MnO_2 triangle in Figure 1.4.

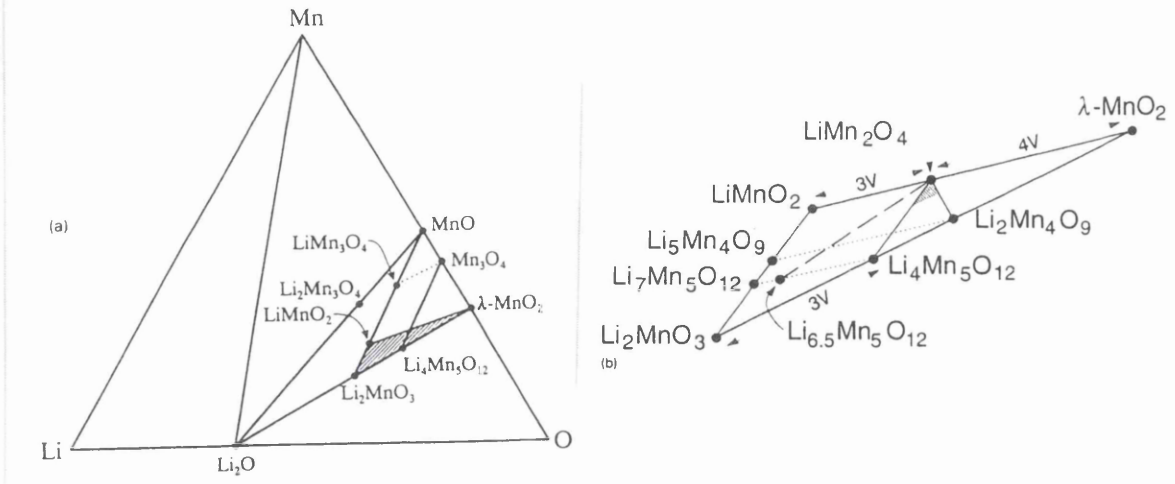

Figure 1.4 (a) An isothermal slice of the ternary Li-Mn-O phase diagram at 25 °C; (b) an enlarged view of the shaded triangle of the phase diagram [15].

Non-stoichiometric spinel phases are represented by the general formula $Li_xMn_{3-x}O_4$ ($0 \leq x \leq 1.33$) and they can be found on the line between Mn_3O_4 ($x = 0$) and $Li_4Mn_5O_{12}$ ($x = 1.33$) [16]. Spinels with the composition AB_2O_4 are located on the same line, and can be represented by the formula $Li_{1+x}Mn_{2-x}O_4$ ($0 \leq x \leq 0.33$). The position of these spinels is between $LiMn_2O_4$ ($x = 0$) and $Li_4Mn_5O_{12}$ ($x = 0.33$) [15].

Manganese oxide defect spinels, $Mn_{3-x}O_4$ ($0 \leq x \leq 1$) are located between Mn_3O_4 and λ-MnO_2. Lithium manganese oxide defect spinels, $Li_2O.yMnO_2$ ($y \geq 2.5$), can be found on the line between $Li_4Mn_5O_{12}$ and λ-MnO_2 [16]. Also lithium manganese oxide defect spinels are found on the tie line between $LiMn_2O_4$ and $Li_2Mn_4O_9$, and can be represented by the formula $Li_{1-x}Mn_{2-2x}O_4$ ($0 \leq x \leq 0.11$).

The marginally lithiated compounds are represented by the shaded triangle in Figure 1.4b, and located within $LiMn_2O_4$-$Li_{1.10}Mn_{1.90}O_4$-$Li_{0.97}Mn_{1.94}O_4$ boundaries, in which the average manganese oxidation state is between 3.5 and 3.63 [15].

In the following sections, the spinel arrangements of interest to this work are described in more detail.

1.4.1 Stoichiometric Spinel $LiMn_2O_4$

The most important technological application of spinels is their use as cathode materials in batteries. Secondary lithium batteries have been studied for the past two decades because they exhibit the highest specific energy among the rechargeable batteries. The use of lithium metal in these batteries prevented their widespread acceptance in the market place. The hazard involved in using lithium metal in batteries has directed the research towards the development of so-called "rocking chair lithium" or "lithium ion" rechargeable batteries [17]. The most promising materials for the cathode in "lithium ion" batteries are $LiCoO_2$ [3], $LiNiO_2$ [4], and spinel $Li_xMn_2O_4$ [5, 6, 7].

$Li_xMn_2O_4$ offers several advantages in terms of low cost, easy preparation and lack of toxicity [5]. It also has a high cell voltage, long shelf life, and a wide operating temperature [16]. The cubic spinel $LiMn_2O_4$ has a combination of other properties, which makes it a very attractive material for various electrochemical devices. These properties include a relatively high diffusion coefficient for lithium ions, a high redox potential and low solubility in aprotic solvents [18].

$LiMn_2O_4$ was first prepared by Wickham and Croft [19] by the solid-state reaction of Li_2CO_3 and Mn_2O_3 in the molar ratio 1:2 at 800-900 °C. $LiMn_2O_4$ has the space group Fd3m and it is isostructural with the mineral spinel $MgAl_2O_4$, with lithium ions occupying the tetrahedral 8a sites and manganese ions the octahedral 16d sites. The oxygen ions, which are cubic-closed packed, occupy the 32e positions. This means that $LiMn_2O_4$ has a normal 1,3,4 spinel structure, as can be seen in Figure 1.2.

The properties of the spinel $LiMn_2O_4$ depend largely on the preparation conditions, i.e. firing temperature, pre-heat treatment, the starting materials, and the Li/Mn molar ratio [20, 21, 22, 23, 24, 25, 26]. Samples with low levels of by-products and high surface area are favourable for use as cathode materials, since cells with high surface area cathode materials have low self-discharge values through spinel dissolution and electrolyte decomposition [27]. Besides the classical firing technique, $LiMn_2O_4$ has been prepared with a high surface area of 9.7 $m^2 g^{-1}$ using a wet-chemical technique by reacting lithium acetate and manganese acetate in methanol [28]. Chen *et al.* [29] showed that the lithium ion diffuses ten times faster in $LiMn_2O_4$ prepared using the wet-chemical method, compared to samples prepared using solid state reactions. $LiMn_2O_4$ has also been prepared using the Pechini process, which offers a high purity product with good stoichiometry at low temperatures [30, 31].

The spinel $LiMn_2O_4$ has been given a great deal of attention in the past few years. This is reflected in the number of methods that have been developed to prepare this oxide. The name of the method usually echoes the type of process used to prepare the oxide such as the Dynamic Process method [32], the mechanical alloying method [33], and the combustion method [34]. Other methods are named according to the way the sample is

applied to form the cathode such as the pulsed laser deposition method [35], the microwave synthesis method [36], the electrostatic spray deposition (ESD) method [37], and the ultrasonic spray pyrolysis method [38].

In this work, a method has been developed to prepare $LiMn_2O_4$ with high surface area (7.6 m^2 g^{-1}) using Li_2CO_3 and Mn_2O_3. The product was examined by x-ray diffraction and found to have the cubic spinel structure with unit cell parameter a = 8.24 Å. The thermal properties of the spinel $LiMn_2O_4$ were also investigated and it was found be to thermally stable at temperatures up to 700 °C. The oxide obtained by this method was used as a precursor for the study of the oxidation/reduction processes of the spinel $LiMn_2O_4$, and the preparation of λ-MnO_2 (see Chapter 3).

1.4.2 Defect Spinel λ-MnO_2

The other important member of the spinel family is λ-MnO_2. This novel form of manganese oxide is obtained by the extraction of lithium from $LiMn_2O_4$ and usually written $Li_{1-x}Mn_2O_4$ ($0 < x < 1$). It has attractive electrical properties similar to those of the parent oxide $LiMn_2O_4$. λ-MnO_2 was first described by Hunter [39] and its existence confirmed by Mosbah *et al.* [40]. Hunter found that when a sample of $LiMn_2O_4$ was treated with mildly acidic solution (H_2SO_4, pH = 2), the blue-black solid remained, but with a weight loss of approximately 29% from the starting material. Chemical analysis revealed that all the lithium had been removed [39], and powder neutron diffraction results indicated that oxides, λ-MnO_2 and $LiMn_2O_4$, have the cubic spinel structure with unit cell parameters a = 8.0639(3) Å and a = 8.2468(2) Å respectively [41].

Thackeray *et al.* [42, 43] demonstrated for the first time that $Li_{1-x}Mn_2O_4$ ($0 \leq x \leq 1$) could be prepared electrochemically by cycling a $LiMn_2O_4$-containing electrode versus a lithium reference electrode. Later Ohzoku *et al.* [44, 45] and Berg *et al.* [46, 47] reported a good electrochemical reversibility of $Li_{1-x}Mn_2O_4$ ($0 \leq x \leq 1$) and found that the electrochemical oxidation of $LiMn_2O_4$ proceeds topotactically to form λ-MnO_2.

The topotactic (chemical and electrochemical) extraction of lithium ions from $LiMn_2O_4$ causes the unit cell to 'shrink'. The product λ-MnO_2 has the spinel structure with the same framework $[Mn_2]O_4$ except that the tetrahedral 8a sites are empty, as can be seen in Figure 1.5.

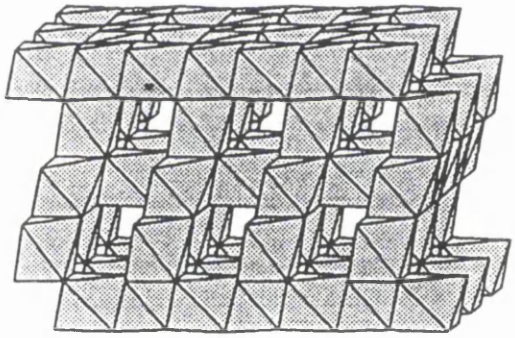

Figure 1.5 The $[B_2]O_4$ spinel framework [48].

Within the spinel $[B_2]O_4$ framework, the interstitial space represents a network of tetrahedral 8a and surrounding octahedral 16c sites that offers a 3D conduction pathway for lithium ions which remains intact for both lithium insertion and extraction over the range $Li_xMn_2O_4$ ($0 \leq x \leq 1$) [16].

In the present study, λ-MnO_2 has been prepared chemically by the acid treatment of $LiMn_2O_4$. The product was examined using x-ray diffraction techniques and found to have the cubic spinel structure with unit cell parameter a = 8.08 Å, a reduction of about 2% from that for $LiMn_2O_4$. The composition of λ-MnO_2 was determined by means of thermal analysis and found to be $MnO_{1.99}$, close to theoretical value MnO_2. This work is described in Chapter 4.

The chemical oxidation / reduction (lithium extraction / insertion) process for $LiMn_2O_4$ was investigated by means of the measurement of lithium concentrations diffused to solvent and residual in the solid during and after the oxidation process. The results are reported in Chapters 5.

In order to understand and interpret the changes that occur during the oxidation / reduction process, we need to review Fick's [49] first and second laws of diffusion.

The first law states that the rate of transfer of the diffusing species through a unit cross-sectional area is proportional to the concentration gradient, measured normal to the section, i.e.

$$J = -D\left(\frac{\partial c}{\partial x}\right)$$

where J is the rate of transfer per unit area of the section; c is the concentration; x is the space co-ordinate measured normal to the section. D is called the diffusion coefficient.

Fick's second law states that the rate of change of concentration with time is proportional to the rate of change of concentration with distance, expressed as follows:

$$\frac{\partial c}{\partial t} = \frac{\partial}{\partial x}(D\frac{\partial c}{\partial x})$$

with symbols as defined above.

If the diffusion coefficient is independent of distance, the above equation may be expressed as follows:

$$\frac{\partial c}{\partial t} = D\frac{\partial^2 c}{\partial x^2}$$

where, again, the symbols are as defined above, and the equation is for diffusion in one dimension.

Solutions to the above equations can be found in standard texts such as Carslaw and Jaeger [50], and Crank [51] for a wide variety of boundary conditions. These are typically defined by solid shape (e.g. spheres, cylinders, planes, sheets, etc.), variations in concentration (constant, discontinuous, oscillating, etc.), and diffusion coefficient (concentration dependent, time dependent, discontinuous, etc.). An explanation of the application of Fick's second law to the study of lithium diffusion in $LiMn_2O_4$ is presented in Chapter 5.

The diffusion coefficient (D) for lithium diffusion in $LiMn_2O_4$ was found by the technique introduced in Chapter 5 to be 2.01×10^{-9} cm^2 s^{-1}. Table 1.2 lists some diffusion

coefficients of lithium in $LiMn_2O_4$ found using the Galvanostatic Intermittent Titration Technique (GITT), along with the preparation temperature of the sample investigated.

Table 1.2 The chemical diffusion coefficient of lithium ions in $LiMn_2O_4$.

Preparation temperature	**Diffusion Coefficient D, $cm^2 s^{-1}$**
The wet method [29]	$4.7\text{-}7.9 \times 10^{-8}$
Commercial [52]	$10^{-10} - 10^{-8}$
300 °C [29]	$3.3 \times 10^{-8} - 7.7 \times 10^{-7}$
450 °C [53]	4.9×10^{-9}
800 °C [54]	$0.7\text{-}3.4 \times 10^{-8}$
1100 °C [29]	6.0×10^{-10}
This work	2.01×10^{-9}

In this work, it was shown that lithium could be chemically re-inserted into the spinel λ-MnO_2 to form the spinel $LiMn_2O_4$ by reacting λ-MnO_2 with Li^+ ions in the presence of Mn^{2+} ions. The results of the above studies have been discussed in relation to the likely mechanism for the extraction/oxidation reaction of $LiMn_2O_4$.

1.4.3 Spinel λ-MnOOH

λ-MnOOH belongs to another class of mixed metal oxides namely metal oxide hydroxides. Metal oxide hydroxides have almost exclusively the formula M^{3+} O^{2-} $(OH)^-$ where M^{3+} may be Al, Fe, Mn, Co, V, Cr, Ga, Sc, Y, and In. The predominant influence on crystal structure in these compounds is the electrostatic lattice energy and the ligand configuration around the metal atom. The most stable configuration for these metal atoms is an octahedral arrangement of oxygen atoms (O^{2-} or OH^-) which results in the octahedron being the commonest sub-unit of the structure.

Hydrogen bonding is a major factor in deciding how these sub-units are organised and grouped together, except for β-FeOOH and some other compounds, where the hydrogen bond does not occur. The influence of the hydrogen bonds on these compounds leads to a variety of structures, many of which occur naturally as minerals, e.g., diaspore (AlOOH), lepidocrocite (FeOOH) and akaganeite (FeOOH) etc. Other structures such as the InOOH structure have been formed under laboratory conditions only.

Some oxide hydroxides exist in several crystallographic modifications, which may or may not occur in nature. It is useful to classify these metal oxides into two main groups: hydrogen bonded and non-hydrogen bonded metal oxide hydroxides.

1.4.3.1 Hydrogen Bonded Metal Oxide Hydroxides

Hydrogen bonded metal oxide hydroxides have four main crystal structures, and they are as follows.

a) The ∝-MOOH or Goethite Structure

The crystal structure of goethite (α-FeOOH) may be represented by double chains of edge-shared distorted octahedra of oxygen atoms, as shown in Figure 1.6. It has the orthorhombic crystal structure with a = 4.608, b = 9.956 and c = 3.021 Å, the unit cell having four formula units of FeOOH [55, 56].

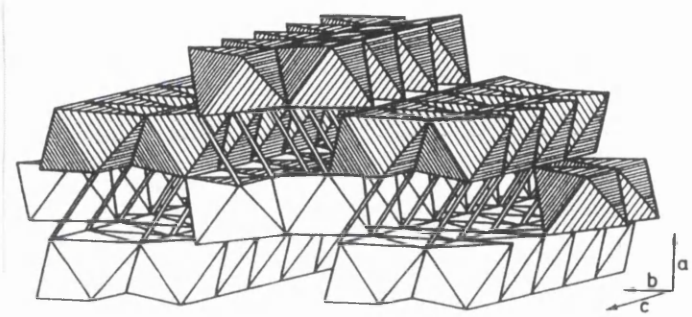

Figure 1.6 An idealised model of goethite (α-FeOOH) [55].

Lines connecting oxygen atoms on each side of the 1x2 tunnels represent hydrogen bonds. These hydrogen bonds between the hydroxyl ions and the oxide ions are 2.67 Å long forming a bioxide ion $[O—H\text{----}O]^{3-}$. It is thus similar to the bifluoride ion $[F—H\text{---}F]^-$ but unlike the bifluoride ion it is not symmetric so that the proton does not lie in the centre of the bond [57]. Other metal oxide hydroxides that have the goethite structure are diaspore (α-AlOOH) [58], α-ScOOH [59], bracewellite (CrOOH) [60], montroseite (α-VOOH) [61], and groutite (α-MnOOH) [62]. The manganese oxide hydroxide mineral (groutite) has unit cell dimensions of a = 4.560, b = 10.700 and c = 2.870 Å and a hydrogen bond length of 2.62 Å [62].

b) The γ-MOOH or Boehmite Structure

This group includes the minerals lepidocrocite (γ-FeOOH), manganite (γ-MnOOH), boehmite (γ-AlOOH) and γ-ScOOH [63].

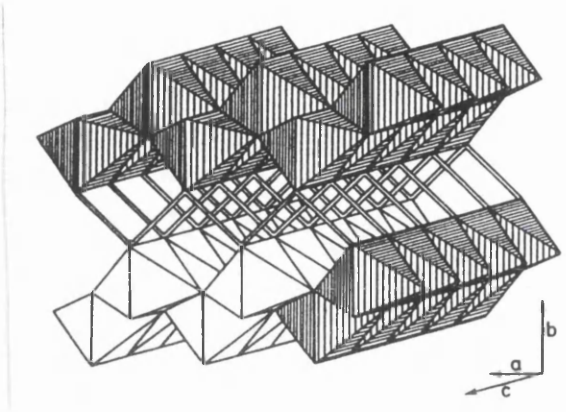

Figure 1.7 An idealised model of lepidocrocite [55].

The crystal structure of lepidocrocite (γ-FeOOH) has been determined by Ewing [64] who described it in terms of octahedrally co-ordinated iron atoms. The octahedral sub-units are joined by four common sides into double layered plates. The plates are parallel with infinite OH-OH zigzag chains of OH groups held together by hydrogen bonds [65]. Ewing assigned the crystal structure to the orthorhombic structure with the unit cell containing four formula units of FeOOH. Figure 1.7 shows the structure of lepidocrocite according to Ewing, with the lines corresponding to the hydrogen bonds. This structure was later confirmed by others [66, 67, 68]. The manganese oxide hydroxide (γ-MnOOH) has a unit cell with the dimensions a = 8.98, b = 5.28 and c = 5.71 Å [69].

c) The InOOH and CrOOH Structures

InOOH has a rutile-like structure with a hydrogen bond length of 2.58 Å between certain atoms. This structure has an orthorhombic unit cell with two formula units of InOOH [70]. Other examples of this structure are shown by β-CrOOH [71], VOOH, FeOOH [72] and ScOOH [73].

On the other hand, the CrOOH structure is known to have CdI_2-type layers, which are arranged so that the oxygen atoms of one layer are directly above the oxygen atoms in the next layer. The layers are held together by short hydrogen bonds of length 2.471 Å [74]. Other oxide hydroxides like CoOOH [75] and δ-FeOOH [76, 77] also display this structure. No manganese oxide hydroxide has been reported so far to have either of the above structures.

1.4.3.2 Non-hydrogen Bonded Metal Oxide Hydroxides

As we saw in the previous section, hydrogen bonding plays an important role in the structures of lepidocrocite, goethite etc. Some of the metal oxide hydroxides exist, however, without the need for hydrogen bonding. The best examples for this group are the mineral akaganite (β-FeOOH), YOOH, HoOOH and all other MOOH compounds with the metal ion having a $4f^n$ electronic configuration.

The structure of akaganeite (β-FeOOH) is analogous to that of hollandite (α-MnO_2) [78]. The iron-oxygen octahedra are connected together to form double chains parallel to the c axis, with two distinctive large channels per unit cell.

It was suggested that the structure would exist only in the presence of a halide ion (Cl^-, F) [79]. Although they are necessary for the formation of this modification, the halide ions were successfully removed from the tunnels without disturbing the structure [80]. Figure 1.8 shows the akaganeite structure before and after the removal of the chlorine ion.

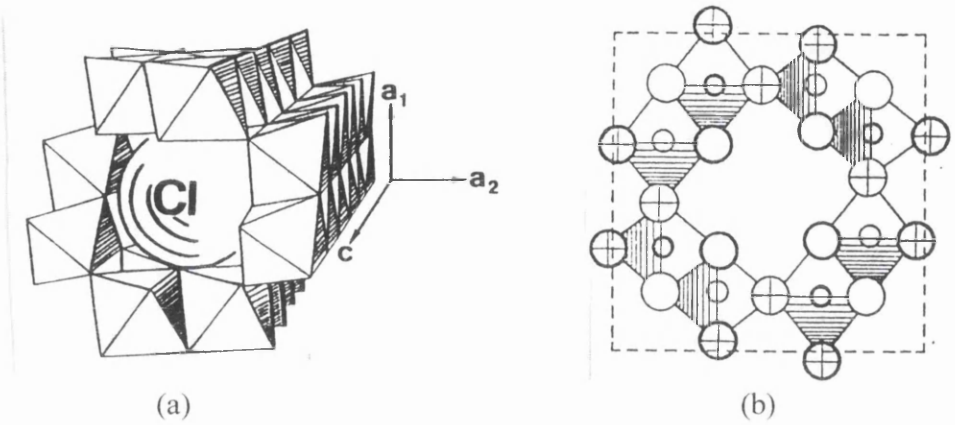

Figure 1.8 The crystal structure of akaganeite, (a) before the removal of the chloride ion [55] and (b) after [81].

Akaganeite (β-FeOOH) has a tetragonal unit cell with a = 10.48 and c = 3.023 Å and eight formulae of FeOOH per unit cell [9, 82, 83]. Szytula *et al.* [84] confirmed the above results and the absence of the hydrogen bond using neutron diffraction. No manganese oxide hydroxide has been reported so far to have the above structure.

The spinel manganese oxide hydroxide (λ-MnOOH) has been obtained in this work by the chemical reduction of λ-MnO_2 using cinnamic alcohol. The new form of manganese oxide hydroxide has been given the name "lambda" λ-MnOOH to distinguish it from the other forms of manganese oxide hydroxide and to show that it has been prepared via the oxide λ-MnO_2. X-ray examination showed that λ-MnOOH has retained the cubic spinel structure of the parent oxide with a slight increase in the size of the unit cell (a = 8.096 Å). The increase in unit cell dimension is believed to be the result of the formation of

some hydrogen bonds inside the 3D tunnels, and of the Jahn-Teller distortion resulting from the reduction of Mn^{4+} to Mn^{3+}. No indication was found in the scientific literature with regard to the formation of such an oxide hydroxide.

1.4.4 Other spinel members of the Li-Mn-O system

The cubic spinel $LiMn_2O_4$ is not the only compound that has received attention in the Li-Mn-O system. Other spinel compounds, e.g. $Li_4Mn_5O_{12}$ and $Li_2Mn_4O_9$, are found to have similar characteristics to those of $LiMn_2O_4$, with regard to their use as cathode materials for 'lithium ion' cells. They can be synthesised within a few hours at relatively low temperatures. The theoretical capacities of these materials as electrodes, for example $Li_4Mn_5O_{12}$ (0.163 Ampere hour gram^{-1} written as A h g^{-1}), and $Li_2Mn_4O_9$ (0.213 A h g^{-1}), are relatively higher than the capacity of $LiMn_2O_4$ (0.148 A h g^{-1}).

Spinel compounds can be disordered, either by cation mixing (inverse spinel) or by cationic or anionic nonstoichiometry (deficient spinels). Stoichiometric spinels $Li_4Mn_5O_{12}$ [15, 85, 86], $Li_2Mn_3O_7$ [86], and defect spinel $Li_2Mn_4O_9$ [15, 85, 87] have been prepared by solid state reactions of different stoichiometric amounts of lithium salts and manganese oxides and salts at moderately high temperatures (350-450 °C).

$Li_4Mn_5O_{12}$ and $Li_2Mn_4O_9$ are the end members of the system $Li_2O.yMnO_2$ ($2.5 \leq y \leq 4.0$). $Li_4Mn_5O_{12}$ is a stoichiometric spinel M_3O_4, where M is the total cation content in the sample, with the spinel notation $[Li]_{tet}$ $[Li_{0.33}$ $Mn_{1.67}]_{oct}$ O_4. The non-stoichiometric spinels $Li_{1+x}Mn_{2-x}O_4$ ($0 \leq x \leq 0.33$) could be represented, in terms of spinel notation, by the formula $[Li]_{8a}$ $[Mn_{2-x}$ $Li_x]_{16d}$ O_4. Thus increasing x in site 16d causes the manganese

ions to be replaced by lithium. This will decrease the lattice constant, and increase the manganese ion oxidation state to maintain charge neutrality until the x = 0.33 composition is reached, where the manganese has the tetravalent oxidation state [15]. Thackeray *et al.* [87] prepared $Li_4Mn_5O_{12}$ (y = 2.5) and $Li_2Mn_3O_9$ (y = 3) by mixing Li_2CO_3 and $MnCO_3$ powders in a Li:Mn ratio of 4:5 and 2:3 respectively. The mixtures were then heated in air at 400 °C. Gummow *et al.* [15] and Rossouw *et al.* [85] prepared $Li_4Mn_5O_{12}$ (y = 2.5) using a stoichiometric mixture of $LiOH.H_2O$, CMD (γ-MnO_2) and electrochemically prepared manganese dioxide (EMD). The mixtures were then heated in air at 400 °C.

$Li_2Mn_4O_9$ (y = 4.0) is a defect spinel $[Li_{0.89}\ \square_{0.11}]_{tet}\ [Mn_{1.78}\ \square_{0.22}]_{oct}\ O_4$ in which vacancies exist in both tetrahedral and octahedral sites of the structure. It has a stoichiometry M_2O_3, which is well known in defect spinels, e.g. γ-Al_2O_3 and γ-Fe_2O_3. Single phase $Li_2Mn_4O_9$ has been prepared by de Kock *et al.* [86] by reacting Li_2CO_3 and $MnCO_3$. The reactants were mixed in a 1:4 molar ratio and then heated at 400 °C for five hours.

Table 1.3 The cubic spinel compounds in the Li-Mn-O system.

Compounds	**Cell constant, a (Å)**	**Spinel notation**
λ-MnO_2 [86]	8.0445	$[\square_{1.0}]_{8a}[Mn_2]_{16d}\ O_4$
$LiMn_2O_4$ [16]	8.245	$[Li_{1.0}]_{8a}[Mn_2]_{16d}\ O_4$
$Li_2Mn_4O_9$ [86]	8.174	$[Li_{0.89}\ \square_{0.11}]_{8a}[Mn_{1.78}\ \square_{0.22}]_{16d}\ O_4$
$Li_2Mn_3O_7$ [87]	8.1605	$[Li_{0.85}\ \square_{0.15}]_{8a}[Mn_{1.74}\ \square_{0.26}]_{16d}\ O_4$
$Li_4Mn_5O_{12}$ [87]	8.1430	$[Li_{1.0}]_{8a}[Mn_{1.67}\ Li_{0.33}]_{16d}\ O_4$

X-ray and neutron diffraction studies of the above compounds revealed that they all have a cubic system with different site occupancy. Table 1.3 summarises the well-known

spinel compounds with their available data. In this work, some other members of the Li-Mn-O system were prepared. The main success of the method proposed is the preparation of the electrochemically active orthorhombic $LiMnO_2$ with unit cell dimensions a = 2.790 Å, b = 5.614 Å and c = 4.564 Å.

1.5 Conclusion

In the 20th century, electricity has become the key energy carrier and the engine for the growth of large industries and technologies in the whole world. Batteries in general and rechargeable ones in particular, are playing an important role in our time and indeed in the future. The demand for small and highly efficient rechargeable batteries is growing to power popular devices such as portable computers, phones etc. As the demand for such power sources is growing, the pressure to find efficient, cost effective, and environmentally friendly materials is mounting.

Over the past few years, various metal oxide systems have been investigated for their chemical and electrochemical properties: hence their use as cathode materials to satisfy the ever-growing demand for power sources. One of the promising systems is the Li-Mn-O system, and in particular its members with the spinel structure.

The use of various lithiated metal oxides such as $LiCoO_2$ and $LiNiO_2$ has led to the emergence of the Li-ion battery. Lithium manganese oxides are emerging as viable replacement cathode materials in Li-ion cell development. The importance of lithiated manganese oxides comes from the fact that they are cheap, easy to prepare, environmentally friendly and found to show superior electrochemical properties

compared to those of cobalt and nickel. In this thesis, some members of the Li-Mn-O system are investigated in order to contribute to the understanding of this class of materials.

1.6 Thesis objectives

Over the last decade, various materials have been introduced as cathodes for rechargeable batteries. However, one class of materials, which has dominated the research arena and lately found its way to the commercial market, is the lithiated manganese oxides. Despite all that effort, these materials have still not been fully understood and their behaviour not fully comprehended.

In Chapter three, spinel $LiMn_2O_4$ is prepared using a modified firing technique in order to achieve a single-phase oxide with high surface area. Thermal properties of the oxide are also explored in Chapter three. Defect spinel manganese oxide λ-MnO_2 is prepared by the acid treatment of $LiMn_2O_4$ and λ-MnOOH is prepared by the reduction of defect spinel λ-MnO_2 by cinnamic alcohol. Both procedures are discussed in Chapter four. Chapter five describes a kinetic study of the extraction of lithium from $LiMn_2O_4$. The study seeks to understand the mechanism by which lithium diffuses through the oxide into solution. A diffusion model is introduced. The extraction of lithium from the oxide is thought to be reversible. The possibility of inserting the extracted lithium back into the defect spinel λ-MnO_2 is presented in Chapter six. The study is focused on proving the possibility of the insertion reaction and establishing the best conditions for such a reaction. In Chapter seven, a method is developed to prepare other members of the Li-Mn-O system e.g. the orthorhombic $LiMnO_2$.

References

1 P. James and N. Thorpe, *Ancient Inventions*, Ballantine Books, New York (1994) p. 148.

2 D. Linden (Ed.), *Handbook of Batteries*, 2nd Edition, McGraw-Hill Inc., New York (1995).

3 T. Nagura and K. Tazawa, *Prog. Batteries Solar Cells*, **9**, 20 (1990).

4 J.R. Dahn, U. Sackenvon, M.R. Jukow, and H. Al-Janaby, *J. Electrochem. Soc.,* **137**, 2207 (1991).

5 J.M. Tarascon and D. Guyomard, *J. Electrochem. Soc.,* **138**, 2864 (1991).

6 D. Guyomard. and J.M. Tarascon, *J. Electrochem. Soc.*, **139**, 937 (1992).

7 J.M. Tarascon, D. Guyomard, and G.L. Baker, *J. Power Sources* , **43/44**, 689 (1993).

8 J.D. Bernal, *Schweiz. Arch. Angew. Wiss. U. Tech.*, **26**, 69 (1960).

9 L. Smart, and E. Moore, *Solid State Chemistry, an introduction*, Chapman & Hall, London (1992).

10 A.R. West, *Solid State Chemistry and its Applications*, Wiley, London (1987).

11 D. M. Adams, *Inorganic Solids, an introduction to concepts in solid state structural chemistry*, Wiley, London (1974) p.150.

12 J.D. Dunitz, and L.E. Orgel, *J. Phys. Chem. Solids*, **3**, 318 (1957).

13 J.K. Burdett, G.D. Price, and S.L. Price, *J. Am. Chem. Soc.,* **104**, 92 (1982).

14 H.F. Paulsen, N.A. Andersen, J.V. Andersen, H. Bohr, and O.G. Mouritsen, *Nature*, **349**, 594 (1991).

15 R.J. Gummow, A. de Kock, and M.M. Thackeray, *Solid State Ionics,* **69**, 59 (1994).

16 M.M. Thackeray, A. de Kock, M.H. Rossouw, and D. Liles, *J. Electrochem. Soc.,* **139**, 363 (1992).

17 Y. Xia, H. Takeshige, H. Noguchi, and M. Yoshio, *J. Power Sources,* **56**, 61 (1995).

18 V.I. Ezikyan, G.P. Ereiskaya, U.V. Ivanov, and A.M. Kolomoets, *Langmuir*, **25**, 795 (1989).

19 D. Wickham and W. Croft, *J. Phys. Chem. Solids*, **7**, 351 (1958).

20 A. Momchilov, V. Manev, A. Nassalevska, and A. Kozawa, *J. Power Sources*, **41**, 305 (1993).

21 J.M. Tarascon, W.R. Mckinnon, F. Coowar, T.N. Bowmer, G. Amatucci, and D. Guyomard, *J. Electrochem. Soc.,* **141**, 1421 (1994).

22 V. Manev, A. Momchilov, A. Nassalevska, and A. Sato, *J. Power Sources,* **54**, 323 (1995).

23 A. Momchilov, V. Manev, A. Nassalevska, and A. Kozawa, *J. Power Sources,* **43/44**, 551 (1993).

24 Q. Feng, Y. Miyai, H. Kano, and K. Ooi, *Langmuir*, **8**, 1861 (1992).

25 E. Oz, X.H. Hu, X.P. Ai, H.X. Yang and S.X. Li, *J. Power Sources*, **74**, 240 (1998).

26 M.G. Lazarraga, S. Mandal, J. Ibanez, J.M. Amarilla and J.M. Rojo, *J. Power Sources*, **115**, 315 (2003).

27 G. Pistoia and R. Rosati, *J. Power Sources,* **58**, 135 (1996).

28 T. Tsumura, A. Shimizu, and M. Inagaki, *J. Mat. Chem.*, **3**, 995 (1993).

29 L. Chen, X. Huang, E. Kelder, and J. Schoonmann, *Solid State Ionics*, **76**, 91 (1995).

30 W. Liu, G. C. Farrington, F. Chaput, and B. Dunn, *J. Electrochem. Soc.,* **143**, 879 (1996).

31 S.Y. Han and G.H. Kim, *J. Power Sources*, **88**, 161 (2000).

32 D.G. Fauteux, A. Massucco, J. Shi, and C. Lampe-Onnerud, *J. Appl. Electrochem.*, **27**, 543 (1997).

33 W.T. Jeong, J.H. Joo, and K.S. Lee, *J. Alloys and Compounds*, **358**, 294 (2003).

34 P. Kalyani, N. Kalaiselyi, and N. Muniyandi, *J. Power Sources*, **111**, 232 (2002).

35 I. Yamada, T. Abe, Y. Iriyama, and Z. Ogumi, *Electrochemistry Communications*, **5**, 502 (2003).

36 M. Nakayama, K. Watanabe, H. Ikuta, Y. Uchimoto, and M. Wakihara, *Solid State Ionics*, **164**, 35 (2003).

37 D. Shu, K.Y. Chung, W.I. Cho, and K.B. Kim, *J. Power Sources*, **114**, 253 (2003).

38 I. Taniguchi, C.K. Lim, D. Song and, M. Wakihara, *Solid State Ionics*, **146**, 239 (2002).

39 J. Hunter, *J. Solid State Chem.*, **39**, 142 (1981).

40 A. Mosbah, A. Verbaern, and M. Tounoux, *Mat. Res. Bull.*, **18**, 1375 (1983).

41 C. Fong, B.J. Kennedy and M.M. Elcombe, *Z. Kristallog.*, **209**, 941 (1994).

42 M.M. Thackeray, P. Johnson, L. de Picciotto, P. Bruce, and J. Goodenough, *Mat. Res. Bull.*, **19**, 179 (1984).

43 M.M. Thackray, L. de Picciotto, A. de Kock, P. Johnson, U. Nicholas, and K. Adendorff, *J. Power Sources*, **21**, 1 (1987).

44 T. Ohzuku, H. Fukuda, and T. Hirai, *Chem. Express,* **2**, 543 (1987).

45 T. Ohzuku, M. Kitagawa, and T. Hirai, *J. Electrochem. Soc.,* **137**, 769 (1990).

46 H. Berg and J.O. Thomas, *Solid State Ionics,* **126**, 227 (1999).

47 H. Berg, H. Rundlov and J.O. Thomas, *Solid State Ionics*, **144**, 65 (2001).

48 R. J. Gummouw, D.C. Liles, and M.M. Thackeray, *Mat. Res. Bull.,* **38**, 1249 (1993).

49 A. Fick, *Ann. Phys.,* LP2, **170**, 59 (1855).

50 H.S. Carslaw and J.C. Jaeger, *Conduction of Heat in Solids*, Oxford University Press, Fair Lawn, NY (1959).

51 J. Crank, *Mathematics of Diffusion*, Oxford University Press, Fair Lawn, NY (1956).

52 M. Mohamedi, D. Takahashi, T. Itoh, and I. Uchida, *Electrochim. Acta,* **47**, 3483 (2002).

53 L. Chen and J. Schoonman, *Solid State Ionics*, **67**, 17 (1993).

54 M.Y. Saidi, J. Barker, and R. Koksbang, *J. Solid State Chem.,* **122**, 195 (1996).

55 U. Schwertmann, *Iron Oxides in the Laboratory*, VCH, NY (1991).

56 F.J. Ewing, *J. Chem. Phys.*, **3**, 203 (1935).

57 K.J. Gallagher and D.N. Philips, *J. Chem. Soc. Faraday Trans.*, **64**, 785 (1968).

58 W.R. Busing and H.A. Levy, *Acta Crystallogr.*, **11**, 798 (1958).

59 A.N. Christensen and S.J. Jensen, *Acta Chem. Scand.*, **21**, 121 (1967).

60 JCPDS files, 25-1497.

61 H.T. Evans, Jr. and M.E. Morse, *Am. Min.*, **40**, 8161 (1955).

62 L.S.D. Glasser and L. Ingram, *Acta Crystallogr.*, **B24**, 1233, (1968).

63 W.O. Milligan and J.L. McAtee, *J. Phys. Chem.*, **60**, 273 (1956).

64 F.J. Ewing, *J. Chem. Phys.*, **3**, 420, (1935).

65 K.A. Wickersheim and G.K. Korpi, *J. Chem. Phys.*, **42**, 579 (1965).

66 A. Oles, A. Szytula, and A. Wanic, *Phys. Status Solidi*, **41**, 173 (1970).

67 A.N. Chistensen, M.S. Lehmann, and P. Convert, *Acta Chem. Scand.*, **A32**, 87 (1978).

68 T. Murad, *Ph.D. thesis,* University of Wales Swansea (1985).

69 JCPDS files, 18-805.

70 A.N. Chistensen, R. Gronbak, and S.E. Ramussan, *Acta Chem. Scand.*, **18**, 1261 (1964).

71 A.N. Chistensen, P. Hansen, and M.S. Lehmann, *J. Solid State Chem.*, **19**, 299 (1976).

72 J. Chenavas, *J. Solid State Chem.*, **6**, 1 (1973).

73 A.N. Chistensen, *Mat. Res. Bull.*, **6**, 691 (1971).

74 A.N. Chistensen, P. Hansen, and M.S. Lehmann, *J. Solid State Chem.*, **21**, 325 (1977).

75 R.G. Delaplane, J.A. Ibers, J.R. Ferraro, and J.J. Rush, *J. Chem. Phys.*, **50**, 1920 (1969).

76 O. Muller, R. Wilson, and W. Krakow, *J. Mat. Sci.*, **14**, 2929 (1979).

77 T. Ishikawa, W.Y. Cai, and K. Kandori, *J. Chem. Soc. Faraday Trans.*, **88**, 1173 (1992).

78 A. Bystroem and A.M. Bystroem, *Acta Crystallog.*, **3**, 146 (1950).

79 A.F. Wells, *Structural Inorganic Chemistry*, Clarendon Press, Oxford (1975).

80 K.J. Gallagher, *Nature*, **226**, 1225 (1970).

81 J.D. Benal, D.R. Dasgupta, and A.L. MacKay, *Clay Miner. Bull.*, **4**, 415 (1959).

82 A.L. MacKay, *Miner. Mag.,* **32**, 545 (1960).

83 A.T. Howe and K.J. Gallagher, *J. Chem. Soc. Faraday Trans. I*, **71**, 22 (1975).

84 A. Szytula, M. Baland, and Z. Dimitrijevec, *Phys. Status Solidi,* **A3**, 1033 (1970).

85 M.H. Rossouw, A. de Kock, L.A. de Picciotto, M.M. Thackeray, W.I.F. David, and R.M. Ibberson, *Mat. Res. Bull.*, **25**, 173 (1990).

86 A. de Kock, M.H. Rossouw, L.A. de Picciotto, M.M. Thackeray, W.I.F. David, and R.M. Ibberson, *Mat. Res. Bull.*, **25**, 657 (1990).

87 M.M. Thackeray, A. de Kock, and W.I.F. David, *Mat. Res. Bull.,* **28**, 1041 (1993).

Experimental Methods

This chapter deals with the experimental techniques used in the course of this work, e.g. x-ray powder diffraction, thermal analysis, electron microscopy, FTIR & UV-VIS spectroscopy, atomic absorption spectroscopy, and surface area measurements. The procedures used for chemical analysis of manganese, lithium, aluminium and iron are described. This chapter also lists the chemicals used in this work with their source and degree of purity.

2.1 X-ray Powder Diffraction

X-ray powder diffraction analysis was carried out using a Nonius Guinier-De Wolff parafocusing camera mounted in the horizontal position and geometrically arranged so that diffracted reflections from the specimen converge to a line in space. The parafocusing condition and monochromatic radiation were obtained by diffracting radiation from a rectangular quartz crystal cut at an angle of 4½ ° to the $10\bar{1}1$ planes.

The camera has the ability to record the diffraction pattern in the front reflection region ($2\theta = 90°$) and also served to minimise the finite breadth of the diffraction lines, which is caused by the specimen thickness and the $K\alpha_1$-$K\alpha_2$ separation [1]. Figure 2.1 shows the layout of the camera. The camera can accommodate several tubes as an x-ray source for use with different samples depending on the mass absorption coefficient of the main element in the sample to be analysed. They can either be operated contiguously or switched off by a pre-set timer for up to 30 hours per cycle. For the x-ray work described here FeKα radiation was used and the exposure time was 13 hours.

The Guinier-deWolff camera has the ability to irradiate up to four samples simultaneously, these being supported on a metal frame by sellotape and held by bedacryl and toluene. The sellotape gives two broad and diffuse bands at d-values of about 4.1 and 4.5 Å. Bedacryl gave no noticeable pattern.

The film was 180 mm in length and 45 mm in breadth. The change in film size during processing was negligible, but for more accurate readings, calibration was necessary, and for this purpose, 'Analar' potassium chloride (B.D.H.) was included as one of the samples in all this work.

To measure the d-values for identification purposes, a transparent perspex ruler was used. The ruler is calibrated to a graduated scale for the Guinier-de Wolff camera and for the particular radiation used. The intensities were estimated on a scale of 1 to 10 by giving the highest value to the strongest line, and estimating the strength of the other lines on this scale. For more accurate measurements, e.g. unit cell dimensions, unit cell volume etc., a ruler with accuracy to within ±0.01 mm was used to measure the spacing of the lines in mm which could then be converted to d-values in Å.

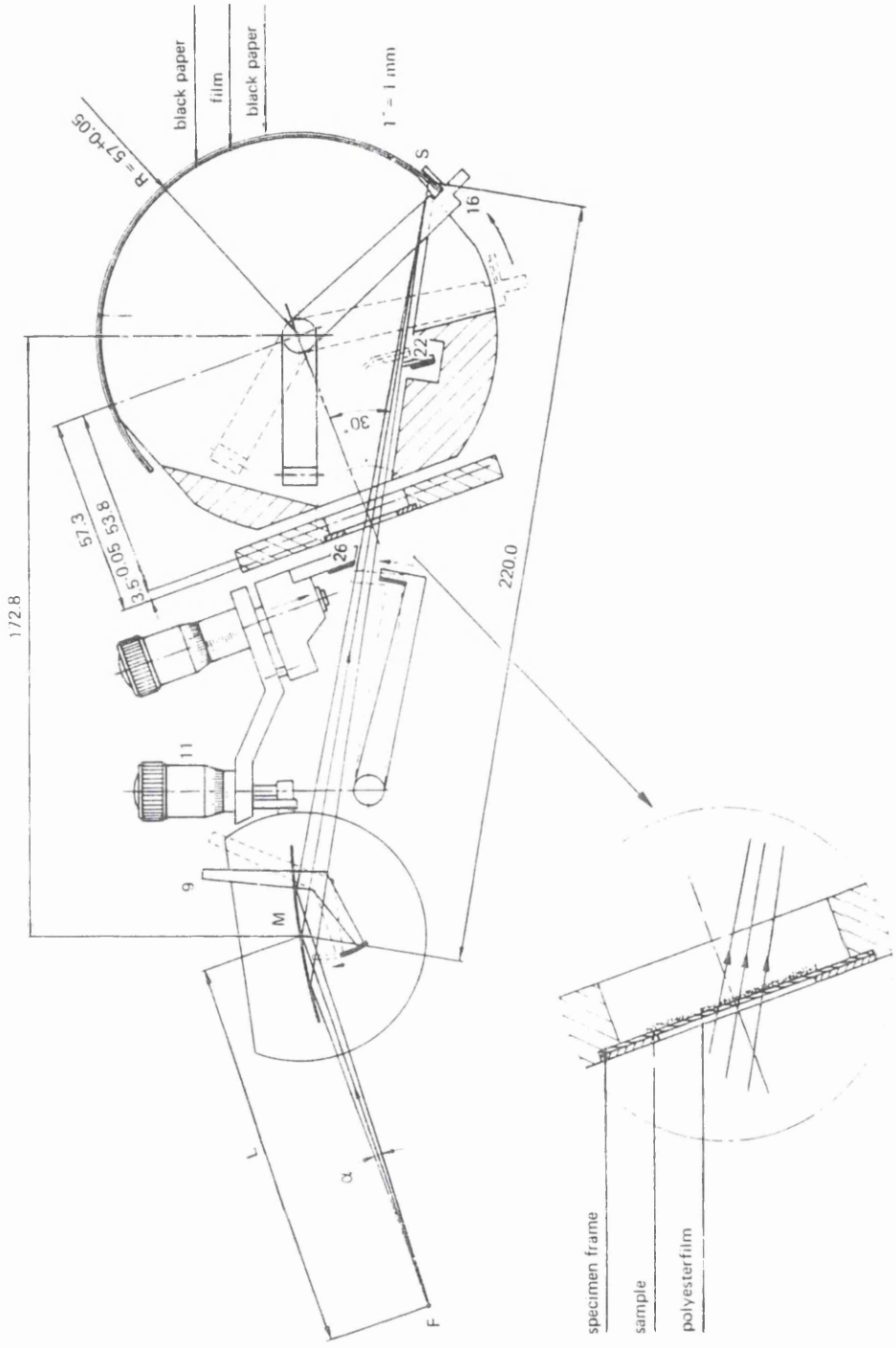

Figure 2.1 Principle layout of the Guinier-de Wolff camera [1].

2.2 Thermal Analysis

Thermal analysis techniques and in particular differential scanning calorimetry (DSC) proved to be an essential tool for the characterisation of Li-Mn-O oxides [2]. Thermal analysis was carried out on Stanton Redcroft TG-DSC simultaneous thermal analyser Model STA625. The instrument is designed to record thermogravimetric (TG) data and differential scanning calorimetry (DSC) data simultaneously. Figure 2.2 shows a schematic diagram for the STA625 thermal analyser.

The simultaneous unit eliminates the problem of correlating TG and DSC data for the same sample. Separate instruments for TG and DSC do not necessarily operate under the same conditions so the information obtained from simultaneous TG-DSC may be more reliably correlated.

The STA625 thermal analyser is computer controlled via a Stanton Redcroft Data Acquisition System. This facilitates the automatic conversion of the differential signal into DSC output so that the enthalpies of the various processes taking place in the sample may be measured directly from the peak areas of the curve regardless of the temperature range of interest.

The balance system is based on a 5 g electronic micro-balance which is easy to operate. The balance control module provides an analogue signal to give very high resolution [3].

The furnace has an operating range of 0-1500 °C and may be programmed to heat linearly with time to a chosen temperature and then to thermostat at this temperature or

be switched off. It can be programmed to heat and cool linearly or to cycle between chosen temperature limits. Any heating rate between 0.2-60 °C/min may be chosen. Principally, a rate of 5 °C/min or 10 °C/min was used to gain a better curve definition and to avoid collecting a large amount of data on the computer storage media. The furnace could be adapted to accept a static or flowing gas atmosphere, up or down as required. It is fitted with a flow meter graduated 0-100 % (the 100% mark corresponds to approximately 80-100 ml/min depending upon the particular gas). When an inert gas was required B.O.C. "white spot" nitrogen (>99.99 % purity) was usually used. In some experiments, an atmosphere of air was required and achieved by the use of B.O.C. compressed air.

The hang-down arrangement houses the Chromel/Alumel flat plate thermocouple system for differential and sample temperatures.

The DTG trace was obtained by differentiating the weight loss curve using the control software. This would clearly indicate the number of processes in overlapping weight losses. To calculate the percentage of each overlapping weight change, the software provided could be used. An example of such a calculation is shown below.

The area under curve A is found to be 89.09% and under curve B is 19.91% and the whole weight loss calculated from the TG trace for both overlapping weight changes is 6.05%. These values are substituted in the following relationships

$$w_1 + w_2 = w_T \qquad \frac{A_1}{A_2} = \frac{w_1}{w_2} \qquad \frac{A_1}{A_2} = \frac{89.09}{19.91} = 4.02$$

where A_1 and A_2 are the areas under the curves for A and B respectively, w_1 and w_2 are the weight losses during the first and the second overlapping changes.

$$\frac{w_T - w_2}{w_2} = \frac{A_1}{A_2} \qquad w_2 = \frac{w_T}{\frac{A_1}{A_2} + 1} = \frac{6.06}{4.02 + 1} = \frac{6.06}{5.02} = 1.205\%$$

$$w_1 = w_T - w_2 \qquad \text{so} \qquad w_1 = 6.05 - 1.205 \qquad w_1 = 4.85\%$$

So the correct percentage weight change is found for each overlapping step of the reaction.

The collected data were stored on IBM computer storage media and may be treated mathematically using the PL-STA software and then plotted graphically on a HP pen plotter.

The STA625 thermal analyser was used intensively as a reaction environment to perform most of the solid state reactions. One example of such a reaction is the reaction of Li_2CO_3 and Mn_2O_3 at different Li:Mn ratios. The progress of the reaction was monitored by recording the accurate weight and heat changes during the course of the reaction with increasing temperature under different ambient atmospheres.

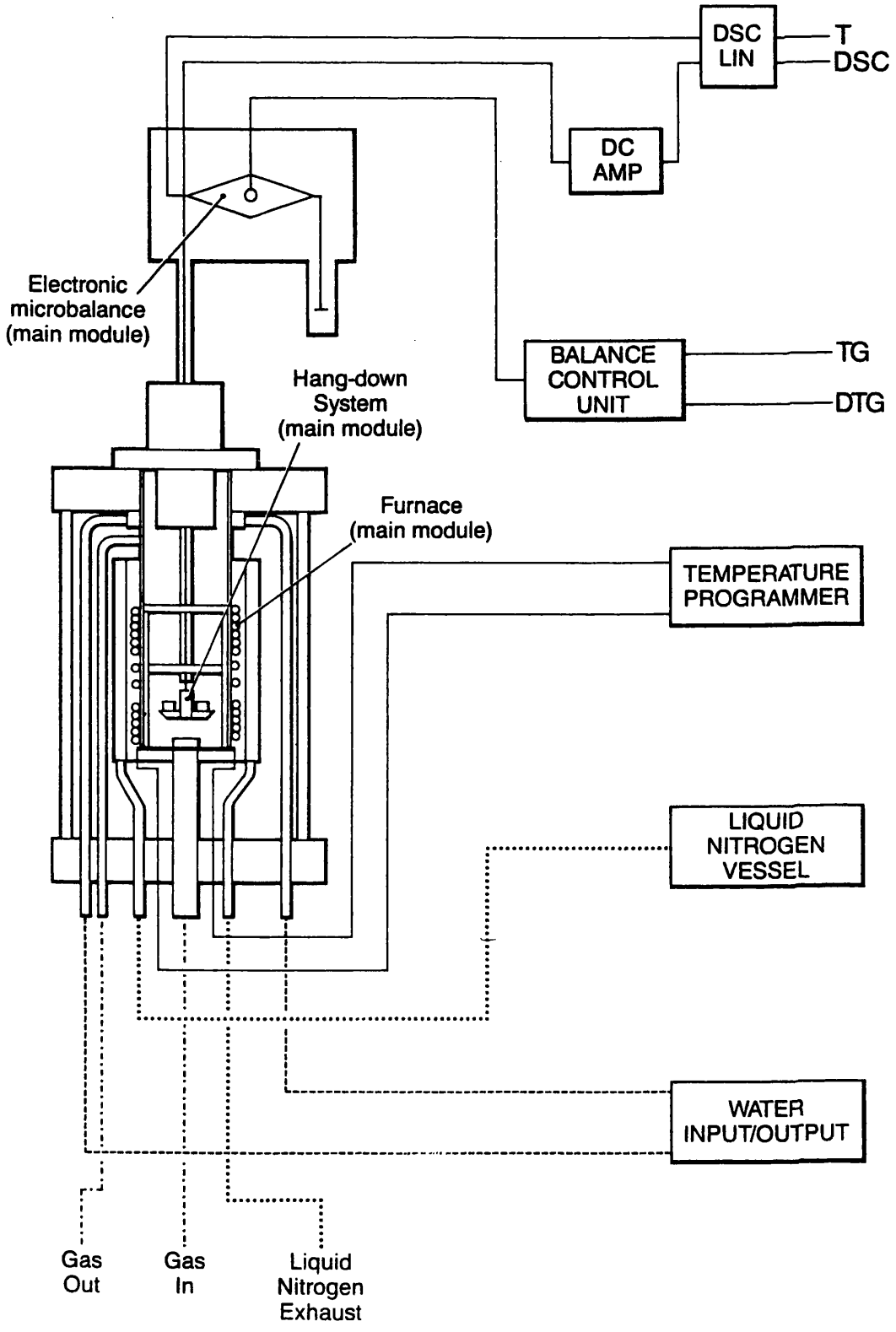

Figure 2.2 Schematic diagram of the STA625 thermal analyser [3].

2.3 Electron Microscopy

JEOL JEM 35C and JEOL JEM 6100 electron microscopes were available as a service from the Department of Materials Engineering of the University of Wales Swansea. Transmission and scanning electron microscopy (S.E.M.) were used during the course of this study. Both machines have a magnification power up to 100,000.

The samples were prepared by dispersing a small amount of the solid sample on to a carbon film. The excess of the sample was then discarded using compressed air, leaving a thin layer of the sample.

2.4 Spectrophotometry

The Fourier Transform Infra Red (FTIR) experiments were done using a Perkin Elmer 1725X FTIR Spectrometer. The samples were prepared by grinding a small amount of the specimen in proportions of about 1:100 by weight with KBr; the resultant mixture was pressed under a pressure of 10 tons per square inch to form a thin translucent disk.

Ultraviolet and visible measurements were taken using the Philips PU8720 UV/VIS scanning spectrophotometer.

2.5 Atomic Absorption Spectroscopy and Flame Photometry

The manganese content of the samples was determined using a BAIRD ALPHA2 Atomic Absorption Spectrophotometer. Lithium content was also determined using the BAIRD ALPHA2 Atomic Absorption Spectrophotometer in the emission mode and a simple EEL flame photometer fitted with a Li filter.

The results were obtained by plotting a calibration curve using known amounts of the standard in a suitable range of concentrations. A solution of the unknown sample was then run under the same conditions and the concentration of the element under investigation found using the calibration curve.

2.6 Surface Area Measurements

When required, the surface area of samples was determined using a single point BET method [4]. A mixture of known composition of two gases (nitrogen and helium) was passed over the sample cooled in liquid nitrogen. The nitrogen gas which adsorbed on the sample surface caused a change in the composition of the gas mixture stream. This would change its thermal conductivity giving an adsorption peak on a chart recorder connected to the sorptometer. When the liquid nitrogen was removed from the sample, desorption occurs, giving a second peak which is used for the determination of the powder's surface area, since this peak is cleaner and has less tailing associated with it than the adsorption peak. Figure 2.3 shows a schematic diagram of the single point nitrogen BET surface measurement equipment used in this work.

The sample must be degassed for at least 24 hours in flowing nitrogen. The measurements can be taken after immersing the sample and the gas trap in liquid nitrogen; standard and sample peaks had to be taken at least four times in alternate order, in order to minimise the experimental error. The areas of the peaks were measured by cutting out the areas under the peaks on the recorder paper and weighing them. Also the weight of the sample, the room temperature, the atmospheric pressure and the attenuation values used were recorded for the calculations.

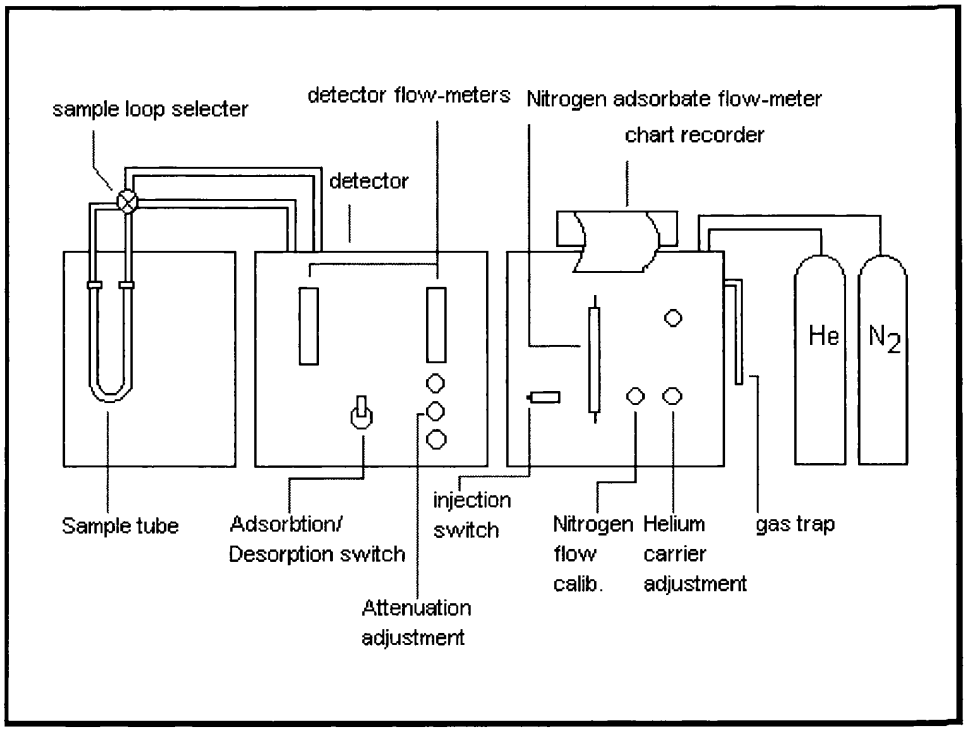

Figure 2.3 The single point nitrogen BET surface area measurement equipment.

The calibration factor needed to be calculated first by taking the reciprocal value of the average weight of the standard peaks multiplied by the standard attenuation value. Then the volume of gas adsorbed by the sample (V_d) was calculated by multiplying the average of the sample peaks by the sample attenuation value and then by the calibration factor. This value was then converted to the standard conditions by multiplying V_d by 0.359 (standard temperature divided by standard pressure) and the atmospheric pressure, and dividing by room temperature. This gave V_{dStd}, which must be multiplied by the known cross-sectional area of 1 ml of nitrogen at STP, which is 4.385 m^2. This gave the surface area of the sample which had to be divided by the weight of the sample (in grams) in order to obtain the specific surface area in $m^2\ g^{-1}$.

$$\text{i.e. Calibration factor} = \frac{1}{\text{Average standard weight} \times \text{Standard attenuation}}$$

Then

V_d = Average weight of sample peak × Sample attenuation × Calibration factor

$$\text{so} \qquad V_{dStd} = 0.359 \times V_d \times \frac{\text{Atmospheric Pressure (mmHg)}}{\text{Room Temperature (K)}}$$

Thus,

Surface area = $4.385 \times V_{dStd}$ and then,

$$\text{Specific surface area } (m^2\ g^{-1}) = \frac{\text{Surface area}}{\text{Weight of sample (g)}}$$

2.7 High Temperature Furnace

The solid state reactions were carried out using a Carbolite tube furnace. The furnace is capable of providing a temperature up to 1600 °C with an accuracy of ±10 °C. The furnace is controlled to heat up to the desired temperature and either thermostatted at this temperature or switched off.

The furnace is able to provide a controlled atmosphere for temperatures up to 500 °C. The specimens were contained in porcelain crucibles and inserted into the centre of the tube and heated up and left to cool down slowly inside the furnace.

2.8 Computing

When the standard BET method was used, a FORTRAN program was written to minimise the enormous time spent using graph paper to plot the data and carrying out manual curve subtraction. The program was based on the least squares curve fitting method. See Appendix 1. For the analysis of data collected using the single point BET method described above, a FORTRAN program employing the least square analysis technique was used. The program is listed in Appendix 2.

For x-ray analysis, the d-values collected from the x-ray diffraction film were corrected using a Math CAD program written especially for that reason. See Appendix 3. The program gives good agreement with the results found using the manual method and correction using the Lagrange formula [5, 6].

The Q.C.P.E. program number 331 (Muller and Goldberg) [7] used supplied cell constants (taken from I.U.D.D. files) to calculate d values. The calculation was limited by the data, which specified such parameters as maximum camera angle, cell type (or chosen range of Miller indices) and the radiation used. Results were presented in order of decreasing d values, with their associated Miller indices and 2θ values. See Appendix 4.

To calculate the cell constants from d values, version 15 of the program FZON (originally written by J. Visser [8]) finds the zones, and uses these to find reciprocal lattices, which are then reduced in a simple way. Each solution was compared with experimental data and a figure of merit was calculated. The program requires a minimum of twenty observed lines as data, so it was not useful for all the samples.

2.9 Chemicals and Standards

Chemicals, compounds used	Sources	Purity
Chemicals		
Lithium carbonate Li_2CO_3	Aldrich	Laboratory reagent 99+%
Manganese (III) oxide Mn_2O_3	Alpha	98%
Iron (III) chloride hydrate $FeCl_3.6H_2O$	B.D.H.	Analar
Aluminium (III) chloride hydrate $AlCl_3.6H_2O$	B.D.H.	G.P.R. 97%
Lithium nitrate $LiNO_3$	Fluka	99.5%
Standards		
Potassium aluminium sulphate $KAl(SO_4)_2.12H_2O$	B.D.H.	Analar 99.5%
Aluminium wire	Fisons	Analytical Reagent 99.995%
Iron wire	Aldrich	99.9%
Potassium chloride KCl	B.D.H.	Analar
Potassium bromide KBr	B.D.H.	Analar
Manganese(II) sulphate hydrate $MnSO_4.4H_2O$	B.D.H.	G.P.R. 97%
Reagents		
Sodium sulphite hydrate $Na_2SO_3.7H_2O$	B.D.H.	Analar 97%
Hydrogen peroxide H_2O_2	Fisons	Analytical reagent
Sodium oxalate $Na_2C_2O_4$	Sigma	ACS Reagent 99.5%
Potassium permanganate $KMnO_4$	Sigma	ACS Reagent 99.0%
8-Hydroxyquinoline HOC_9H_6N (oxine)	Sigma	ACS Reagent
Ammonium chloride NH_4Cl	Sigma	ACS Reagent
E.D.T.A.	B.D.H.	G.P.R.
Cupferon	Sigma	ACS Reagent
Miscellaneous		
Hydrochloric acid HCl	B.D.H.	G.P.R.

Sulphuric acid H_2SO_4	B.D.H.	G.P.R.
Nitric acid HNO_3	B.D.H.	G.P.R.
Ammonia solution NH_3	B.D.H.	G.P.R.
Tartaric acid	B.D.H.	G.P.R. 99%
Sodium hydroxide NaOH	B.D.H.	G.P.R. 96%
Potassium cyanide KCN	B.D.H.	G.P.R. 96%
Chloroform	B.D.H.	G.P.R.
Double distilled de-ionised water		
Nitrogen	B.O.C.	White spot oxygen free
Compressed Air	B.O.C.	
Carbon dioxide CO_2	B.O.C.	

2.10 Analytical Techniques

2.10.1 Determination of Manganese

The percentage of manganese was determined as MnO_2 by the sodium oxalate method [9]. A 100 ml portion of 10% (by volume) sulphuric acid and 1.000 gram of sodium oxalate were added to a 300 ml Erlenmeyer flask, followed by 0.5 gram of the sample under analysis. The reaction was allowed to proceed on a steam bath until the sample had decomposed. The excess oxalate was determined by the titration of the hot solution with 0.02 M potassium permanganate. The potassium permanganate was prepared and calibrated as described by Vogel [10]. The percentage of manganese dioxide was calculated from the equation

$$\%\,MnO_2 = \frac{4.346\left(\frac{1}{0.067} - 5 \times T \times M\right)}{W}$$

where W is the weight of sample, T is the sample titre, M is the molarity of potassium permanganate.

Since the oxalate method is subject to a positive error resulting from air oxidation of oxalate, passing CO_2 gas into the flask until the time of the titration provided an inert atmosphere.

The experiment was repeated at least three times in order to determine the standard deviation of error. The precision of the experiment is between 0.5 and 1.15%.

The ferrous sulphate method [9] and the potentiometric titration method [11,12] were tried and did not show any agreement when standard materials were analysed.

Atomic absorption spectroscopy has also been used to determine the amount of manganese in the samples. Manganese (II) sulphate hydrate ($MnSO_4.4H_2O$) was used as a standard material to prepare the solutions required for the calibration curve. A suitable amount of the manganese sample under investigation was dissolved and diluted to a concentration within the concentration range of the calibration curve. The manganese content may be found using the calibration curve, graphically or using a programmable calculator.

The individual measurements were repeated at least five times and a typical calibration curve used has a correlation coefficient of 0.993707 and standard error of the estimate of $3.345E^{-2}$.

2.10.2 Determination of Lithium

The amount of lithium in the lithiated manganese oxide samples was determined by atomic emission spectroscopy, using the atomic absorption spectroscopy (AAS) instrument (section 2.5) in the emission mode. Lithium carbonate was used as a standard material for preparing the solutions required for the calibration curve. The lithiated

samples under investigation were then dissolved in 4 ml of 1:1 hydrochloric acid and 1 ml of concentrated sulphuric acid and made up to 20 ml in a volumetric flask. An equal amount of ionisation suppresser (potassium chloride at 2000 $\mu g\ l^{-1}$) was added to the standard and the sample solutions.

The individual measurements were repeated at least five times and a typical calibration curve has a correlation coefficient of 0.999161 and standard error of the estimate of $1.2160E^{-2}$.

The amount of lithium has also been determined using a flame photometer fitted with a lithium filter. The range of concentrations used was between 2-20 ppm, and the technique does not require any ionisation suppresser.

Unsuccessful trials were made to determine the lithium content in the lithiated manganese oxide samples as lithium aluminate, as described by Vogel [13]. The result was a large amount of black precipitate, which might be caused by the large amount of manganese in the samples.

References

1 Guinier-De Wolff camera, model II operation instructions.

2 J.M. Amarilla and RM. Rojas, *J. Thermal Analysis and Calorimetry*, **73**, 191 (2003).

3 Stanton Redcroft TG-DSC Thermal Analyser STA625 operation instructions.

4 S. Brunaur, P.H. Emett, and E. Teller, *J. Am. Chem. Soc.,* **60**, 309 (1938).

5 A. Ralston, *A First Course in Numerical Analysis*, McGraw-Hill Book Co. (1965).

6 W.H. Press, B.P. Flannery, S.A. Teukolsky, and W.T. Vetterling, *Numerical Recipies, The Art of Scientific Computing*, Cambridge University Press, Cambridge (1986) p.77.

7 J. Muller and S. Goldberg, *J. Chem. Ed.,* **54**, 54 (1977).

8 J. Visser, *J. Appl. Cryst.,* **2**, 89 (1969).

9 M.J. Katz, R.C. Clarke, and W.F. Nye, *Anal. Chem.,* **28**, 507 (1956).

10 A.I. Vogel, *Quantitative Inorganic Analysis*, 5th ed., Longman, Harlow (1981) p.351.

11 K.J. Vetter and N. Jaeger, *Electrochim. Acta,* **11**, 401 (1966).

12 J.J. Lingare and R. Karplus, *Indust. & Eng. Chem.,* **18**, 191 (1946).

13 A.I. Vogel, *Quantitative Inorganic Analysis*, 5th ed., Longman, Harlow (1981) p. 43.

Preparation, Characterisation, and Study of Spinel Related Manganese Oxides – $LiMn_2O_4$

This chapter describes how the spinel $LiMn_2O_4$ was prepared and subsequently characterised using x-ray diffraction, electron microscopy, thermal analysis, FTIR spectroscopy, surface area measurements and chemical analysis.

3.1 Introduction

Manganese dioxides have been used widely as cathode materials in the Leclanché type dry cell, which is still probably the most popular and inexpensive source of current for a number of portable electronic products. Catalysts based on manganese oxides are also widely used for the oxidation of CO and other organic compounds [1]. For rechargeable non-aqueous batteries, the most widely used cathode material is $LiCoO_2$, which possesses a high specific capacity of 0.12-0.13 ampere hour per gram (A h g^{-1}) and a good cycling life [2].

The high cost of cobalt and its environmental hazards added to its vulnerability to permanent structure disorder in case of over-charge, led to the start of a search for an alternative to this oxide. $LiNiO_2$ and $LiMn_2O_4$ represent the possible alternative oxides to that of cobalt [3]. The more attractive of the above oxides is $LiMn_2O_4$, since it can be prepared from cheap starting materials, is non-toxic and can stand an over-charge, as full de-lithiation results in the stable form of the spinel λ-MnO_2. The theoretical specific capacity (~0.12 A h g^{-1}) and D_{Li+} value of 10^{-9} cm^2 s^{-1} for $LiMn_2O_4$ do not differ greatly from those of $LiNiO_2$ and $LiCoO_2$, although $LiMn_2O_4$ shows better rate capabilities [4]. The above properties can be achieved by preparing the oxide with good porous particles

(surface area >5 m^2 g^{-1}), while the other two oxides have particles with low surface area of ~1 m^2 g^{-1} [5, 6, 7, 8, 9].

The spinel $LiMn_2O_4$ is usually prepared by mixing stoichiometric amounts of lithium salts such as Li_2CO_3, LiOH, $LiNO_3$ or LiI with manganese oxides, acetates, or hydroxide powders. The mixtures are then heated in air up to 900 °C [8, 9, 10, 11, 12, 13]. The preparation conditions, e.g. heat treatment temperatures and Li/Mn ratio of the starting materials, of the spinel $LiMn_2O_4$ play a major role in deciding the properties of the product manganese dioxide λ-MnO_2. Feng *et al.* [14] found that the extraction/insertion reactions of lithium ions with the spinel-type lithium manganese oxide depend on the preparation conditions of the parent oxide $LiMn_2O_4$. Therefore Manev *et al.* [8, 12, 13] tried to point out the problems associated with the preparation of $LiMn_2O_4$ and λ-MnO_2. They also tried to establish the best preparation conditions for these oxides to obtain the best performance with regard to their use in rechargeable lithium batteries. They found that using a chemically obtained manganese dioxide (CMD), instead of an electrochemically obtained one (EMD), and lithium nitrate or lithium hydroxide instead of lithium carbonate has an advantage when the product is used at high discharge rates. The thermal pre-treatment of the reaction mixture in the temperature range 350-550 °C improves the electrochemical behaviour of the samples. The optimum results were obtained with reaction times of the main synthesis from 75 to 200 hours at temperatures in the 650-750 °C range [12].

Using the wet-chemical technique at low temperature, Tsumura *et al.* [15] obtained a sample of $LiMn_2O_4$ with high surface area (9.7 m^2 g^{-1}), using lithium acetate dihydrate

and manganese acetate tetrahydrate in ethanol. The solvent then evaporated and the resultant powder was heated above 250°C. The lithium chemical diffusion coefficient in $LiMn_2O_4$ as synthesised by the wet-chemical method is at least ten times higher than that of $LiMn_2O_4$ obtained by solid state reaction [16]. In the search for a cathode material with superior electrochemical properties, other researchers had used the original wet-chemical methods [17, 18, 19, 20] and others had modified them. The modifications reported are: the use of citric acid as a chelating agent [21, 22, 23, 24], the use of tartaric acid as a chelating agent [25, 26, 27, 28], the use of oxalic acid as a chelating agent [29], and finally the use of succinic acid as a chelating agent [30].

$LiMn_2O_4$ has also been prepared using the Pechini process [31]. The process is carried out by adding a 1:4 mixture of citric acid and ethylene glycol at 90°C to mixed powders of lithium and manganese nitrates. The resultant mixture is then treated in a series of reactions and finally fired in air at temperatures above 250°C to give a fine powder of $LiMn_2O_4$. The process offers a low temperature synthetic method, yields inorganic oxides with excellent phase purity and well-controlled stoichiometry [32].

Reflecting the importance and the interest shown in the spinel $LiMn_2O_4$ and its use as a cathode material, various other methods of preparation have been reported. To name a few: the Dynamic Process [33], the combustion method [34, 35, 36], the pulsed laser deposition method [37], the mechanical alloying method [38], the microwave synthesis method [39], the electrostatic spray deposition (ESD) method [40], and the ultrasonic spray pyrolysis method [41].

Each of the above methods possesses some advantages over the others, but the main objective of all the above methods is to obtain a single-phase spinel $LiMn_2O_4$ with high surface area and low levels of impurities which can be used as a cathode material in lithium rechargeable cells. Despite the concern that spinel samples with high surface area might favour electrolyte decomposition or spinel dissolution, which lead to cell self-discharge, Pistoia *et al.* found that self-discharge is inversely proportional to surface area [4].

The structure of $LiMn_2O_4$ has been determined by Rietveld analysis of powder neutron diffraction data. $LiMn_2O_4$ is found to have a cubic unit cell with space group Fd3m a = 8.2468 Å [42]. Single crystal x-ray diffraction examination of the spinel $LiMn_2O_4$ also confirmed the cubic unit cell with lattice constant of a = 8.2483 Å [43]. The structure of a typical AB_2O_4 normal spinel is shown in Figure 3.1

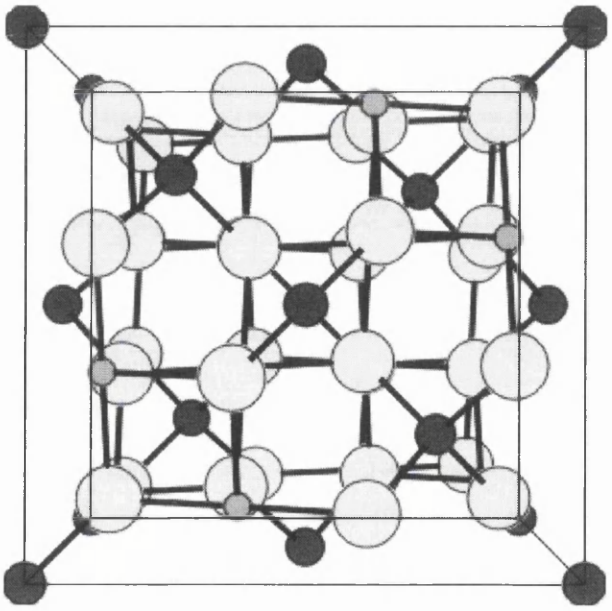

Figure 3.1 The normal AB_2O_4 spinel structure.

From the sections above, we can see that the insertion/extraction reaction of lithium has been extensively investigated since the early 1980's [44]. Despite the limited practical capacity of about 0.12 A h g^{-1}, $LiMn_2O_4$ is considered to be a very attractive cathode material, mainly due to its easy of manufacturing, low cost and environmental compatibility [45]. Certainly, some battery manufacturing companies have announced the use of lithium manganese oxides as cathodes in the production of Li-ion batteries [46]. However, $LiMn_2O_4$ suffers from significant capacity fading upon cycling due to irreversible structure changes and storage losses, especially at high temperature. Large research efforts have been devoted to solving this problem by various techniques such as modifying the preparation conditions and doping the oxide with other metals like Ni or Co [47, 48].

In the present work, a preparation method based on the classical firing technique has been developed to obtain a pure, single-phase and high surface area spinel $LiMn_2O_4$. The spinel lithium manganese oxide, $LiMn_2O_4$, has been characterised using x-ray diffraction, scanning electron microscopy (SEM), FTIR spectroscopy, thermal analysis techniques (TG and DSC), chemical analysis and single point surface area measurements. Surface area measurements of the produced lithium manganese oxide $LiMn_2O_4$ gave 7.6 m^2 g^{-1}. $LiMn_2O_4$ prepared using the procedure described in this work has a relatively high surface area when compared with those reported in the literature and prepared using the firing technique [49, 50].

3.2 Experimental and Results

3.2.1 Preparation of $LiMn_2O_4$

3.2.1.1 Chemicals

The manganese source throughout all the preparations was manganese (III) oxide Mn_2O_3. Manganese (III) oxide was purchased from Alpha chemicals with a purity of 98%. On the other hand, lithium sources used in this work are lithium nitrate $LiNO_3$ and lithium carbonate Li_2CO_3. Lithium nitrate was purchased with a purity of 99.5% from Fluka chemicals. Lithium carbonate was purchased from Aldrich chemicals as a laboratory reagent with a purity of 99+ %.

3.2.1.2 Initial Thermal Study of the Starting Materials

$LiMn_2O_4$ has been previously prepared by the classic firing technique, which was first described by Wickham and Croft [10]. This technique is simply the reaction of stoichiometric amounts of lithium and manganese precursors at high temperatures. In order to choose the right reaction conditions, the thermal behaviours of the starting materials were closely examined. The thermal behaviour of the reactants ($LiNO_3$, Li_2CO_3 and Mn_2O_3) was studied using the Stanton Redcroft TG-DSC simultaneous thermal analyser STA625, which has been described in Chapter 2.

a) Thermal Study of Lithium Nitrate $LiNO_3$

Thermogravimetric Analysis (TGA) and Differential Scanning Calorimetry (DSC) results of lithium nitrate $LiNO_3$ showed some weight loss (about 6%) at about 67 °C,

which could be related to some adsorbed moisture on the surface of the sample (see Figure 3.2). The nitrate started to disintegrate at about 550 °C with a weight change of about 79%, which is in good agreement with the theoretical value of 78.33%. The weight change is represented by Equation 3.1.

$$2LiNO_3 \xrightarrow{660\,^{\circ}C} Li_2O + 2NO_2 \uparrow + \tfrac{1}{2}O_2 \uparrow \qquad 3.1$$

On the other hand, the Differential Scanning Calorimetry (DSC) curve of $LiNO_3$ shows an endothermic reaction occurring at around 260 °C, the melting point of $LiNO_3$ (literature value of 264 °C).

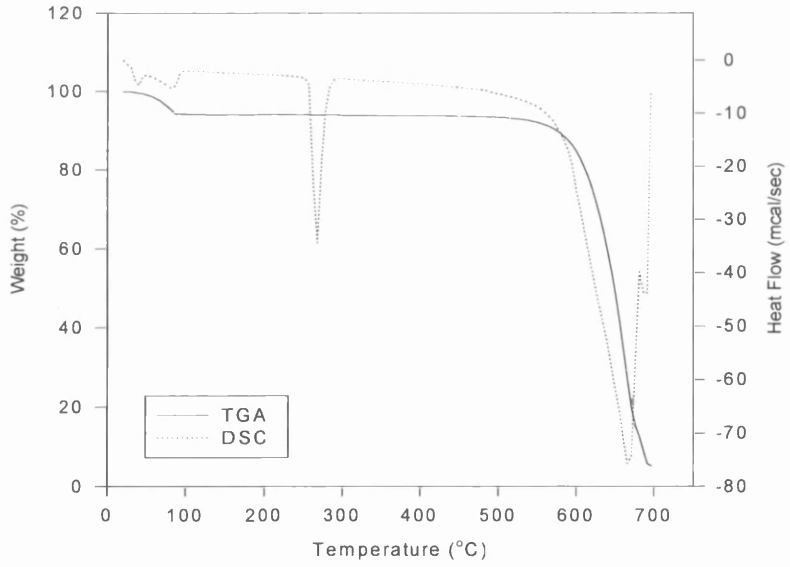

Figure 3.2 Thermal analysis results for $LiNO_3$.

b) Thermal Study of Lithium Carbonate Li_2CO_3

Analogous analysis of lithium carbonate Li_2CO_3 gave TG and DSC traces that are illustrated in Figure 3.3. The traces show that Li_2CO_3 starts to disintegrate and release CO_2 at about 750 °C preceded by its melting at about 700 °C (literature value 723 °C). The weight loss of 61.4% agrees with the theoretical value of 59.6%, which corresponds to the evolution of CO_2 according to Equation 3.2.

$$Li_2CO_3 \xrightarrow{100\ ^oC} Li_2O + CO_2 \uparrow \qquad 3.2$$

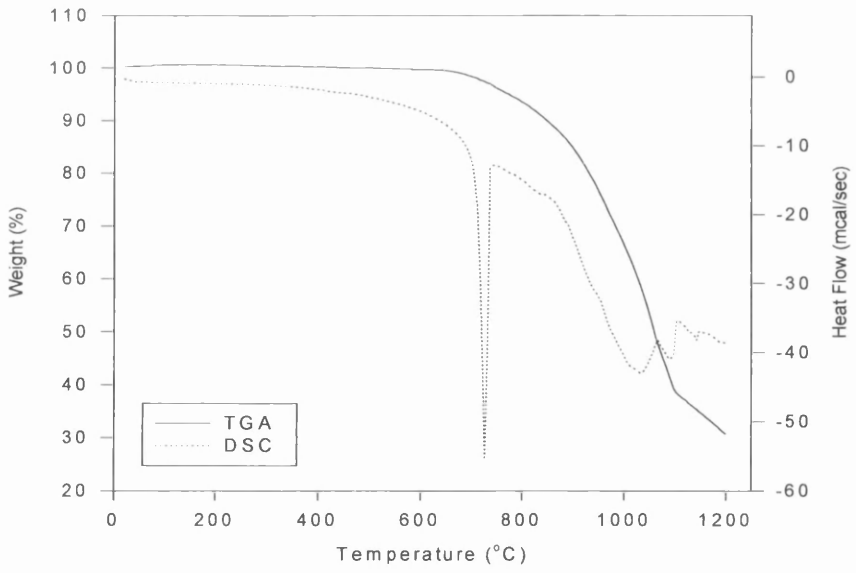

Figure 3.3 Thermal analysis results for Li_2CO_3.

c) Thermal Study of Manganese Oxide Mn_2O_3

The thermal stability of manganese (III) oxide Mn_2O_3 (98%) was investigated using Thermogravimetric Analysis (TGA) and Differential Scanning Calorimetry (DSC) (Figure 3.4). TGA and DSC of Mn_2O_3 showed that the oxide is stable on heating up to about 950 °C when a sharp drop in its weight of about 4.05% occurs. This change in weight is easily attributed to the conventional loss of oxygen upon heating and the transformation of Mn_2O_3 to Mn_3O_4. A small change of weight of 0.52% was found at lower temperatures and could be assigned to adsorbed and bound water.

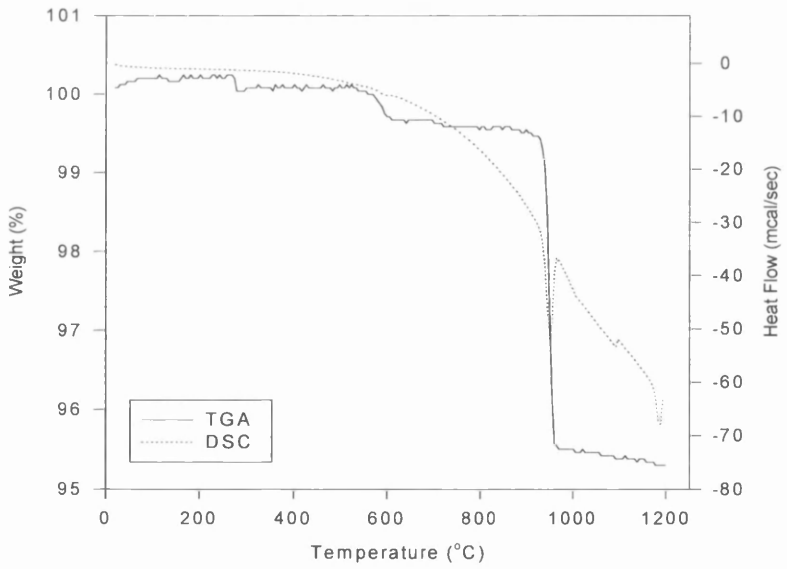

Figure 3.4 Thermal analysis results for manganese (III) oxide Mn_2O_3.

From the above results, the pre-heating treatment of the reactants should be executed at a temperature somewhat between the melting point of the selected lithium salt and the disintegration temperature. This should allow the molten salt to penetrate the pores on the surface of the metal oxide and, thereby, form a homogeneous mixture that can then be heated to the desired temperature. The advantage of using the above technique is the great improvement of the contact area between the lithium salt and the manganese oxide. The preheating treatment temperatures for $LiNO_3$ and Li_2CO_3 are to be 500 °C and 700 °C respectively.

d) Thermal Study of Stoichiometric Mixtures of the Starting Materials

1) In Air

Thermal analysis of 1:2 stoichiometric mixtures of the starting materials, $LiNO_3$+Mn_2O_3 and Li_2CO_3+Mn_2O_3, between 20-1200 °C in air revealed the main thermal effects (Figure 3.5).

The TGA results illustrated in Figure 3.5 show that the reaction between Li_2CO_3 and Mn_2O_3 progress according to the model proposed by Howard [51]. According to Howard, the preparation of $LiMn_2O_4$ proceeds in two steps. The first step is the formation of the intermediate $LiMnO_2$ according to the reaction between Li_2O and Mn_2O_3.

$$Li_2O + Mn_2O_3 \xrightarrow{t>530\,^{\circ}C} 2LiMnO_2 \qquad 3.3$$

The second main step is associated with two iterative reactions as follows.

$$3LiMnO_2 + \tfrac{1}{2}O_2 \xrightarrow{t>530\,^{\circ}C} LiMn_2O_4 + Li_2MnO_3 \qquad 3.4$$

$$2Li_2MnO_3 + 3Mn_2O_3 + \tfrac{1}{2}O_2 \xrightarrow{t>600\,^{\circ}C} 4LiMn_2O_4 \qquad 3.5$$

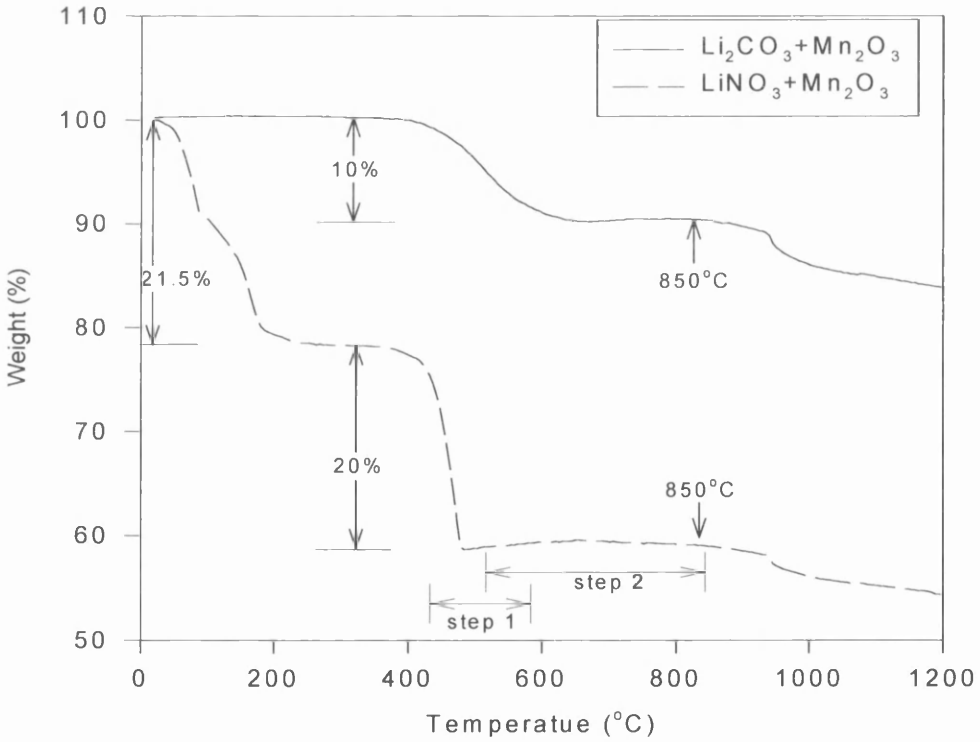

Figure 3.5 Thermogravimetric Analysis (TGA) results of the reaction progress between lithium salts ($LiNO_3$ and Li_2CO_3) and manganese (III) oxide Mn_2O_3 in air.

The starting point of each of the above reactions is not defined but it varies depending on the starting materials. Figure 3.5 clearly shows the sharp decrease in weight (step 1) according to reaction 3.3 and the slight increase in weight (step 2) due to the oxygen uptake according to reactions 3.4 and 3.5.

Experimental values of the mass loss agree well with the theoretical ones. For the reaction between Li_2CO_3 and Mn_2O_3, a weight loss of 10% was recorded, less than the theoretical value of 11.4%, which could be assigned to the evolution of CO_2 and the formation of Li_2O according to reaction 3.2. The reason for the low weight loss is that the evolution of CO_2 (reaction 3.2) coincides with oxygen uptake by the sample (reactions 3.4 and 3.5), leading to a low overall weight loss, as recorded by the TGA trace.

For the reaction between $LiNO_3$ and Mn_2O_3, a mass loss of about 21.5% is observed between 20-200 °C. The nature of this weight loss is not fully understood. The changes takes place at relatively low temperatures for any structural change to occur, therefore it is thought to be the result of a mixture of adsorbed water and the remnants of some of the organic solvent used to premix the reactants.

The second major weight loss of about 20% is taking place between 350-450 °C. The value is in good agreement with the theoretical value of 20.3% according to reaction 3.6.

$$LiNO_3 + Mn_2O_3 \rightarrow LiMn_2O_4 + NO_2 \qquad 3.6$$

The good agreement between the experimental and the theoretical values indicates that there is no oxygen uptake from the air and this would suggest that $LiMn_2O_4$ could be prepared by heating stoichiometric amounts of $LiNO_3$ and Mn_2O_3 in the absence of oxygen. This theory proved to be true when the above mixture was heated between 20-1200°C in nitrogen, as will be described in the next section.

Both mixtures were heated in air up to 850 °C, annealed at this temperature for one hour and allowed to cool to room temperature. Samples of the products from both reactions were examined by x-ray powder diffraction. The x-ray diffraction results showed the evolution of a single-phase spinel and could be assigned to the spinel $LiMn_2O_4$, when compared with the results reported in J.C.P.D.S. file 35-782. On increasing the temperature to about 900 °C, the spinel started to decompose. The loss of oxygen from $LiMn_2O_4$ after 900 °C is accompanied by the reduction of the tetravalent manganese to the trivalent state and a decrease in the attractive force between the Mn and O ions. An electrochemically undesirable expansion of the unit cell volume occurs [52]. Therefore, to avoid the undesirable loss of oxygen from the final product, the firing temperature should be in the range 800 to 900 °C.

2) In Nitrogen

Thermal analysis of 1:2 stoichiometric mixtures of the starting materials, $LiNO_3$+Mn_2O_3 and Li_2CO_3+Mn_2O_3, between 20-1200 °C in nitrogen gave an identical TGA trace for the mixture containing lithium nitrate to that run in air, and produced an extra weight loss in the case of the mixture containing lithium carbonate. The main features of the effect of nitrogen on the TGA traces of both reactions are shown in Figure 3.6.

For the reaction between $LiNO_3$ and Mn_2O_3, the first mass loss between 20-200 °C is similar to that found in air and the same argument would apply. The second main mass loss of about 22% which takes place at about 480 °C, is associated with reaction 3.6 that have the theoretical value of 20.3% and the oxide $LiMn_2O_4$ is formed.

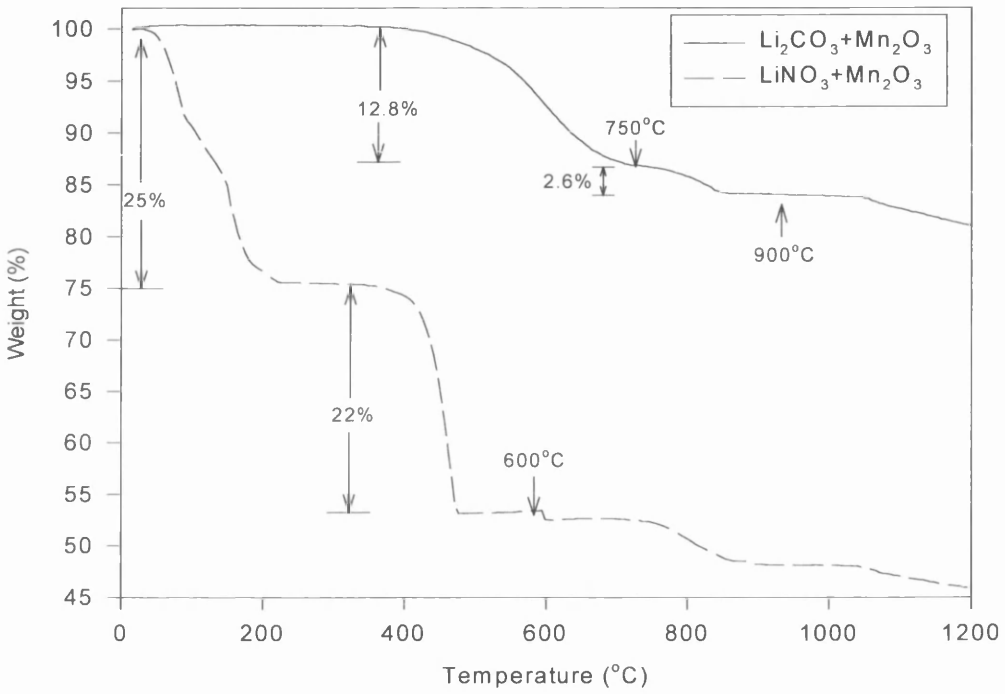

Figure 3.6 Thermogravimetric Analysis (TGA) results of the reaction progress between lithium salts ($LiNO_3$ and Li_2CO_3) and manganese (III) oxide Mn_2O_3 in nitrogen.

To test the credibility of the above statement, the mixture was heated up to 600 °C and annealed at this temperature for one hour, and then allowed to cool to room temperature, all under nitrogen. A sample of the product was examined by x-ray powder diffraction.

The x-ray diffraction results were identical to those found for the same mixture in air. The diffraction pattern is for a single-phase cubic spinel and could be assigned to the spinel $LiMn_2O_4$, when compared to that reported in J.C.P.D.S. file 35-782. The above results show that the spinel $LiMn_2O_4$ can be obtained by reacting stoichiometric amounts (1:2) of $LiNO_3$ and Mn_2O_3 in both air and nitrogen. See figure 3.8.

On the other hand, the reaction between stoichiometric amounts of Li_2CO_3 and Mn_2O_3 (1:2) in nitrogen produced a different TG trace to that run in air. The first slow mass loss of 12.84% starting at 400 °C and finishing at 720 °C was followed by an immediate small weight loss of 2.6% between 770 °C and 850 °C.

The stoichiometric mixture was heated up in nitrogen and annealed at 750 and 900 °C (as indicated by the arrows in Figure 3.6) for x-ray analysis purposes. X-ray diffraction studies of the products obtained at these temperatures yielded completely different diffraction patterns from that of spinel $LiMn_2O_4$, as can be seen in Figure 3.7. The d-values of the diffraction lines shown in Figure 3.7 are listed in Table 3.1.

It is obvious from the diffraction patterns that the products at 750 and 900 °C are different from $LiMn_2O_4$. The first weight loss of about 12.5% could be assigned to the loss of one molecule of carbon dioxide CO_2 resulting in formation of the oxygen deficient oxide $LiMn_2O_{3.5}$ or $Li_2Mn_4O_7$. The second small change of about 2.6% observed with increasing temperature is the result of further oxygen release from the oxide to form a lithium manganese oxide with more oxygen deficiency, $LiMn_2O_3$ or $Li_2Mn_4O_6$. The over all reaction path can be summarised by Equation 3.7.

$$Li_2CO_3 + 2Mn_2O_3 \xrightarrow{\sim 600\,^{\circ}C} Li_2Mn_4O_7 + CO_2 \xrightarrow{\sim 820\,^{\circ}C} Li_2Mn_4O_6 + \tfrac{1}{2}O_2 \qquad 3.7$$

Figure 3.7 X-ray diffraction pattern of (a) $LiMn_2O_4$, (b) Li_2CO_3+Mn_2O_3 at 750 °C, and (c) Li_2CO_3+Mn_2O_3 at 900 °C.

e) Effect of Grinding on Sample Quality

Grinding the stoichiometric mixtures during annealing treatment is found to improve the cathode material's performance, since grinding gets rid of any localised patches of the starting materials which might result in electrochemically inactive by-products, e.g. Mn_2O_3, Li_2MnO_3 and $LiMnO_2$ [53].

Since these materials are thermodynamically stable in the temperature range 500-1000°C in an inert atmosphere [54], localised zones of the above materials would hinder the reactions in Equations 3.4 and 3.5. Therefore, grinding the sample during the firing period should be considered as an important factor in order to prepare a single-phase spinel $LiMn_2O_4$.

Table 3.1 X-ray diffraction data for $LiMn_2O_4$, $LiMn_2O_{3.5}$ and $LiMn_2O_3$ derived from the x-ray diffraction photograph shown in Figure 3.7.

$LiMn_2O_4$ d-values	I	$LiMn_2O_{3.5}$ d-values	I	$LiMn_2O_3$ d-values	I
4.73	10	5.77	5	5.78	7
2.93	1	4.95	3	4.95	3
2.49	10	4.75	8	3.10	4
2.38	4	3.10	4	2.89	2
2.07	10	2.89	2	2.78	7
1.899	4	2.78	6	2.53	2
1.592	6	2.53	1	2.49	9
1.465	8	2.50	8	2.44	0.5
		2.45	0.5	2.40	0.5
		2.40	0.5	2.37	3
		2.375	1	2.30	4
		2.310	2	2.04	3
		2.07	2	2.02	7
		2.04	2	1.925	0.5
		2.02	5	1.835	0.5
		1.90	0.5	1.805	1
		1.836	0.5	1.710	1
		1.805	1	1.648	0.5
		1.709	1	1.580	2
		1.648	0.5	1.550	4
		1.582	1	1.515	4
		1.550	3	1.505	0.5
		1.517	3	1.480	0.5
		1.469	2		

3.2.2 The Final Preparation and Characterisation of $LiMn_2O_4$

The results obtained from the above initial thermal studies were used to optimise the preparation conditions for the spinel $LiMn_2O_4$. The procedure can be summarised as follows.

Stoichiometric amounts of a lithium source (Li_2CO_3 or $LiNO_3$) and Mn_2O_3 were mixed in a Li/Mn molar ratio of 0.5. The two powders were pre-mixed thoroughly using a ball mill with steel balls. Cyclohexane was added to the contents of the ball mill and the mixture ground for 3 hours to form a homogeneous paste of the reactants. The paste was then placed in a porcelain crucible and pre-heated in air for six hours at about 500 °C for $LiNO_3$ and 700 °C for Li_2CO_3. The solid was then ground and heated up to 900 °C for 48 hours. The mixture was repeatedly ground and reacted at the same temperature four times or until the sample had reached a constant weight. The sample was then allowed to cool down gradually to room temperature inside the open-end tube furnace, which was used for both the pre-heating and the final firing treatments. The result of this reaction was a bluish-black powder of the spinel $LiMn_2O_4$ as confirmed by x-ray diffraction and chemical analysis.

X-ray Powder Diffraction

The x-ray diffraction pattern obtained from the sample prepared by the methods above revealed that a single spinel phase has been produced (Figure 3.8), and corresponded to the $LiMn_2O_4$ pattern in J.C.P.D.S. file 35-782. d-values/Å of the patterns shown in Figure 3.8 and the d-values/Å of $LiMn_2O_4$ from J.C.P.D.S. file 35-782 are listed in Table 3.2 for comparison.

(a)
(b)
(c)

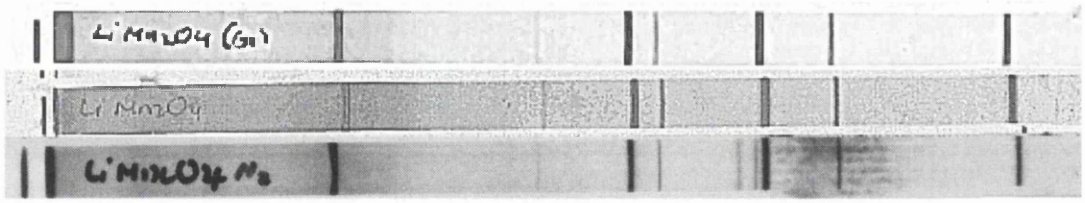

Figure 3.8 X-ray diffraction pattern for $LiMn_2O_4$ obtained from (a) Li_2CO_3 and Mn_2O_3 in air,(b) $LiNO_3$ and Mn_2O_3 in air, and (c) $LiNO_3$ and Mn_2O_3 in nitrogen (The difference in line positions between a, b and c is due to graphical reproduction of the images).

Table 3.2 X-ray diffraction data for $LiMn_2O_4$ prepared using Li_2CO_3 or $LiNO_3$ and Mn_2O_3.

hkl	$LiMn_2O_4$ JCPDS file No. 35-782		$LiMn_2O_4$ Experimental	
	d-values	I	$Li_2CO_3+Mn_2O_3$ d-values	$LiNO_3+Mn_2O_3$ d-values
111	4.764	100	4.75	4.75
220	2.914	<1	-	-
311	2.494	38	2.49	2.48
222	2.381	10	2.38	2.38
400	2.0621	33	2.07	2.07
331	1.8921	7	1.885	1.890
333	1.5874	10	1.582	1.590
440	1.4581	16	1.458	1.459
531	1.3941	7	1.390	1.390

X-ray diffraction data indicate that both Li_2CO_3 and $LiNO_3$ when heated with Mn_2O_3 give a single-phase spinel which corresponds to lithium manganese oxide $LiMn_2O_4$ with unit cell dimension of a = 8.24 Å and 8.276 Å respectively.

Spinels usually give an x-ray diffraction pattern containing the [220] Bragg reflection. This reflection is absent here because of the low scattering power for x-rays of lithium, which occupies the tetrahedral sites in the spinel structure of $[Li]_{tet}$ $[Mn_2]_{oct}O_4$. This reflection is very sensitive to any cation mixing [9], and should therefore appear if any Mn ion occupies a tetrahedral site. No evidence for that reflection was found in all x-ray photographs of $LiMn_2O_4$, which leads to the conclusion that lithium manganese oxide as prepared in this work has the normal spinel structure where all the lithium ions occupy tetrahedral sites and manganese occupies octahedral sites.

It is, however, impossible to rule out a small percentage of cation mixing, as the ability to detect the [220] reflection is limited by the resolution of the Guinier-de Wolf powder x-ray diffraction camera used.

The degree of cation mixing can also be estimated using the ratio of the intensities of reflections [311] and [111] that should increase with increasing cation mixing, in comparison to a [311]/[111] ratio of 0.37 for pure $LiMn_2O_4$ [9]. Tarascon *et al.* [9] recorded a ratio of 0.47, indicating cation mixing of no more than 10%, i.e. $[Li_{0.9}$ $Mn_{0.1}]_{tet}$ $[Mn_{1.9}$ $Li_{0.1}]_{oct}$ O_4. The intensities of Bragg reflections [311] and [111] for both diffraction photographs shown in Figure 3.6 were visually estimated, and the [311] / [111] ratios found to be about 0.4. This ratio indicates that both samples of $LiMn_2O_4$ do have a very small percentage of cation mixing, but not enough to cause Bragg reflection [220] to appear in the diffraction pattern.

Xia *et al.* [52] found that both capacity and rechargeability depends on the value of the unit cell dimension (a). A small unit cell dimension would lead to low capacity and

excellent rechargeability, and should be in the range 8.23-8.24 Å. The spinel oxides prepared in this work have unit cell dimensions within or near to this range: 8.24 Å and 8.276 Å for $LiMn_2O_4$ prepared using Li_2CO_3+Mn_2O_3 and $LiNO_3$ + Mn_2O_3 respectively.

Chemical Analysis and Surface Area Measurements

Lithium, manganese and manganese dioxide contents in both samples were determined as described in Chapter 2. The experimental values of lithium and manganese in both oxides are in good agreement with the theoretical values of $LiMn_2O_4$ and with those published before [49, 55]. The results are presented in Table 3.3.

Table 3.3 Chemical composition and specific surface area (SSA) of $LiMn_2O_4$.

$LiMn_2O_4$	% Li	% Mn	% MnO_2	SSA $m^2\ g^{-1}$
Theoretical	3.8	60.8	72.1	-
Literature [49]	3.8	60.7	71.6 [50]	2.0
$Li_2CO_3 + Mn_2O_3$	3.7	60.7	71.8 ±0.5	7.6 ±1.3
$LiNO_3 + Mn_2O_3$	3.7	60.7	71.7 ±0.7	4.3 ±1.4

Surface area measurements were carried out using the single point method as described in Chapter 2. The experimental surface area measurements for both oxides showed that $LiMn_2O_4$ prepared using Li_2CO_3 and Mn_2O_3 has a specific surface area of 7.6 ±1.3 $m^2\ g^{-1}$ while that prepared from $LiNO_3$ and Mn_2O_3 has a specific surface area of 4.3 ±1.4 $m^2\ g^{-1}$. The lithium manganese oxide prepared using Li_2CO_3 exhibited an attractive high surface area since it has been described as the main factor for the high performance of lithium manganese oxide cathodes in non-aqueous lithium cells [5, 6, 7, 8, 9]. For this

reason, $LiMn_2O_4$ prepared using Li_2CO_3 and Mn_2O_3 was selected for all future preparations and investigations.

Electron Microscopy

Lithium manganese oxide $LiMn_2O_4$ was observed under the scanning electron microscope (SEM). An enlarged image (x2000) of the oxide was recorded on the micrograph shown in Figure 3.9. The image shows that $LiMn_2O_4$ has a particle size ranging from 0.5 to 10 μm.

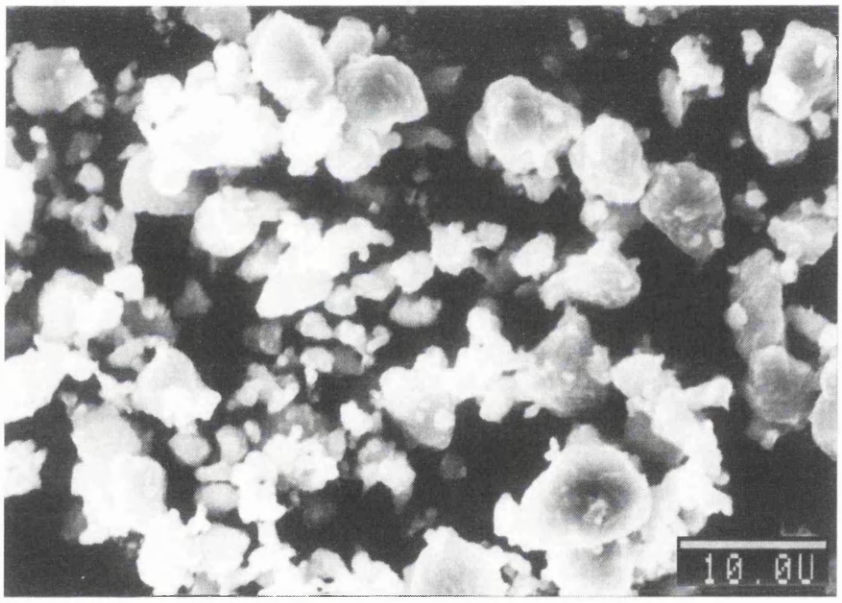

Figure 3.9 Electron microscope photograph of $LiMn_2O_4$ obtained from Li_2CO_3 and Mn_2O_3, x2000.

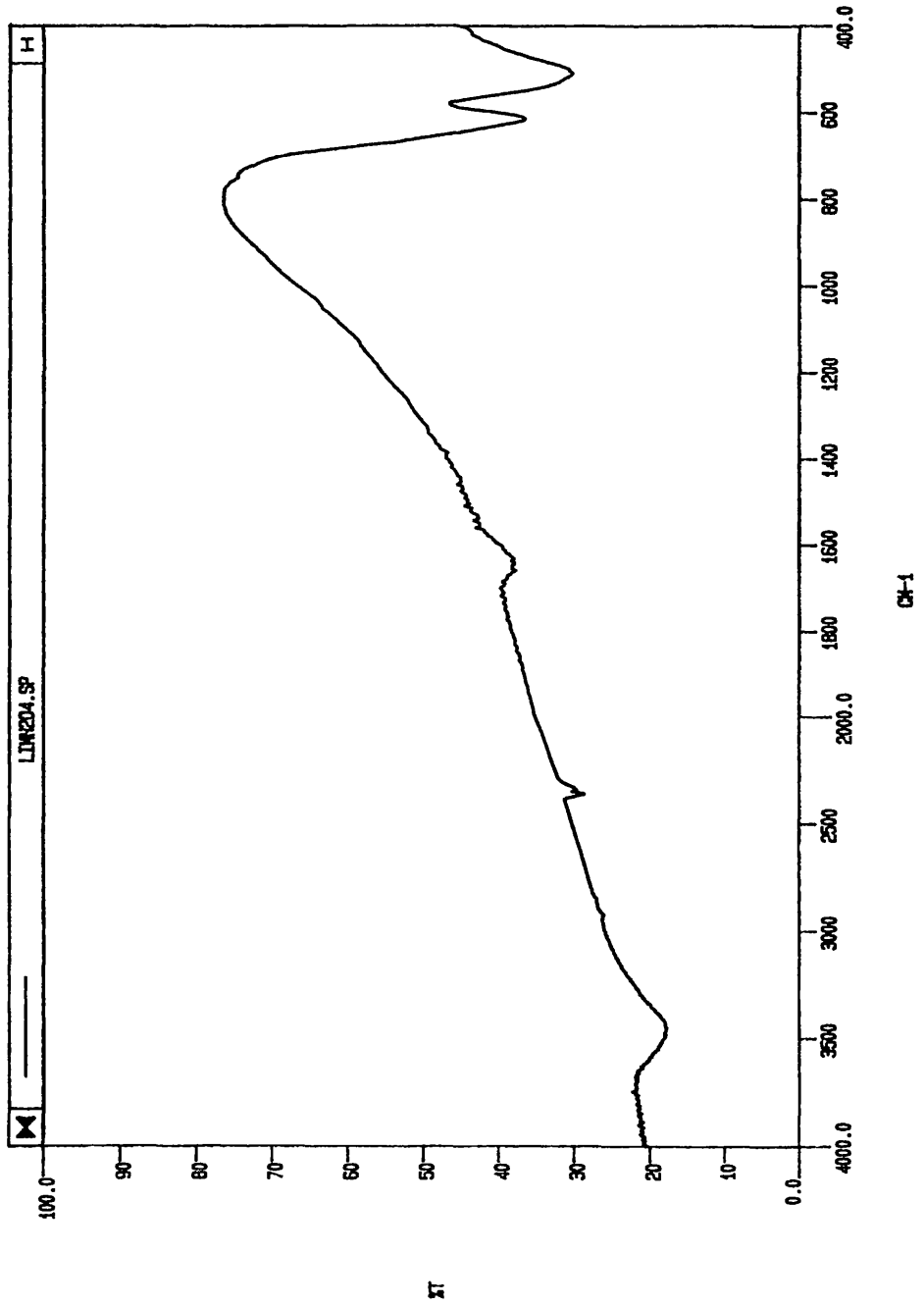

Figure 3.10 FTIR spectrum of $LiMn_2O_4$ obtained from Li_2CO_3 and Mn_2O_3.

FTIR Spectroscopy of Spinel $LiMn_2O_4$

A sample of $LiMn_2O_4$ was examined by FTIR spectroscopy at room temperature (Figure 3.10), and the spectrum is in good agreement with that previously published [14]. The spectrum consists of a few bands located at 500, 620, 1650, 2300, 2350 and 3450 cm^{-1}.

For oxide spinels, it is difficult to assign a specific band to a cation and its oxide neighbours because of the contribution of all the atoms in the structure to the vibrational modes. The big difference in mass, charge and covalence between the cations in the lithium-containing spinels could, however, make the modes involving the motion of the lithium ion more dominant than the others. The FTIR spectra of $LiMn_2O_4$, as well as those of λ-MnO_2 and λ-MnOOH can be understood in terms of contributions from tetrahedral LiO_4 units (600-650 cm^{-1}), octahedral LiO_6 units (350-400 cm^{-1}) and octahedral (500-600 cm^{-1}) or tetragonally distorted octahedral (550-600 and *ca.* 450-500 cm^{-1}) MnO_6 units [56].

Despite the above classification, the powerful coupling in spinels between the vibrations of the tetrahedral LiO_4 units and those of the octahedral MnO_6 units prevents the assignment of any absorption band to any particular part of the structure. The coupling between the tetrahedral and octahedral units is believed to be caused by the fact that the oxide ions at the corners of the AO_4 units are also at the corners of the BO_6 units [57]. A recent study [58] of the oxides $LiMn_2O_4$ and $Li_{0.1}Mn_2O_4$ using samples isotopically enriched with ^6Li indicated very little or no effect on the FTIR spectra. Thus despite the contribution of lithium ions to the vibrational modes, manganese oxides are the

dominant factor and their frequencies are decided mainly by the co-ordination geometry and the bond lengths of the MnO_6 unit.

The two bands centred at 500 and 610 cm^{-1} indicate a sample of $LiMn_2O_4$ with high local symmetry, and therefore will be used to show the spectral change caused by lithium extraction from $LiMn_2O_4$. The bands observed at 1650 and 3450 cm^{-1} could be assigned to the O-H bending and stretching vibrations of some adsorbed water. [14, 59, 60]. The bands at 2300 and 2350 cm^{-1} are due to CO_2 that is adsorbed and possibly present in the background and not completely removed by subtraction.

3.2.3 Thermal Stability of Spinel $LiMn_2O_4$ at Elevated Temperatures

Thermal analysis techniques were shown to be essential and valuable tools in the characterisation of $LiMn_2O_4$ [61]. The behaviour of spinel $LiMn_2O_4$ at elevated temperatures was examined in nitrogen and air using the Stanton Redcroft thermal analyser described in Chapter 2. The samples were heated at rate of 10 °C per minute from room temperature to 1200 °C. Typical weight loss thermograms are presented in Figure 3.11.

During heating in air, the sample was stable until about 800 °C, then decreased in mass rapidly by as much as 6.33% at about 1000 °C. In nitrogen the shape of the mass loss curve is similar to that in air, but the decrease starts at 700 °C instead of 800 °C, and reaches a value of 5.7% at about 1000 °C. The mass loss observed in both curves could be attributed to the decomposition of $LiMn_2O_4$ to $LiMnO_2$ and Mn_3O_4 [9, 62]. The

decomposition of spinel $LiMn_2O_4$ corresponds to a theoretical mass loss of 6%, and can be summarised by Equation 3.8.

$$3LiMn_2O_4 \longrightarrow 3LiMnO_2 + Mn_3O_4 + O_2 \qquad 3.8$$

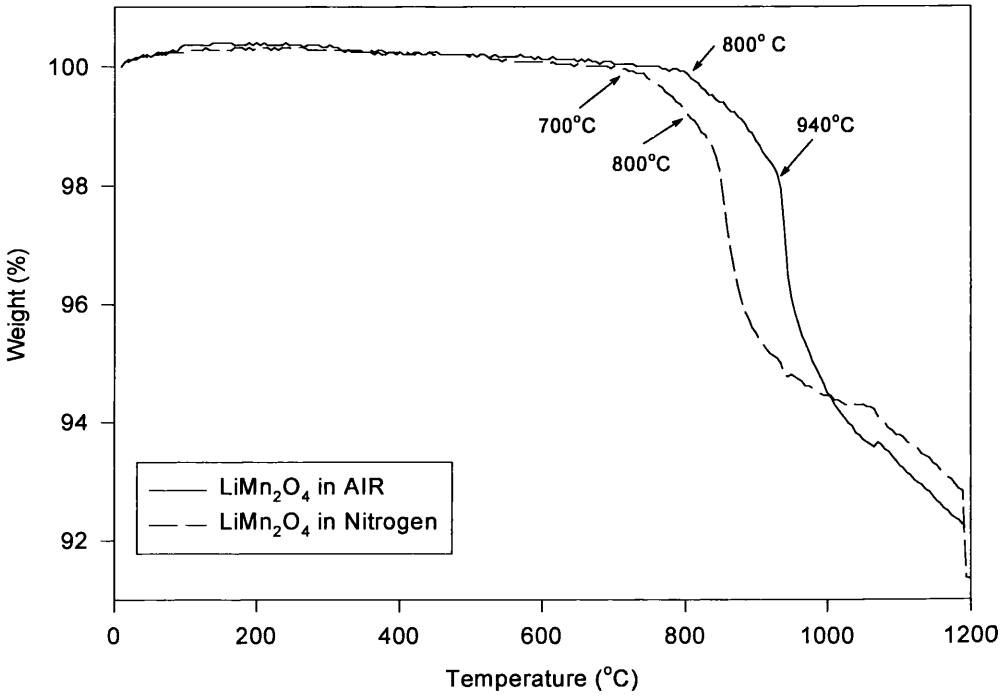

Figure 3.11 Thermogravimetric Analysis (TGA) of $LiMn_2O_4$ obtained from Li_2CO_3 and Mn_2O_3 heated in nitrogen or air at a rate of 10 °C per minute from room temperature to 1200 °C.

It is clear that the nitrogen atmosphere encourages the above reaction, which explains the earlier mass loss when $LiMn_2O_4$ was heated under nitrogen.

To confirm the above reaction, a sample of spinel $LiMn_2O_4$ prepared from Li_2CO_3 and Mn_2O_3 was heated from room temperature up to 1000 °C and annealed at this temperature for 15 minutes. The sample was then allowed to cool under nitrogen to room temperature. X-ray diffraction examination revealed that only the two expected phases of the orthorhombic $LiMnO_2$ and the tetragonal Mn_3O_4 were present (see Figure 3.12).

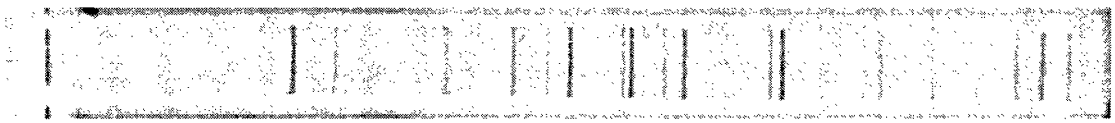

Figure 3.12 X-ray diffraction photograph of sample $LiMn_2O_4$ heated up to about 1000°C in nitrogen.

The d-values/Å derived from the x-ray diffraction lines shown in Figure 3.12 are listed in Table 3.4, along with the corresponding d-values of the orthorhombic $LiMnO_2$ and the tetragonal Mn_3O_4. The values listed for $LiMnO_2$ and Mn_3O_4 were obtained from the JCPDS-ICDD files 23-361 and 24-734 respectively.

From table 3.4 we can see clearly that all the reflections may be assigned to either $LiMnO_2$ or Mn_3O_4, indicating compliance of the $LiMn_2O_4$ decomposition with Equation 3.7, apart from the faint reflection at 2.78 Å which might be assigned to reflection [111] in $LiMn_2O_4$. The appearance of reflection [111] in the diffraction pattern would suggest the existence of small amounts of $LiMn_2O_4$ trapped inside the particles during the heating process. The product of heating $LiMn_2O_4$ to 1000 °C has been examined under

the scanning electron microscope and the result is shown in Figure 3.13. The SEM photograph revealed that heating $LiMn_2O_4$ to 1000 °C has caused the particles to change into somewhat rounded shapes with a tendency toward accumulation.

Table 3.4 d-values/Å of sample of $LiMn_2O_4$ heated up to about 1000 °C in nitrogen, derived from the x-ray diffraction photograph shown in Figure 3.12.

$LiMn_2O_4$ At 1000 °C	I	$LiMnO_2$ 23-361	I	Mn_3O_4 24-734	I
5.70	10	5.80	10		
4.90	3			4.924	3
4.78	1	*	*	*	*
3.58	3	3.62	7		
3.08	5			3.089	4
2.88	2			2.881	1.7
2.77	8			2.768	8.5
2.53	2	2.533	2		
2.49	10			2.487	10
2.44	1	2.444	1.5		
2.39	1	2.405	1		
2.37	3			2.367	2
2.29	8	2.298	6		
2.22	0.5	2.220	3		
2.04	3			2.0369	2
2.02	8	2.017	7		
1.920	0.5	1.923	0.5		
1.825	0.5			1.8288	0.7
1.795	2			1.7988	2.5
1.705	0.5			1.7008	1
1.642	0.5			1.6405	0.8
1.575	3			1.5762	2.5
1.542	4			1.5443	5
1.510	4	1.510	5		
1.495	0.5	1.495	1.5		

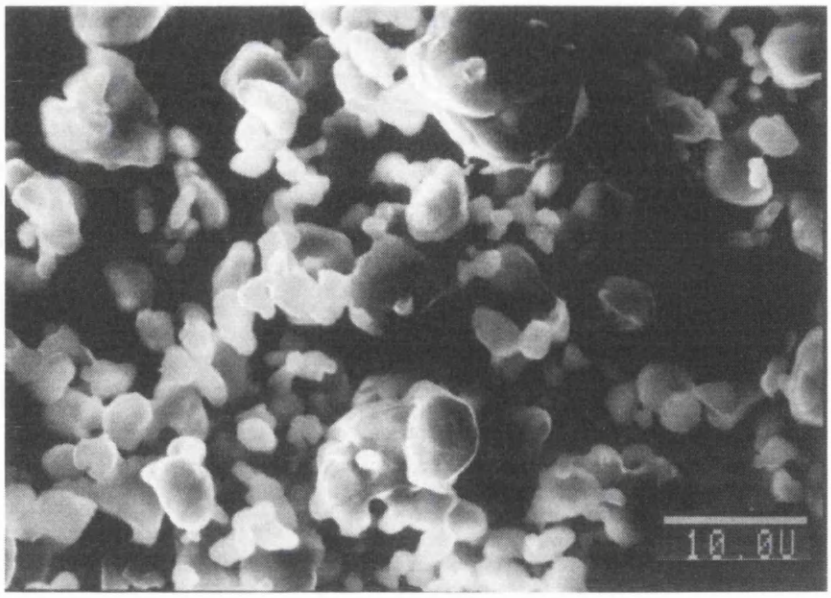

Figure 3.13 Electron microscope photograph of $LiMn_2O_4$ heated up to 1000 °C, x2000.

The nature of the weight loss was further investigated by heating a sample of $LiMn_2O_4$ in nitrogen at a rate of 0.5 °C per minute from 650 to 900 °C. The TGA trace (Figure 3.14) shows a non-uniform weight loss with increasing temperature with a sudden change in slope around 770 °C. The weight loss suffered by $LiMn_2O_4$ was revealed to consist of three parts as shown by plotting the derivative of the TGA trace (Figure 3.14). The first change in weight is a small and gradual weight loss of about 0.75% for a temperature up to 770 °C. The second major weight loss of about 3.7% takes place between 770 and 795 °C, followed immediately by another weight loss of about 1.68% between 795 and 810 °C. The total estimated weight loss found above is 6.13% which agrees very well with the theoretical value of 6% for the decomposition reaction of $LiMn_2O_4$ (Equation 3.8).

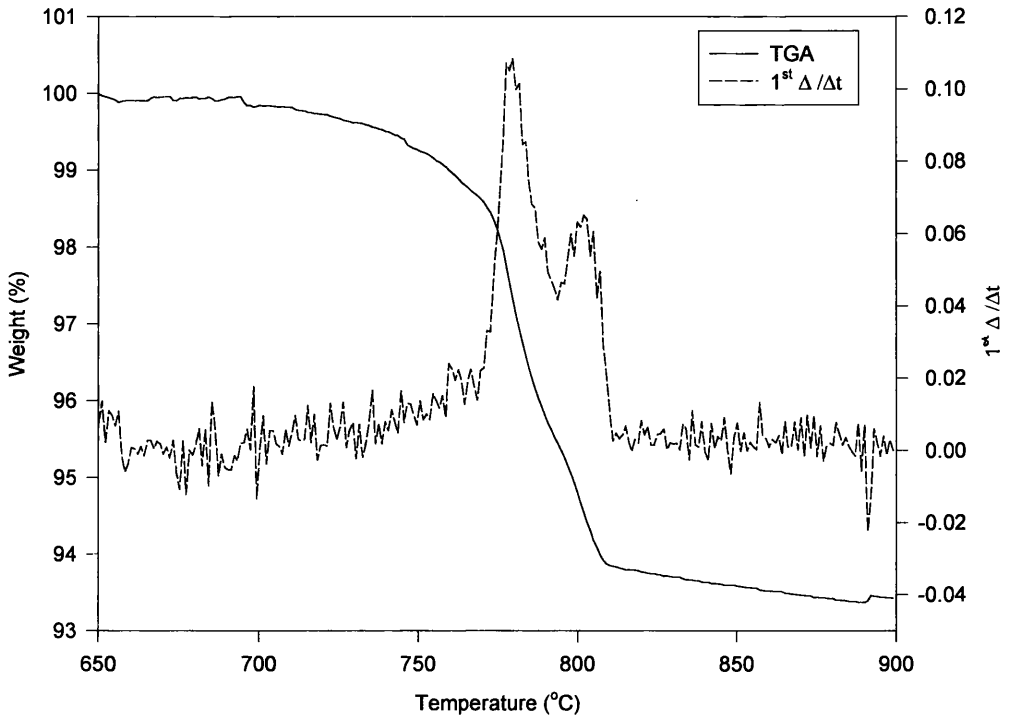

Figure 3.14 The TGA trace and its derivative for $LiMn_2O_4$ when heated in nitrogen from 650 to 900 °C at a rate of 0.5 °C per minute.

The sharp peaks in the derivative plot suggest a first-order phase transition, possibly induced by the loss of oxygen and the rearrangement of oxygen vacancies during the heating procedure [63]. The change in slope found in the derivative curve shows clearly that the sample remains single phase until the temperature reaches ~770 °C, and after that another single phase domain exists within the narrow range 770 to 795 °C. Guyomard and Tarascon [53] and Tarascon *et al.* [9] have shown that $LiMn_2O_4$ quenched from temperatures between 750 and 800 °C has a tetragonal spinel structure, so the change in weight at 770 °C could indicate the beginning of the cubic-tetragonal distortion.

The first weight loss at 770 °C of 0.75% compared to the starting cubic phase is equivalent to 0.085 oxygen atoms per formula unit. If the cubic starting material is stoichiometric, the new phase is $LiMn_2O_{3.92}$. This oxygen loss is accompanied by the reduction of 0.17 Mn^{4+} to Mn^{3+} in order to balance the charges, so the formula for the new cubic spinel could be written as $LiMn^{3+}_{1.17}.Mn^{4+}_{0.83}O_{3.92}$.

Further weight loss between 770 and 795 °C of 3.7%, which is equivalent to 0.42 oxygen atoms per formula unit results in formation of the tetragonal spinel phase $LiMn_2O_{3.5}$. The latest oxygen loss is accompanied by the reduction of all of the remaining 0.83 Mn^{4+} to Mn^{3+}. A cubic to tetragonal transformation that maintains a spinel structure happens when the number of Mn^{3+} ions per formula unit increases above 1.17. This result could be explained by the action of a co-operative Jahn-Teller effect of the Mn^{3+} ions in octahedral sites [64].

The third weight loss of 1.68%, which starts at 795 °C, is equivalent to 0.19 oxygen atoms per formula unit and corresponds to the transformation of the tetragonal spinel to orthorhombic $LiMnO_2$ and tetragonal Mn_3O_4 (theoretically equivalent to $LiMn_2O_{3.33}$). The existence of the above two phases has been confirmed by x-ray diffraction examination of a sample of $LiMn_2O_4$ heated to 1000 °C.

The reversibility of the oxygen weight loss was tested by heating samples of $LiMn_2O_4$ in nitrogen at 10 °C /min to *ca.* 1000 and 1200 °C. The samples were annealed at these temperatures for 15 minutes before allowing them to cool in air at the same rate. Figure 3.15 shows the weight loss versus temperature curve for a sample of $LiMn_2O_4$ heated up to ~1080 °C.

On the heating part of the curve the weight started to decline noticeably at the first onset temperature (T_{h1}= 700 °C) and then declines rapidly again at the second onset temperature (T_{h2}= 800 °C) followed by a small change at T_{h3} of about 900 °C. These weight changes are identical to those shown in Figure 3.11 and are attributed to the oxygen loss in this temperature range as discussed earlier.

On the cooling part of the curve, the sample gained weight indicating the uptake of oxygen. Unlike the heating part of the curve, there are only two onset temperatures (T_{c1}= 1020 °C and T_{c2}= 885 °C) during cooling part. The two onset points in the cooling part of the curve, T_{c1}= 1020 °C and T_{c2}= 885 °C, correspond to the third (T_{h3}= 900 °C) and the second (T_{h2}=800 °C) onset temperatures on the heating part of the curve, respectively. On the other hand the first onset temperature on the heating part of the curve does not have a counterpart on the cooling part of the curve [63, 65]. These onset temperatures correspond to the change in crystal structure resulting from oxygen mobility during the heating-cooling cycle. These temperatures mark the start of the structural changes cubic ↔ tetragonal ↔ orthorhombic/tetragonal, which were discussed earlier.

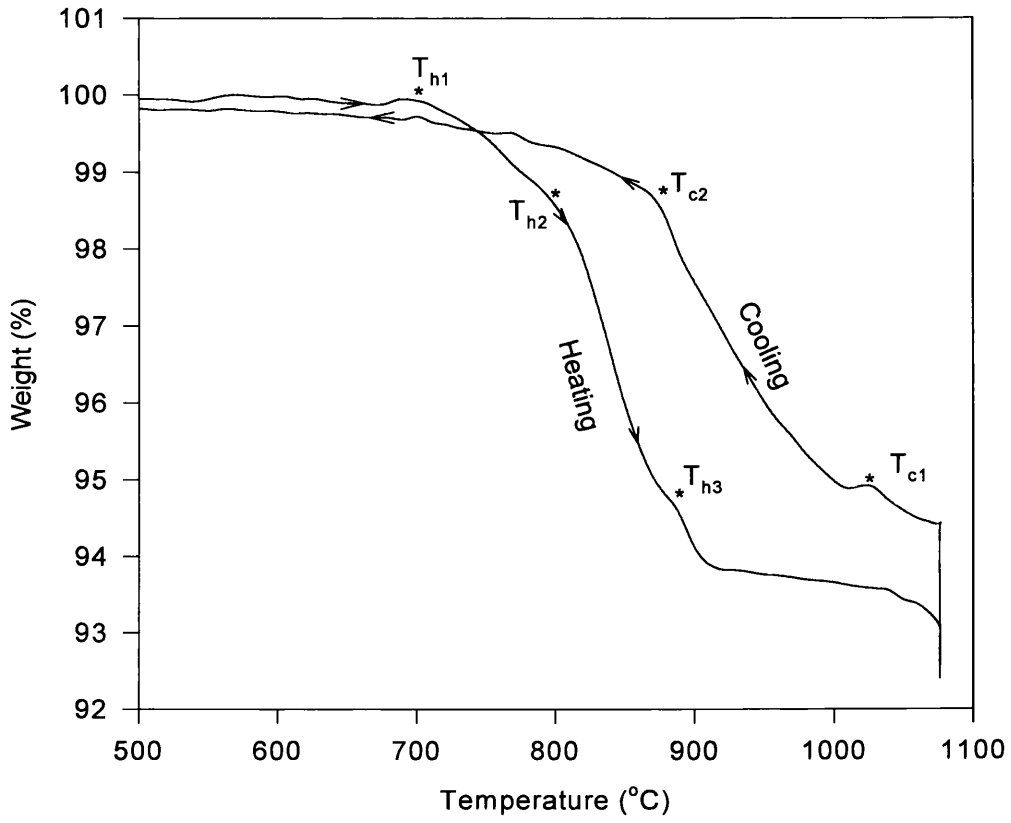

Figure 3.15 The TGA heating and cooling curve for $LiMn_2O_4$ to / from 1080 °C at a rate of 0.5 °C per minute.

Figure 3.15 shows that the sample recovered most of the oxygen lost during the heating process. The net weight loss (Δw) recorded after cooling the sample in air is only 0.23% ±0.05%, indicating that the orthorhombic $LiMnO_2$ and the tetragonal Mn_3O_4 mixture produced by heating $LiMn_2O_4$ in nitrogen can capture the lost oxygen into the crystal structure to form the original cubic spinel $LiMn_2O_4$.

A sample of the air-cooled product has been examined by x-ray diffraction and found to have a diffraction pattern identical to that of the original cubic spinel $LiMn_2O_4$, as can be seen in Figure 3.16.

Figure 3.16 $LiMn_2O_4$ after heating to 1000 °C in nitrogen and cooling in air at a rate of 0.5 °C per minute.

Therefore the dissociation reaction of $LiMn_2O_4$ at high temperatures (reaction 3.8) is fully reversible at 1000 °C in the presence of oxygen, and could be expressed by the relationship below.

$$3LiMn_2O_4 \longleftrightarrow 3LiMnO_2 + Mn_3O_4 + O_2 \qquad 3.9$$

In order to test the reversibility of reaction 3.9 at higher temperatures, a sample of $LiMn_2O_4$ was heated in nitrogen to 1200 °C (the limit of our TGA instrument) and annealed at that temperature for 15 minutes before allowing the sample to cool in air. The path of the heating-cooling process is illustrated by the weight-temperature curve at 1200 °C shown in Figure 3.17.

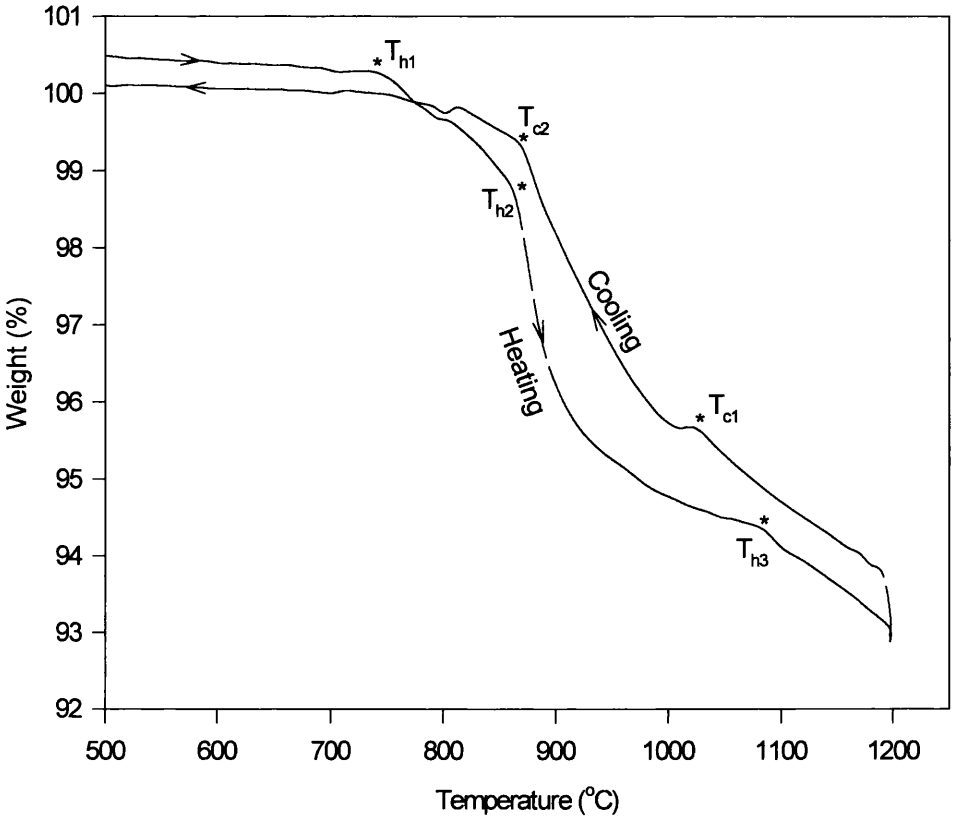

Figure 3.17 The TGA heating and cooling curve for $LiMn_2O_4$ to / from 1200 °C at a rate of 0.5 °C per minute.

Figure 3.17 shows that heating a sample of $LiMn_2O_4$ in nitrogen up to 1200 °C followed by a subsequent cooling in air causes the sample to lose and regain oxygen reversibly within the net weight loss (Δw) recorded after heating and cooling up to 1000 °C, 0.23% ±0.05%. X-ray diffraction examination of the above sample confirmed the formation of cubic spinel $LiMn_2O_4$ following cooling of the sample in air from 1200 °C, as can be seen in Figure 3.18.

Figure 3.18 $LiMn_2O_4$ after heating to 1200 °C in nitrogen and cooling in air at a rate of 0.5 °C per minute.

The above results confirm that the spinel lithium manganese oxide $LiMn_2O_4$ prepared using the method above is thermally unstable at high temperatures and the loss of oxygen suffered as a result (reaction 3.8) is fully reversible for temperatures up to 1200 °C (the limit of the TGA instrument). The mechanism of the transformation of the cubic spinel $LiMn_2O_4$ to the orthorhombic $LiMnO_2$ and the tetragonal Mn_3O_4 is not fully understood and in need of further investigation. The structural changes due to the loss and uptake of oxygen discussed above can be summarised by the diagram below.

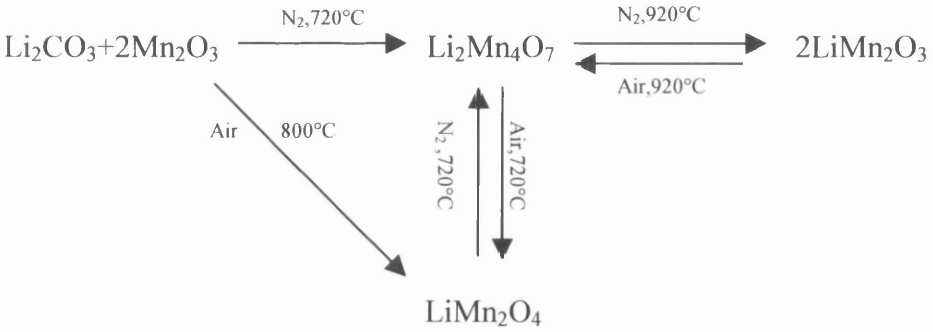

3.3 Conclusion

The preparation method of lithium manganese oxide $LiMn_2O_4$ has been modified to produce an oxide with a high surface area. The product of the above procedure was examined by powder x-ray diffraction and confirmed to be the single-phase spinel lithium manganese oxide $LiMn_2O_4$ with lattice constant of a = 8.24 Å. The prepared $LiMn_2O_4$ oxide was found to have a specific surface area of 7.6 ±1.3 $m^2\ g^{-1}$ as confirmed by the single point BET method. $LiMn_2O_4$ was found to be thermally stable up to about 700 °C at which point oxygen was lost. The loss of oxygen was found to be reversible up to 1200 °C when the sample cooled in air. Further investigation into the electrochemical properties of the oxide prepared using the modified firing technique is needed as it is outside the scope of this thesis.

$LiMn_2O_4$ prepared in this chapter will be used throughout this work. The chemical compositions and the specific surface areas (SSA) of $LiMn_2O_4$ are summarised in Table 3.5.

Table 3.5 Chemical compositions and specific surface areas (SSA) of $LiMn_2O_4$.

$LiMn_2O_4$	% Li	% Mn	% MnO_2	SSA $m^2\ g^{-1}$
Theoretical	3.8	60.8	72.1	-
Literature [49]	3.8	60.7	71.6 [50]	2.0
$Li_2CO_3 + Mn_2O_3$	3.7	60.8	71.8 ±0.5	7.6 ±1.3
$LiNO_3 + Mn_2O_3$	3.7	60.7	71.7 ±0.7	1.4 ±1.4

References

1 K.M. Parida, S.B. Kanungo, and B.R. Sant, *Electrochimica Acta*, **26**, 435 (1981).

2 T. Nagaura and T. Tozawa, *Prog. Batteries Solar Cells*, **9**, 209 (1990).

3 K. Brandt, *Solid State Ionics*, **69**, 173 (1994).

4 G. Pistoia and R. Rosati, *J. Power Sources*, **58**, 135 (1996).

5 G. Pistoia, *12th Int. Seminar Primary and Secondary Battery Technology and Application,* Mar. 1995, Deerfield Beach, FL, USA.

6 D. Guyomard and J.M. Tarascon, *J. Electrochem.* Soc., **139**, 937 (1992).

7 K. Mizoshima, P.C. Jones, P.J. Wiseman, and J.B. Goodenough, *Mat. Res. Bull.*, **15**, 783 (1980).

8 A. Momchilov, V. Manev, A. Nassalevska, and A. Kozawa, *J. Power Sources*, **41**, 305 (1993).

9 J.M. Tarascon, W.R. Mckinnon, F. Coowar, T.N. Bowmer, G. Amatucci, and D. Guyomard, *J. Electrochem. Soc.,* **141**, 1421 (1994).

10 D. Wickham and W. Croft, *J. Phys. Chem. Solids*, **7**, 351 (1958).

11 V.I. Ezikyan, G.P. Ereiskaya, U.V. Ivanov, and A.M. Kolomoets, *Langmuir*, **25**, 795 (1989).

12 V. Manev, A. Momchilov, A. Nassalevska, and A. Sato, *J. Power Sources,* **54**, 323 (1995).

13 A. Momchilov, V. Manev, A. Nassalevska, and A. Kozawa, *J. Power Sources,* **43/44**, 551 (1993).

14 Q. Feng, Y. Miyai, H. Kano, and K. Ooi, *Langmuir*, **8**, 1861 (1992).

15 T. Tsumura, A. Shimizu, and M. Inagaki, *J. Mater. Chem.*, **3**, 995 (1993).

16 L. Chen, X. Huang, E. Kelder, and J. Schoonmann, *Solid State Ionics*, **76**, 91 (1995).

17 X.M. Wu, X.H. Li, Z.B. Xiao, J. Liu, W.B. Yan, and M.Y. Ma, *Materials Chemistry and Physics*, **84**, 182 (2004).

18 C. Wan, Y. Nuli, Q. Wu, M. Yan, and Z. Jiang, *J. Appl. Electrochem.*, **33**, 107 (2003).

19 S.W. Jang, H.Y. Lee, K.C. Shin, S.M. Lee, J.K. Lee, S.J. Lee, H.K. Baik and D.S. Rhee, *J. Power Sources*, **88**, 274 (2000).

20 V. Massarotti, D. Capsoni, M. Bini, G. Chiodelli, C.B. Azzoni, M.C. Mozzati. and A. Paleari, *J. Solid State Chem*, **147**, 509 (1999).

21 X. Wang, X. Chen, L. Gao, H. Zheng, M. Ji, T. Shen, and Z. Zhang, *J. Crystal Growth*, **256**, 123 (2003).

22 K. Du and H. Zhang, *J. Alloys and Compounds*, **352**, 250 (2003).

23 B.J. Hwang, R. Santhanam and D.G. Liu, *J. Power Sources*, **101**, 86 (2001).

24 J.H. Choy, D.H. Kim, C.W. Kwon, S.J. Hwang, and Y.I. Kim, *J. Power Sources*, **77**, 1 (1999).

25 T. Tsumura, A. Shimizu, and M. Inagaki, *Solid State Ionics*, **90**, 197 (1996).

26 Y.M. Hon, H.Y. Chung, K.Z. Fung, and M.H. Hon, *J. Solid State Chem.*, **160**, 368 (2001).

27 Y.M. Hon, S.P. Lin, K.Z. Fung, and M.H. Hon, *J. European Ceramic Soc.*, **22**, 653 (2002).

28 Y.M. Hon, K.Z. Fung, S.P. Lin, and M.H. Hon, *J. Solid State Chem.*, **163**, 231 (2002).

29 T. Tsumura and M. Inagaki, *Solid State Ionics*, **104**, 35 (1997).

30 S.R.S. Prabaharan, S.S. Michael, and C. Julien, *Int. J. Inorg. Mater.*, **1**, 21 (1999).

31 W. Liu, G.C. Farrington, F. Chaput, and B. Dunn, *J. Eletrochem. Soc.*, **143**, 879 (1996).

32 S.Y. Han and G.H. Kim, *J. Power Sources*, **88**, 161 (2000).

33 D.G. Fauteux, A. Massucco, J. Shi, and C. Lampe-Onnerud, *J. Appl. Electrochem.*, **27**, 543 (1997).

34 W. Yang, G. Zhang, J. Xie, L. Yang, and Q. Liu, *J. Power Sources*, **81**, 412 (1999).

35 H.B. Park, J. Kim, and C.W. Lee, *J. Power Sources*, **92**, 124 (2001).

36 P. Kalyani, N. Kalaiselyi, and N. Muniyandi, *J. Power Sources*, **111**, 232 (2002).

37 I. Yamada, T. Abe, Y. Iriyama, and Z. Ogumi, *Electrochemistry Communications*, **5**, 502 (2003).

38 W.T. Jeong, J.H. Joo, and K.S. Lee, *J. Alloys and Compounds*, **358**, 294 (2003).

39 M. Nakayama, K. Watanabe, H. Ikuta, Y. Uchimoto, and M. Wakihara, *Solid State Ionics*, **164**, 35 (2003).

40 D. Shu, K.Y. Chung, W.I. Cho, and K.B. Kim, *J. Power Sources*, **114**, 253 (2003).

41 I. Taniguchi, C.K. Lim, D. Song, and M. Wakihara, *Solid State Ionics*, **146**, 239 (2002).

42 C. Fong, B.J. Kennedy, and M.M. Elcombe, *Zeit. für Kristall.*, **202**, 941 (1994).

43 J. Akimoto, Y. Takahashi, Y. Gotoh, and S. Mizuta, *J. Crystal Growth*, **229**, 405 (2001).

44 M.M. Thackeray, W.I.F. David, P.G. Bruce, and J.B. Goodenough, *Mat. Res. Bull.*, **18**, 461 (1983).

45 M.M. Thackeray, *J. Electrochem. Soc.*, **142**, 2558 (1995).

46 B. Scrosati, *Electrochim. Acta,* **45**, 2461 (2000).

47 J.M. Tarascon, E. Wang, F.K. Shokoohi, W.R. McKinnon, and S. Colson, *J. Electrochem. Soc.*, **138**, 2859 (1991).

48 J.H. Lee, J.K. Hong, D.H. Jang, Y.K. Sun, and S.M. Oh, *J. Power Sources,* **89**, 7 (2000).

49 J. Hunter, *J. Solid State Chem.*, **39**, 142 (1981).

50 T. Ohzuku, M. Kitagawa, and T. Hirai, *J. Electrochem. Soc.,* **137**, 769 (1990).

51 W. Howard, *Ext. Abstr., 7th Int. Meet. Lithium Batteries*, Boston, MA, USA, 15-20 May 1994, p. 281.

52 Y. Xia, H. Takeshiga, H. Noguchi, and M. Yoshio, *J. Power Sources,* **56**, 61(1995).

53 D. Guyomard and J.M. Tarascon, *Solid State Ionics*, **69**, 222 (1994).

54 M. Rossouw and M. Thackeray, *Mater. Res. Bull.,* **26**, 463 (1991).

55 T. Ohzuku, M. Kitagawa, and T. Hirai, *J. Electrochem. Soc.,* **137**, 769 (1990).

56 T.J. Richardson and P.N. Ross,Jr., *Mater. Res. Bull.*, **31**, 935 (1996).

57 J. Himmrich and H.D. Lutz, *Solid State Comm.*, **79**, 447 (1991).

58 T.J. Richardson, S.J. Wen, K.A. Striebel, P.N. Ross, Jr., and E.J. Cairns, *Mater. Res. Bull.*, **32**, 609 (1997).

59 R.M. Potter and G.R. Rossman, *Am. Mineral.*, **64**, 1199 (1979).

60 H.W. VanderMarel and H. Beutelspacher, *Atlas of Infrared Spectroscopy of Clay Minerals and their Admixtures*, Elsevier Scientific, Amsterdam (1976).

61 J.M. Amarilla and R.M. Rojas, *J. Thermal Analysis and Calorimetry*, **73**, 191 (2003).

62 V. Massarotti, D. Capsoni, and M. Bini, *Solid State Communications*, **122**, 317 (2002).

63 Y. Gao And J.R. Dahn, *Appl. Phys. Lett.*, **66**, 2487 (1995).

64 J.B. Goodenough, M. Thackeray, W.I.F. David, and P.G. Bruce, *Rev. Chim. Miner.*, **21**, 435 (1984).

65 M.M. Thackeray, M.F. Mansuetto, D.W. Dees, and D.R. Vissers, *Mat. Res. Bull.*, **31**, 133 (1996).

Preparation, Characterisation, and Study of Spinel Related Manganese Oxides - λ-MnO_2 and λ-MnOOH

The spinel materials λ-MnO_2 and λ-MnOOH were prepared and subsequently characterised using x-ray diffraction, electron microscopy, thermal analysis, FTIR spectroscopy, surface area measurements and chemical analysis. Details of the above study are presented in this Chapter.

4.1 Introduction

Manganese dioxides have been used widely as cathode materials in the Leclanché type dry cell, which is still probably the most popular and inexpensive source of current for a number of portable electronic products [1].

In recent years, lithium ion batteries have been developed widely and made commercially available as a result of an extensive academic and commercial effort [2, 3]. Some of that effort was concentrated on the introduction of manganese oxides into secondary lithium batteries. As a result of the above effort, the all-solid-state lithium – polymer battery was born and was commercially available in the mid 1970's [4].

For safety reasons, metallic lithium used in the cells above was replaced by a carbon based insertion electrode [5], which led to the birth of the Li-ion transfer cell [6]. In this cell, lithium is present as an ion rather than as a metal.

For a complete Li-ion cell, lithium ions will be contained by one electrode, and then transported reversibly between the electrodes as a result of the charge/discharge cycle. For the last few years, a range of electrodes has been examined [7, 8, 9] and the most commercially exploited electrode is the $LiCoO_2$ electrode [10] and its derivatives.

Materials that are good candidates for insertion electrodes are those with the ability to incorporate a guest ion. The guest ion should be able to move freely between sites in the solid host and to be removed and added easily, thus changing the guest-ion concentration. In lithium ion cells, Li^+ is the guest ion and the host material would be one of a large selection of transition metal oxides, chalcogenides (sulphides, selenides, or tellurides) or salts with oxoanions (phosphate, sulphate or arsenate). Due to their high potential and good reversibility, transition metal oxides were found to be the best candidates for insertion electrodes [11].

Lithium manganese oxides of various crystal structures are the simplest and the most studied insertion compounds e.g. $LiMnO_2$, $LiMn_2O_4$ and recently λ-MnO_2.

The spinel $LiMn_2O_4$ is usually prepared by mixing stoichiometric amounts of lithium salts such as Li_2CO_3, LiOH, $LiNO_3$ or LiI with manganese oxides, acetates, or hydroxide powders. The mixtures are then heated in air up to 900 °C [12, 13, 14, 15, 16, 17]. As described in Chapter 3, a preparation method based on the classical firing technique has been developed to obtain a pure, single-phase and high surface area spinel $LiMn_2O_4$, which will be used as precursor to prepare other manganese oxides.

A novel polymorph λ-MnO_2 with a structure characterised by the $[B_2]O_4$ framework of an $[A]_{tet}$ $[B_2]_{oct}$ O_4 spinel, has been synthesised by lithium extraction from $LiMn_2O_4$. Hunter [18] found that treating a sample of $LiMn_2O_4$ with an acid solution at pH about 2 results in the formation of a new form of manganese dioxide (λ-MnO_2). The new phase

has the same spinel structure but with lithium having been extracted from the tetrahedral positions leaving the framework $[B_2]O_4$ intact. The structures of $LiMn_2O_4$ and λ-MnO_2 have been determined by Rietveld analysis of powder neutron diffraction data. $LiMn_2O_4$ is found to have a cubic unit cell with space group Fd3m and a = 8.2468 Å, while λ-MnO_2 has the same unit cell but with a = 8.0639 Å [19]. The interstitial spaces of λ-MnO_2 consist of a three-dimensional network of face-sharing tetrahedra and octahedra, as can be seen in Figure 4.1.

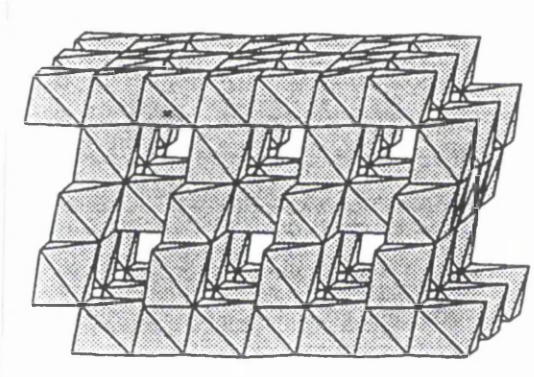

Figure 4.1 The $[B_2]$ O_4 spinel framework.

The spinel λ-MnO_2 has been given a great deal of attention as a new electrode material for secondary lithium batteries. On the other hand, λ-MnO_2 exhibits strong adsorption behaviour towards lithium ions in aqueous solution [20, 21, 22]. The uniform character of λ-MnO_2 makes it a suitable model for "ion-sieve" compounds. It shows a remarkably high selectivity for lithium ions in a range about pH 2.5 [23, 24, 25]. Voltammetric

measurements of electrodes constructed using λ-MnO_2 showed them to have good sensitivity towards small concentrations of Li^+ in solutions [26], a property that can be further investigated and used in an electrochemical lithium ion sensor. Electrodes containing λ-MnO_2 were also successfully used in the potentiometric determination of acids and bases [27].

In this work, the spinel λ-MnO_2 is prepared by the topotactic extraction of lithium from the previously prepared $LiMn_2O_4$. The spinel λ-MnO_2 is then chemically reduced to yield the oxide hydroxide form of manganese. The manganese oxide hydroxide obtained above has not been reported before. This will be given the name λ-MnOOH to indicate the relationship to its precursor oxide. Both manganese oxides, λ-MnO_2 and λ-MnOOH have been characterised using x-ray diffraction, scanning electron microscopy (SEM), FTIR spectroscopy, thermal analysis techniques (TG and DSC), chemical analysis and single point surface area measurements. Surface area measurements of the produced oxides gave 6.3 and 11.2 $m^2 g^{-1}$ for λ-MnO_2 and λ-MnOOH respectively.

4.2 Preparation of λ-MnO_2

4.2.1 Experimental and Results

Spinel-type manganese oxide (λ-MnO_2) is obtained by the topotactic extraction of lithium ions from the spinel-type lithium manganese oxide $LiMn_2O_4$. The extraction can be achieved chemically by treating the parent oxide with dilute acid [18, 28] or an oxidising agent [29]. The extraction process can also be achieved electrochemically

using an electrochemical cell with a $LiMn_2O_4$-containing electrode and a lithium acceptor electrode [30, 31, 32]. A typical electrochemical cell composition is $Li|LiClO_4$ in propylene carbonate (PC)-dimethoxyethane (DME) (1:1)$|LiMn_2O_4$.

4.2.2 Preliminary Study of the Acid Treatment

In order to establish the effect of temperature on the final product of the acid treatment of $LiMn_2O_4$, the reaction was performed at various temperatures.

Temperatures below room temperature were achieved using a cooling coil, in a temperature controlled water bath to within ±0.05 °C. A homogeneous reaction environment was achieved by stirring the solution during the course of the reaction. All reactants were kept at the reaction temperature for at least 24 hours before the reaction commenced. pH measurements were obtained using a pre-calibrated pH meter (Corning Model 7). A two point calibration was performed for the meter for each specific reaction temperature.

An accurately weighed portion of $LiMn_2O_4$ (5 g) was added to 300 ml of double-distilled water. The water and the reaction vessel were kept at the desired reaction temperature. When the pH reading had reached a stable value, usually after 20-30 minutes, a 50 ml portion of 2M sulphuric acid was added to the oxide-water mixture. The reaction mixture was kept stirring at the specified temperature until a constant pH value was obtained, usually after 100 minutes. The reaction was carried out at the temperatures: 1, 5, 10, 15, 20 and 30 °C. After the pH reading had stabilised, the solid

oxide was collected by filtration, washed and dried at 100 °C. The solid oxides were examined by x-ray diffraction and thermal analysis techniques as described in Chapter 2.

All samples gave an identical x-ray diffraction pattern which was confirmed to be that of λ-MnO_2. Hence, the extraction reactions of lithium from $LiMn_2O_4$ proceeded in the temperature range studied, to yield the spinel λ-MnO_2. Thermal analysis results showed that all samples have the same TGA-DSC trace, and all have the characteristic exothermic peak at ~300 °C which corresponds to the conversion of λ-MnO_2 to β-MnO_2. Thermal analysis was performed under nitrogen and the results of these runs are shown in Figure 4.2. Table 4.1 summarises the data obtained from the TGA and DSC traces of the samples prepared at the temperatures above.

Table 4.1 Summary of the results obtained from the TGA and DSC traces for λ-MnO_2 prepared at different temperatures.

Temperature	**1 °C**	**5 °C**	**10 °C**	**15 °C**	**20 °C**	**30 °C**
Heat change (1st DSC peak, mcal/mg)	-48.06	-48.53	-51.83	-52.42	-51.50	-57.00
Heat change (1st TGA peak, mcal/mg)	120.05	121.96	119.35	115.20	116.59	127.90
Heat change (2nd TGA peak, mcal/mg)	74.57	74.75	77.10	73.68	72.09	84.40
Residue at 1000 °C (%)	86.47	86.49	86.49	86.22	86.78	85.76
pH of solution after 100 minutes from the acid addition	1.04	1.06	0.81	0.50	0.38	0.21

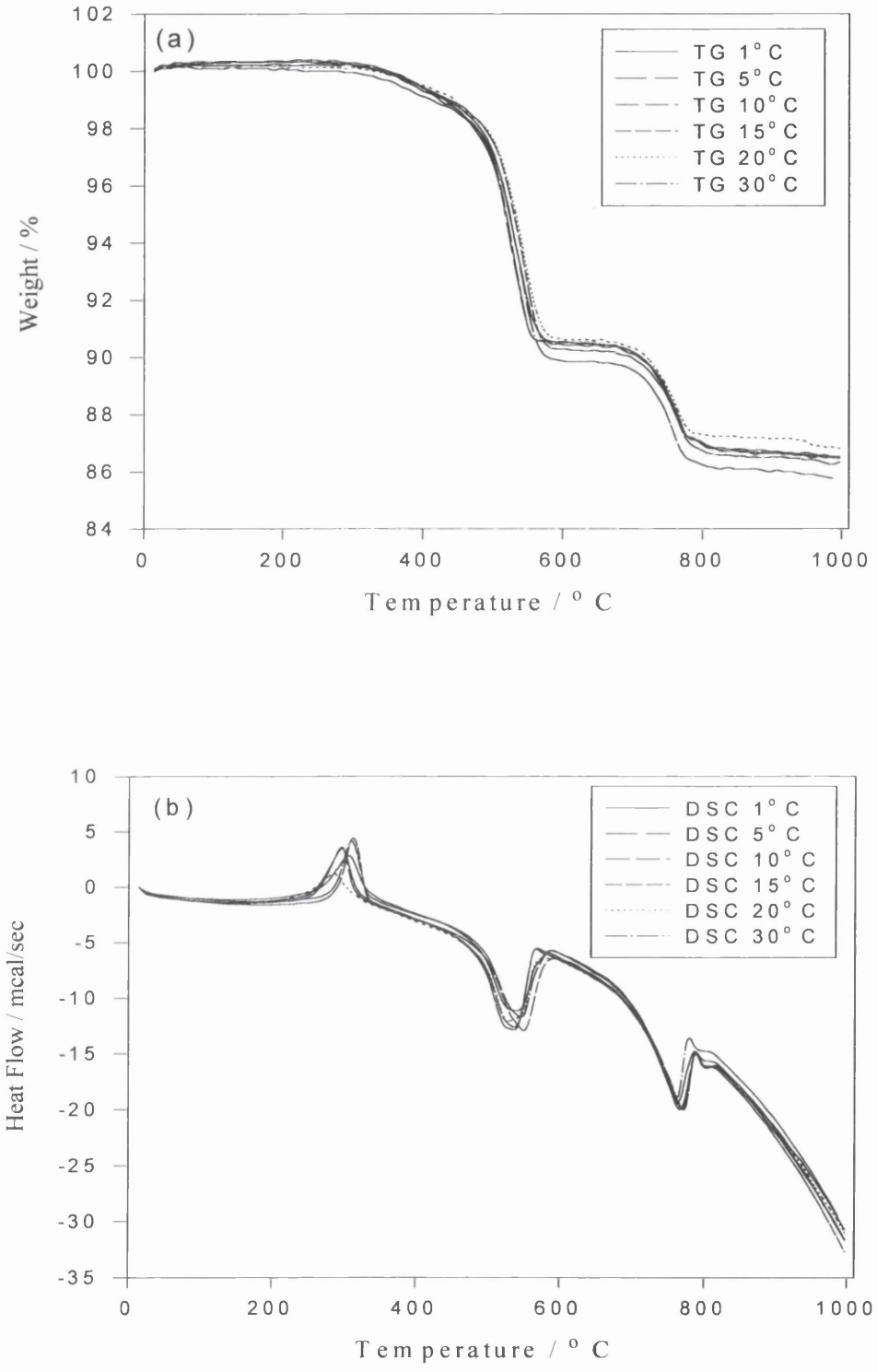

Figure 4.2 (a) TGA and (b) DSC traces for λ-MnO_2 prepared at different temperatures.

From the results above, it was concluded that the preparation of λ-MnO_2 could be achieved at any of the temperatures specified. For technical reasons, the reaction temperature of 20 °C was chosen as the standard temperature for the preparation reaction of λ-MnO_2.

4.2.3 Preparation method

In this work, λ-MnO_2 was prepared by the acid treatment of lithium manganese oxide $LiMn_2O_4$, which had been prepared using the technique described in Chapter 3. The preparation method is summarised below.

15 g of $LiMn_2O_4$ was placed in a beaker containing 400 ml of water, and a solution of dilute acid (2M H_2SO_4, or HCl) was added with stirring, while monitoring the pH changes. The stirring continued for about 45 minutes or until the pH settled at one value. The solution was decanted and the solid washed with five portions of 100 ml distilled water. The solid was then isolated by filtration and dried in air at 100 °C. A 25% weight loss from the original weight was recorded after the extraction procedure. The weight loss is due to the extraction of lithium from the sample and the dissolution of some manganese in the solution.

The samples obtained by the above method were identified by x-ray diffraction, and their composition was determined by chemical analysis as described in Chapter 2. Chemical analysis of λ-MnO_2 revealed that most of the lithium had been extracted from the spinel $LiMn_2O_4$, and x-ray diffraction showed that the new product was a single

phase spinel with a cubic unit cell having a = 8.08 Å, compared to a = 8.24 Å for the parent oxide $LiMn_2O_4$.

4.2.4 X-ray Powder Diffraction

Identification of the product λ-MnO_2 was carried out by x-ray diffraction, which has been described thoroughly in Chapter 2. The x-ray pattern revealed a single phase, corresponding to the results published by Hunter [18] and assigned to the spinel λ-MnO_2. The x-ray diffraction pattern for λ-MnO_2 is shown in Figure 4.3 and the corresponding d-values/Å are listed in Table 4.2 along with the d-values/Å reported by Hunter [18].

Table 4.2 d-values/Å for samples of λ-MnO_2 prepared in this work and by Hunter [18].

hkl	d/Å λ-MnO_2 (this work)	d/Å λ-MnO_2 [18]
111	4.64	4.64
311	2.43	2.42
222	2.32	2.31
400	2.02	2.01
331	1.842	1.84
333	1.543	1.55
440	1.424	1.42
531	1.359	1.35

Figure 4.3 X-ray diffraction pattern for λ-MnO_2 obtained by the acid treatment of $LiMn_2O_4$.

4.2.5 Electron Microscopy

Scanning electron microscopy (SEM) of the λ-MnO_2 samples showed that the shapes of the particles vary considerably. It revealed also a similar morphology to that of $LiMn_2O_4$ with a very slight difference in particle size distribution, 0.5-8 μm for λ-MnO_2 samples compared to 0.5-10 μm for $LiMn_2O_4$, as can be seen in Figure 4.4.

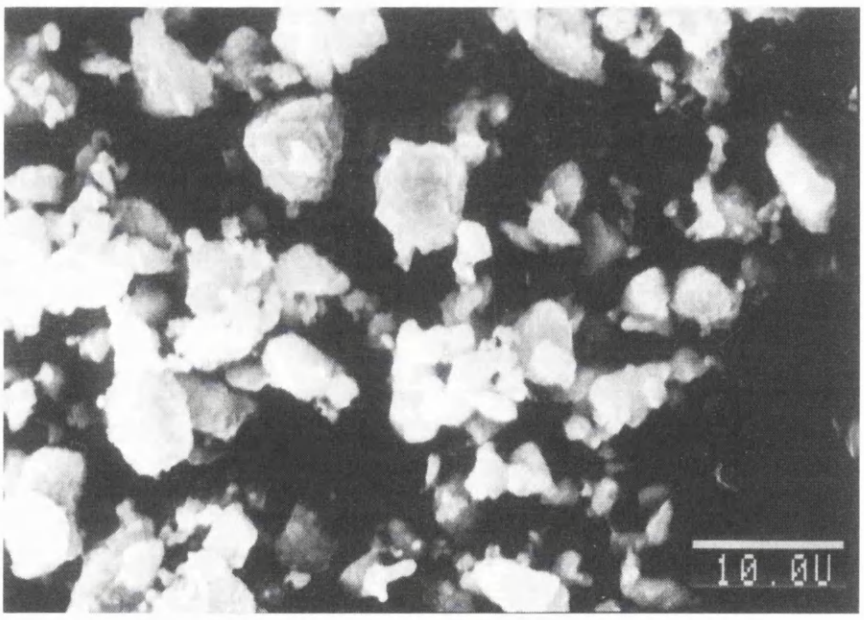

Figure 4.4 Electron microscope photograph of λ-MnO_2 sample, x2000.

4.2.6 Chemical Analysis and Surface Area Measurements

The amounts of lithium, manganese and manganese oxide in λ-MnO_2 samples were determined as described in Chapter 2. The results are summarised in Table 4.3 along with the theoretical values, and the results published by Hunter [18] for comparison.

Surface area measurements of λ-MnO_2 showed that the specific surface area of the sample has a lower value than that of $LiMn_2O_4$ due to the extraction of lithium from $LiMn_2O_4$, which in turn could decrease the pore size distribution. The surface area of λ-MnO_2 as found using the BET single point method (Chapter 2, Section 6) was 6.3 ± 1.7 $m^2 g^{-1}$.

Table 4.3 Chemical composition and specific surface area (SSA) of λ-MnO_2.

λ-MnO_2	% Li	% Mn	% MnO_2	SSA $m^2 g^{-1}$
Theoretical	0	63.2	100	-
Literature [18]	0.4	62.1	93.7	15.0
This work	0.5	63.2	95.4 ±0.7	6.3 ± 1.7

4.2.7 Thermal Analysis

Thermal analysis of the spinel λ-MnO_2 under nitrogen and air showed a characteristic thermogram for λ-MnO_2. DSC analysis of the sample gave quite different results from those for other forms of MnO_2. λ-MnO_2 has a large exothermic peak at 270 °C, which

has been assigned to the transformation of λ-MnO_2 to β-MnO_2, as confirmed by x-ray diffraction. An endothermic peak was found at 540 °C in nitrogen and at 565 °C in air. This peak is assigned to the well-known transformation of β-MnO_2 to bixbyite α-Mn_2O_3. A second endothermic peak was observed at about 700 °C in nitrogen and 900 °C in air. This peak is associated with the well-established transformation of bixbyite α-Mn_2O_3 to hausmannite Mn_3O_4 [33, 34, 35]. The above results indicate that with sufficient heating, the metastable form of manganese oxide λ-MnO_2 reverts to the more stable β-MnO_2 form. Figure 4.5 shows TG and DSC traces for λ-MnO_2 in nitrogen and air.

The exact composition of λ-MnO_2 can be estimated using the information provided by the thermal decomposition trace of λ-MnO_2 in nitrogen. The thermal decomposition of λ-MnO_2 in air has not been used since it involves oxygen uptake during the heating process around 700 °C [33]. The calculation of the available oxygen was based on the sample weight at 1000 °C. The reasons behind this selection are: the product of the decomposition of MnO_2 at 1000 °C is hausmannite Mn_3O_4, regardless of the crystalline structure and the previous history of MnO_2 [34]; 1000 °C is easily achieved using the thermal analyser.

X-ray diffraction analysis of the heated λ-MnO_2 (1000 °C) has confirmed the transformation of manganese dioxide to hausmannite Mn_3O_4.

Let us consider the pure MnO_2 sample. If the stoichiometric composition at 1000 °C was exactly $MnO_{1.333}$ (86.01%), then the weight changes should be 3.5% and 10.49%

according to $MnO_{1.333} \rightarrow MnO_{1.500}$ and $MnO_{1.500} \rightarrow MnO_{2.000}$ respectively. In practice, the percentage of $MnO_{1.333}$ resulting from heating λ-MnO_2 in nitrogen is 87.88%, indicating a deviation from the ideal state. The first weight gain of 3.78% corresponds to the change $MnO_{1.333} \rightarrow MnO_{1.538}$, and a second weight gain of 8.34% corresponds to the change $MnO_{1.538} \rightarrow MnO_{1.99}$. The small deficiency of oxygen in the spinel form of manganese dioxide, λ-MnO_2, is within the experimental error and could be attributed to the presence of lithium in the crystal structure despite the acid treatment.

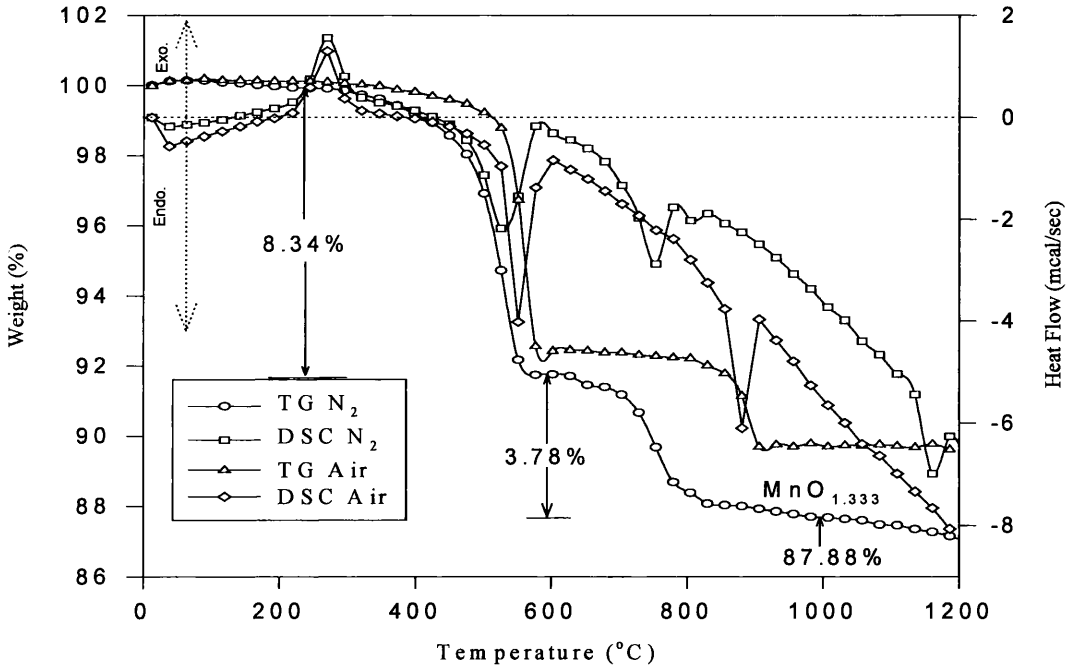

Figure 4.5 TG and DSC traces of λ-MnO_2 in nitrogen and air.

Unlike the other forms of manganese dioxide [36], the spinel λ-MnO_2 has no detectable adsorbed and structural water content, in spite of using aqueous solutions and a relatively low drying temperature (90 °C) in the preparation process. The first derivative of the TG trace for λ-MnO_2 between 25 and 700 °C in nitrogen produced a straight line until the first weight loss started to take place at around 400 °C, as can be seen in Figure 4.6. The thermal decomposition of λ-MnO_2 in nitrogen could be summarised by Equation 4.1.

$$\lambda - MnO_{1.99} \xrightarrow{300\,^{\circ}C} \beta - MnO_{1.99} \xrightarrow{550\,^{\circ}C} MnO_{1.538} \xrightarrow{800\,^{\circ}C} MnO_{1.333} \quad 4.1$$

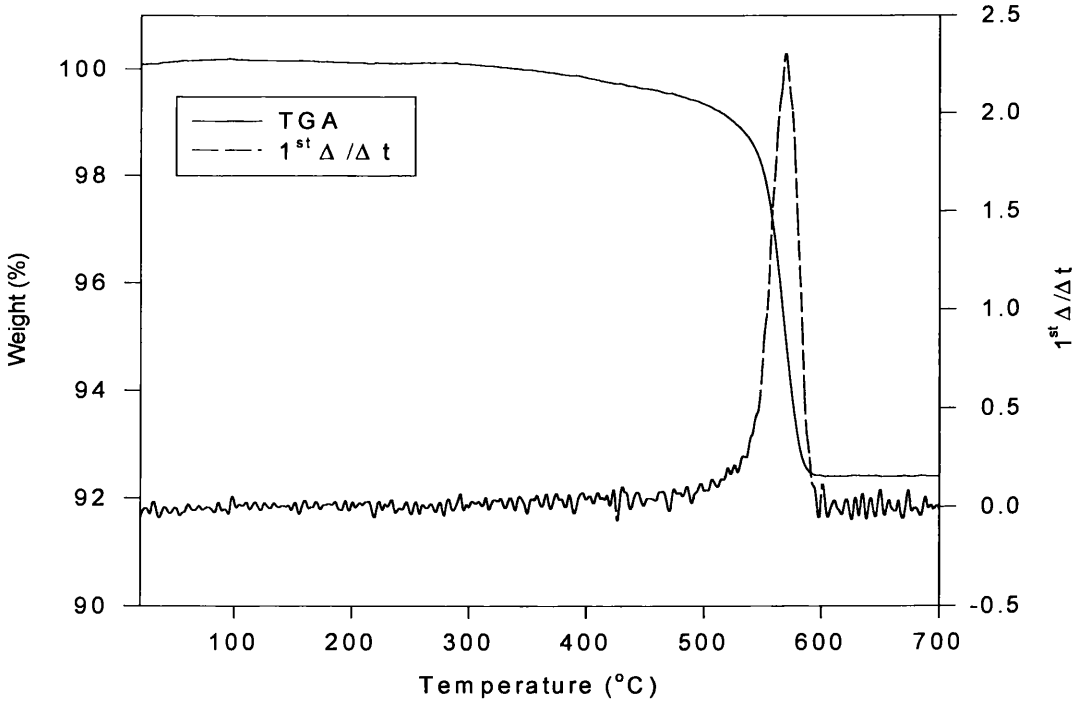

Figure 4.6 The TGA trace and its derivative for λ-MnO_2 heated from 25 to 700 °C in nitrogen.

4.2.8 FTIR Spectroscopy

A sample of λ-MnO_2 was examined by FTIR spectroscopy and gave the spectrum shown in Figure 4.7. The removal of lithium from $LiMn_2O_4$ to form λ-MnO_2 results in major changes in the FTIR spectrum, regardless of the fact that λ-MnO_2 has retained the cubic symmetry of the original oxide. The spectrum is dominated by a broad band of overlapping peaks centred at 520 cm^{-1} with two distinct shoulders at ca. 500 and 530 cm^{-1}, along with a smaller sharper peak at 610 cm^{-1}. Richardson *et al.* [37] explain the complexity in the λ-MnO_2 FTIR spectrum by the change in the Mn^{3+}: Mn^{4+} ratio.

The local symmetry is lowered by the removal of lithium from the tetrahedral site and the balance in electrostatic energy requires that a manganese ion near the lithium vacancy be oxidised to Mn^{4+}.

The bands located at 1630 and 3450 cm^{-1}, which could be assigned to the O-H bending and stretching vibrations, have become broader and less intense in comparison with the same band for the mother oxide $LiMn_2O_4$. The broad and low intensity bands suggest that little water is present in the sample and that it does not occupy well-defined crystallographic sites.

The removal of lithium from $LiMn_2O_4$ has introduced a new band at 920 cm^{-1}, which could be assigned to the lattice coupling vibration of the H^+-form spinel [38]. This band indicated the possibility of a Li^+/H^+ exchange reaction, and may be used to assess the extent of exchange during the lithium extraction reaction.

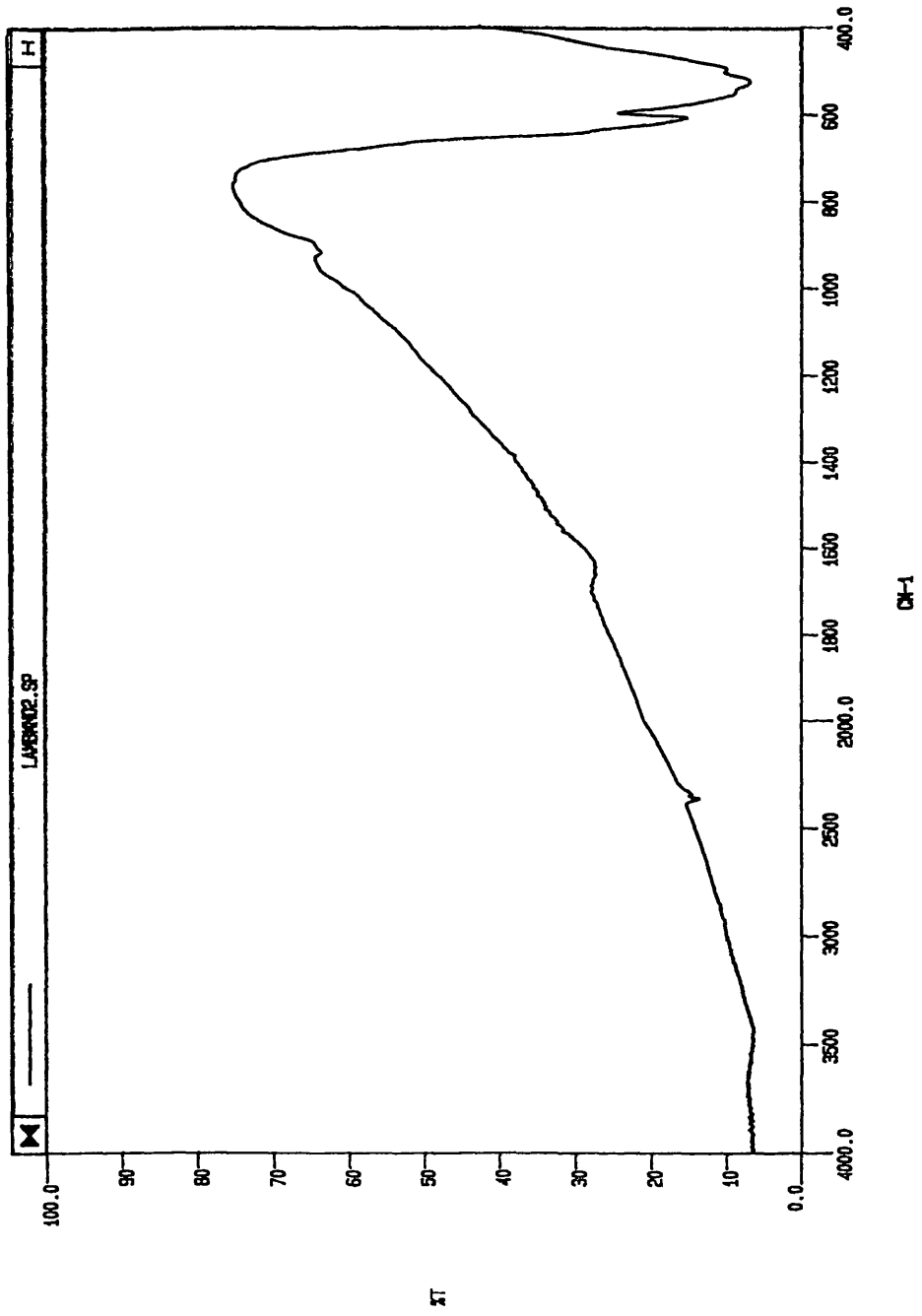

Figure 4.7 FTIR spectrum of λ-MnO_2.

4.2.9 Discussion

The lithium ion extraction-insertion reaction in $LiMn_2O_4$ has been interpreted using several different mechanisms. A disproportionation mechanism has been introduced by Hunter [18], which can be represented by the equation below.

$$2LiMn_2O_4 + 4H^+ \rightarrow 3\lambda - MnO_2 + 2Li^+ + Mn^{2+} + 2H_2O \qquad 4.2$$

An ion exchange mechanism has been also proposed to explain the topotactic extraction of lithium ions [39, 40], and could be represented as follows.

$$LiMn_2O_4 + H^+ \rightarrow HMn_2O_4 + Li^+ \qquad 4.3$$

From Equation 4.3, we can see that the extraction of lithium into solution consumes an equivalent amount of H^+ ions. Therefore, by measuring the change in H^+ concentration in the solution, we could follow the extraction of lithium from $LiMn_2O_4$ as the reaction progresses. During a preliminary study, an attempt was made to follow the pH changes but it proved to be impossible especially during the early steps of the reaction due to the speed of the reaction.

Feng *et. al.* [41] proposed that both redox-type and ion-exchange-type reactions could take place at the same time, and described the origin of both reaction types from a chemical and structural point of view. It is the fact that lithium manganese oxides exhibits both easy conversion between Mn^{3+} and Mn^{4+} because of the simple movement of electrons, and also easy migration of lithium ions in the oxygen framework, that

results in the existence of various kinds of spinels with different oxidation states of manganese and with different Li/Mn mole ratios. Based on that model, spinel lithium manganese oxides with trivalent manganese have redox-type sites while oxides with tetravalent manganese have ion-exchange-type sites for Li^+/H^+ exchange. So the extraction of lithium ions from redox-type sites gives a proton-free spinel manganese oxide (□)Mn_2O_4, and the extraction of lithium from ion-exchange-type sites gives a protonated spinel manganese oxide, HMn_2O_4. The contents and proportions of these sites can be predicted using the Li/Mn ratio and the mean oxidation number of manganese ($\overline{Z}_{Mn}$) values of a lithium manganese oxide spinel without direct study of the extraction / insertion reactions. The model calculations suggest that $LiMn_2O_4$ contains only redox-type sites and that $Li_{1.33}Mn_{1.67}O_4$ contains only ion-exchange-type sites, as described in Equations 4.2 and 4.3 respectively. [41].

Kanzakai *et al.* [20] proposed a unique mechanism based on their NMR ^7Li results. They suggested that lithium exists in $LiMn_2O_4$ in an atomic state. Hence, the redox reaction between $LiMn_2O_4$ and λ-MnO_2 is not Mn^{4+} to Mn^{3+} but Li^0 to Li^+. So the extraction of lithium would follow the equations below:

$$2Li^0Mn_2O_4 + 4H^+ \rightarrow 2Li^+ + Mn^{2+} + 3MnO_2 + 2H_2O \qquad 4.4$$

and the redox reactions are:

$$2Li^0 - 2e^- \rightarrow 2Li^+ \qquad 4.5$$

$$Mn^{4+} + 2e^- \rightarrow Mn^{2+} \qquad 4.6$$

The reduction reaction could include O_2 reduction as a side reaction:

$$\tfrac{1}{2}O_2 + 2H^+ + 2e^- \rightarrow H_2O \qquad 4.7$$

The experimental weight loss after the extraction of about 25% is less that the theoretical weight loss according to reaction 4.4 of 33%. The 8% difference in weight could be attributed largely to the crude drying method followed. The method can be simply described by placing the sample with the filtration crucible inside a drying cabinet set to about 100 °C. Some of the difference in weight loss found above could also be attributed the un-extracted lithium ions and to the large 3-D tunnels formed by the extraction in which water could be trapped.

In the experiments involving insertion of lithium ion into λ-MnO_2 described in Chapter 6, the introduction of lithium ion into the spinel structure was attempted on the assumption that the reaction is based on the ion exchange mechanism. Results showed that no lithium had been inserted when a sample of λ-MnO_2 was exposed to a mixture of LiOH and LiCl at various temperatures. The product was confirmed by x-ray diffraction and thermal analysis to be λ-MnO_2, i.e. no structural change had taken place as a result of a lithium exchange reaction with H^+ in the solid. A neutron diffraction study of λ-MnO_2 confirmed that there is no evidence of such lithium / hydrogen ion exchange [42].

By including a manganese source, e.g. $MnCl_2$ in the insertion reaction, it was found that lithium was easily inserted into λ-MnO_2. A subsequent examination of the product by x-ray diffraction confirmed that the product of the insertion reaction was $LiMn_2O_4$. See Chapter 6, Section 6.2.

Although the main reaction could follow the disproportionation route, the proton exchange reaction with lithium cannot be ruled out completely. The new band (920 cm^{-1}) that appeared in the FTIR spectrum of λ-MnO_2 is an indication of the presence of H^+ in the lattice. The band is a result of the coupling vibration of the H^+-form spinel [43]. Thermal examination of λ-MnO_2 (see Figures 4.5 and 4.6) ruled out residual water as the cause behind the appearance of this band. The extent of this band in the FTIR spectrum does not indicate a large-scale Li^+/H^+ exchange reaction but suggests the existence of limited surface exchange sites limited to extent that no fundamental structural changes were observed in λ-MnO_2 during the insertion reaction performed without the presence of manganese. See Chapter 6, Section 6.4.

From the above it can be concluded that the extraction reaction of lithium ions from spinel $LiMn_2O_4$ follows a disproportionation mechanism as in Equation 4.2 with a very small contribution from an ion-exchange surface reaction that proceeds according to Equation 4.3. The extraction reaction was found to be fully reversible providing the correct conditions were met.

4.3 Preparation of λ-MnOOH

Manganese oxides have been reduced electrochemically and chemically, and the result of the reduction is MnOOH or $MnO_{1.5}$. It is well established that the reduction of manganese dioxide proceeds via proton insertion into the solid phase as first proposed by Coleman [44], Brent [45], Vosburgh [46], and Feitknecht [47]. The reduction reaction could be represented by Equation 4.4.

$$MnO_2 + H^+ + e^- \rightarrow MnO_{1.5} \ . \ 0.5\,H_2O \qquad 4.4$$

Many researchers before have investigated γ-MnO_2, since it is the most widely used material for batteries. Manganese oxide has been reduced electrochemically by Maskell *et al.* [48] using a modified Leclanché cell. The commercial γ-MnO_2 was mixed with carbon black, graphite, NH_4Cl, ZnO, $ZnCl_2$ and water to construct the cell. On the other hand, the chemical reduction of manganese oxide can be classified according to the reducing agent used in the reaction.

A) The Hydrazine Method [34, 49, 50 ,51]

This method involves mixing a sample of manganese oxide (γ-MnO_2) with the desired amount of hydrazine hydrate. The mixture is kept under a nitrogen atmosphere at room temperature without stirring. The amount of hydrazine hydrate corresponds to the degree of reduction required for the manganese oxide [49, 51]. Maskell *et al.* [48] modified the previous method by adding the hydrazine hydrate dropwise over 24 hours at room

temperature to a stirred suspension of manganese oxide. The reduction of manganese oxide is accompanied by the formation of nitrogen gas according to Equation 4.5.

$$NH_2.NH_2 + 4\,MnO_2 \rightarrow N_2(g) + 4\,MnOOH \qquad 4.5$$

B) The Cinnamic Alcohol Method [36,48]

The reduction of manganese oxide (γ-MnO_2) by cinnamic alcohol can be globally represented by equation 4.6.

$$Ar - CH = CH - CH_2OH + 2\,MnO_2 \rightarrow 2\,MnOOH + Ar - CH = CH - CHO \qquad 4.6$$

Cinnamic alcohol and manganese oxide are reacted in a 1:2 molar ratio and 50% excess of cinnamic alcohol is added to the reaction. Gabano *et al.* [36] showed that use of a higher temperature reduced the time required for the reaction to reach completion.

C) The Manganous Chloride Method [48]

Manganous chloride in an ammoniacal solution of ammonium chloride reacts with manganese oxide at 25 °C. The reduction proceeds according to Equation 4.7

$$MnO_2 + Mn^{2+} + 2H_2O \rightarrow 2\,MnOOH + 2H^+ \qquad 4.7$$

4.3.1 Preparation method

For the reduction of λ-MnO_2, the cinnamic alcohol method was employed. The procedure adopted was as follows. 11.58 g of cinnamic alcohol was dissolved in xylene, and then added to 10 g of manganese dioxide (λ-MnO_2). The reaction was carried out at 80 °C for four hours. An ambient atmosphere of CO_2 was maintained during the course of the reaction. The precipitate was then collected by filtration, washed with xylene and dried at 60 °C.

The success of the reaction was confirmed by examining the reductant by means of FTIR spectroscopy. This showed that the main absorption bands of the alcohol functional group (-OH) at 3580 and 3400 cm^{-1} had decreased in intensity. Since the reduction of MnO_2 is accompanied by the oxidation of the alcohol to the aldehyde, a new and strong absorption band at 1700 cm^{-1} had appeared, which corresponds to the carbonyl group (-CHO). The FTIR spectra of cinnamic alcohol before and after the reaction are shown in Figure 4.8.

The resultant fine powder was examined by x-ray diffraction, electron microscopy, FTIR spectroscopy and thermal analysis.

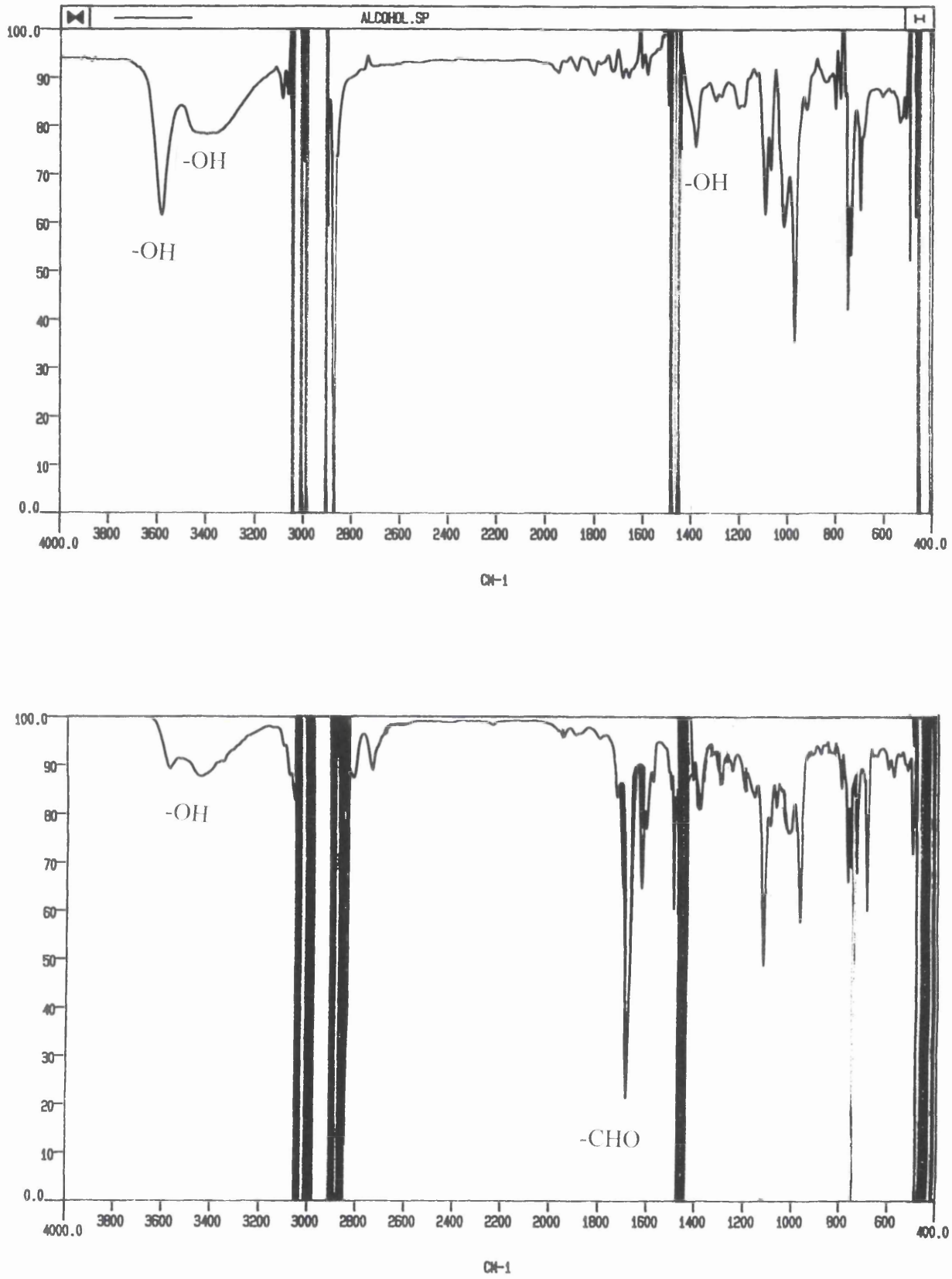

Figure 4.8 FTIR spectra of cinnamic alcohol (a) before and (b) after the reduction of λ-MnO_2.

4.3.2 X-ray Powder Diffraction

The x-ray diffraction pattern obtained from the product of the reduction revealed the presence of a single cubic phase. This has a spinel structure and could be designated as λ-MnOOH, which has not been discussed before. The diffraction pattern is shown in Figure 4.9.

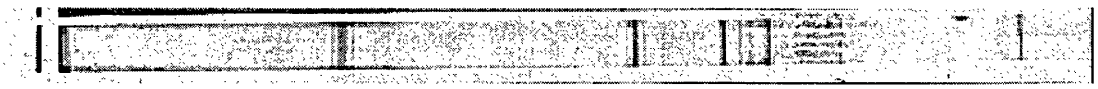

Figure 4.9 X-ray diffraction pattern of λ-MnOOH.

In Table 4.4, d-values/Å of the pattern above and those for the original oxide λ-MnO_2, before the reduction to λ-MnOOH, are presented. The reduction of λ-MnO_2 (a = 8.08 Å) was accompanied by a slight increase in the unit cell parameter (a = 8.096 Å). The increase is believed to be caused by Jahn-Teller distortion introduced by the reduction of the manganese from Mn^{4+} (r = 0.53 Å) to Mn^{3+} (r = 0.645 Å) analogous to that found during the chemical reduction of γ-MnO_2 [48]. The introduction of the relatively larger manganese ion (Mn^{3+}) into the unit cell did not, however, have a large impact on the unit cell dimensions. This could be explained by the presence of the large 3-D channels present in the spinel structure. The expansion of the tetrahedra would take place internally towards the empty 3-D channels leaving the unit cell with only a small change in dimensions. The decrease in the size of the 3-D channels would decrease the freedom of the hydroxyl group, which would explain the poor definition found in the sample's FTIR spectrum (Figure 4.8).

Table 4.4 X-ray diffraction data (d/Å) for λ-MnO_2 and λ-MnOOH.

hkl	λ-MnO_2	λ-MnOOH
111	4.64	4.65
311	2.43	2.435
222	2.31	2.33
400	2.02	2.024
331	1.842	1.847
333/511	1.543	1.544
440	1.424	1.426
531	1.359	1.365

4.3.3 Electron Microscopy

The sample produced by the reduction of λ-MnO_2 was observed under the electron microscope and recorded on the micrograph shown in Figure 4.10. The sample has a similar morphology to those of λ-MnO_2 and $LiMn_2O_4$.

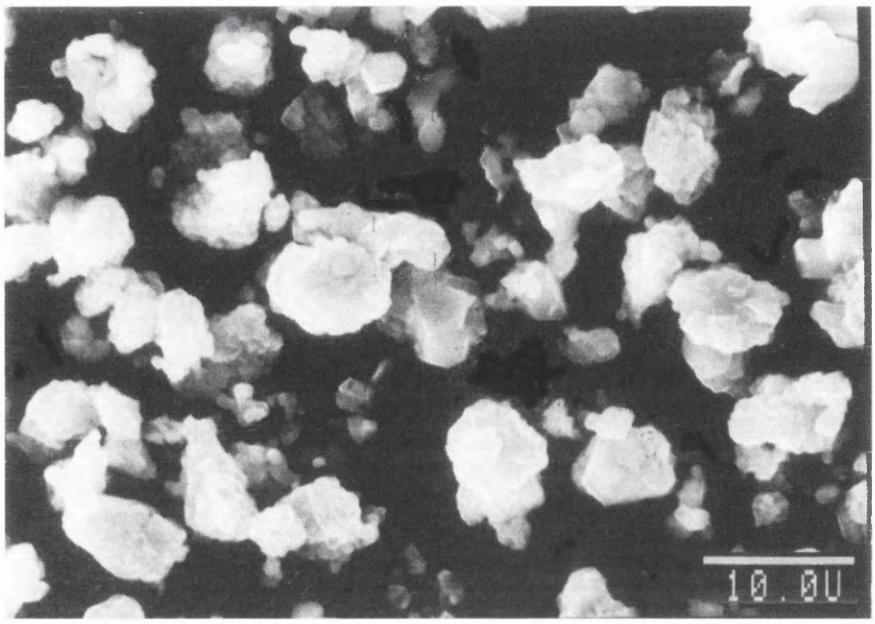

Figure 4.10 Electron microscope photograph of λ-MnOOH, x2000.

4.3.4 Chemical Analysis and Surface Area Measurements

The amounts of lithium and manganese in λ-MnOOH were determined as described in Chapter 2. The results are presented in Table 4.5.

Surface area measurements of the chemically reduced λ-MnO_2 showed that the specific surface area of the sample had increased to nearly double the specific surface area of λ-MnO_2. The specific surface area of the chemically reduced λ-MnO_2, measured as described in Chapter 2, is 11.2 ± 2.0 m^2 g^{-1}.

Table 4.5 Chemical composition and specific surface area (SSA) of λ-MnOOH.

λ-MnOOH	% Li	% Mn	SSA $m^2 g^{-1}$
Theoretical	0	62.5	-
This Work	0.5	62.1	11.2 ± 2.0

4.3.5 Thermal Analysis

A sample of the reduced λ-MnO_2 was analysed thermally as described in Chapter 2. The sample was heated gradually (10 °C / min) to 1200 °C in nitrogen or air and the results are shown in Figure 4.11.

Both thermograms exhibit three major weight losses. In nitrogen, the first weight change (7.48%) is attributed to the dehydration of the sample at a temperature up to 400 °C. The change includes the loss of both adsorbed and combined water, leaving an oxide with nominal formula MnO_x. The dehydration reaction is followed by a rapid loss of 3.5% of the oxygen content of the sample between 400 and 650 °C. The third weight change of 2.4% is recorded between 650 and 1000 °C, which corresponds to the transformation to the well-known oxide of manganese, Mn_3O_4, as confirmed by x-ray diffraction.

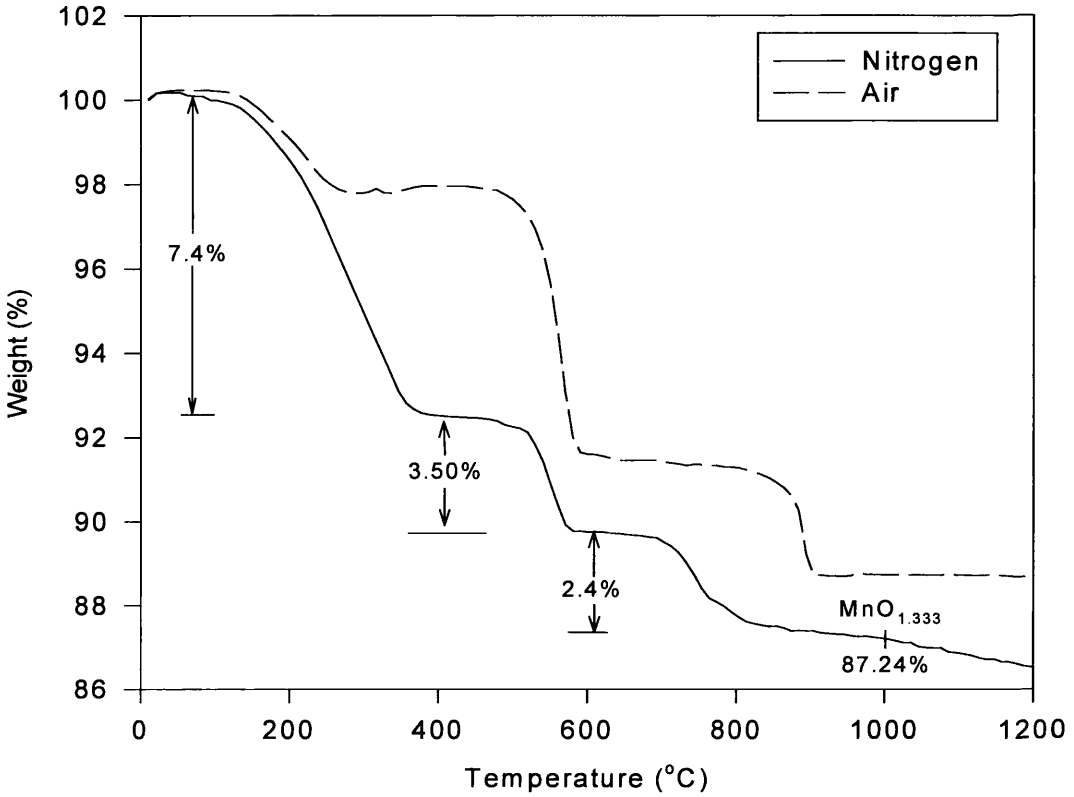

Figure 4.11 TGA traces of λ-MnOOH in nitrogen and air.

Since the product of the thermal decomposition of λ-MnOOH at 1000 °C was confirmed to be hausmannite Mn_3O_4 ($MnO_{1.333}$), the stoichiometry of the starting material can be estimated using the same route followed for λ-MnO_2. The third weight loss leading to $MnO_{1.333}$ was estimated to be about 2.4% of the total weight, which corresponds to 0.131 mole of oxygen, indicating that the precursor oxide should have the stoichiometric composition of $MnO_{1.464}$. The second change of 3.5% is due to the loss of 0.191 moles of oxygen suggesting an intermediate manganese oxide with the stoichiometry $MnO_{1.655}$ has been formed at about 400 °C. The first weight loss of about 7.4% corresponds to the

loss of 0.359 moles of adsorbed and structural water. The final stoichiometric composition of the manganese oxide hydroxide could be represented by the formula $MnO_{1.655}$. $0.359H_2O$. Manganese oxide hydroxides could be equally well represented by the expressions:

$MnO_2 .H_{(4-2n)} .mH_2O$ or $MnO_n .(2-n+m)H_2O$

where n is the "degree of oxidation" (2n = average valency) and (2-n+m) corresponds to the total structural water [36, 52, 53, 54].

For the manganese oxide hydroxide prepared above, $MnO_{1.655}$ $.0.359H_2O$, the values n = 1.655 and 2-n+m = 0.359 give m = 0.014 which represents the neutral water molecules present in the structure. The value of 4-2n equals 0.69 moles of OH^-, that is 0.345 moles of H_2O per mole of manganese leaving the 0.014 moles of additional water which could be surface or interstitially adsorbed water [55]. According to the model above, λ-MnOOH could be represented as $[MnO_{1.655} \cdot 0.345\ H_2O] \cdot 0.014\ H_2O$.

4.3.6 FTIR Spectroscopy

The FTIR spectrum of λ-MnOOH was taken as described in Chapter 2, and is shown in Figure 4.12. The reduction of λ-MnO_2 to λ-MnOOH has introduced a complex and dramatic change in the FTIR spectrum, despite the fact that λ-MnOOH has retained the cubic symmetry of λ-MnO_2. The spectrum is generally poor and dominated by broad and ill-defined bands between 400-600 cm^{-1} and 1200-4000 cm^{-1}, along with small peaks at 610 and 920 cm^{-1} as a result of the reduction of most Mn^{4+} to Mn^{3+}.

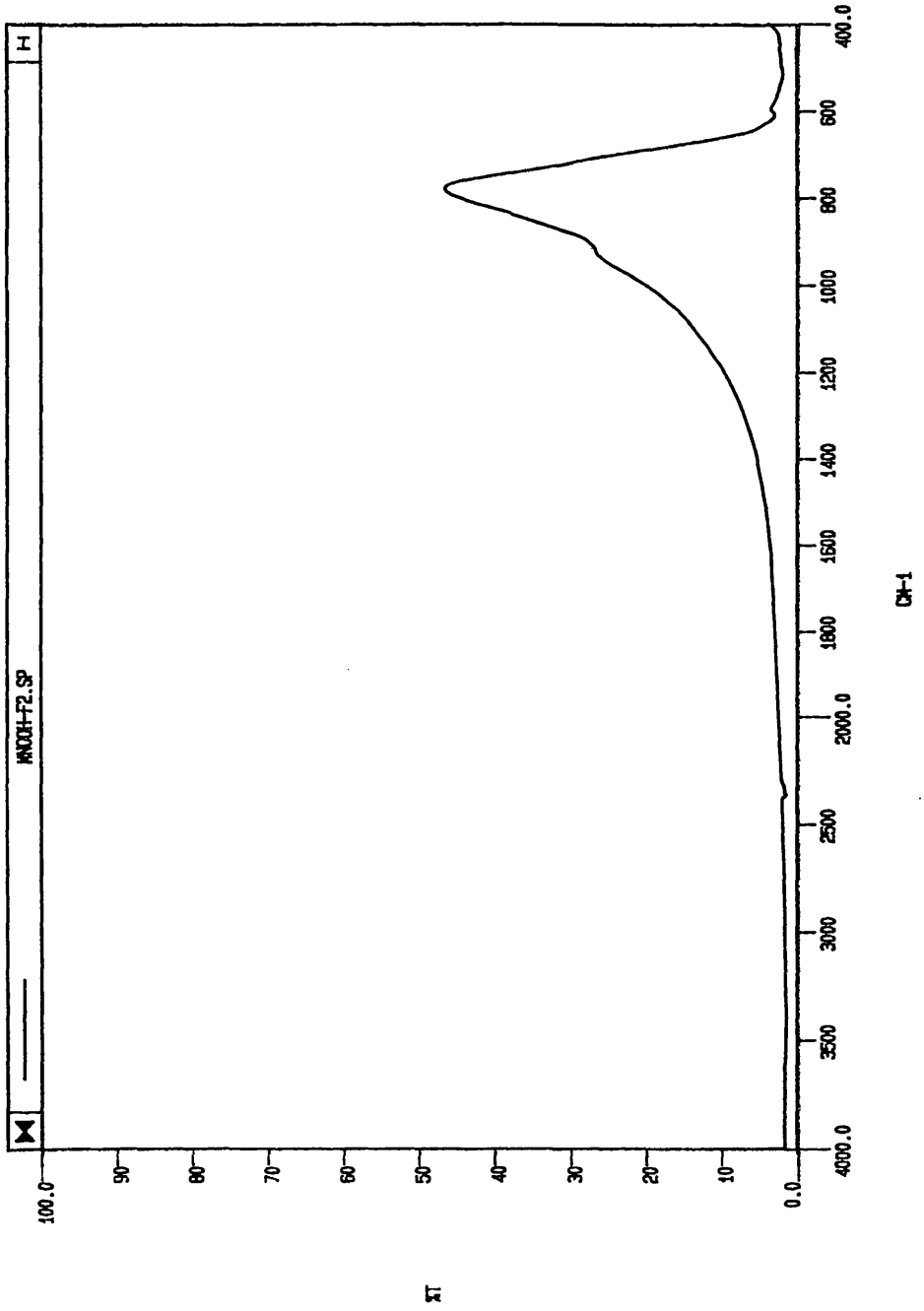

Figure 4.12 FTIR spectrum of λ-MnOOH.

4.4 Conclusion

The novel form of manganese dioxide λ-MnO_2 has been prepared by the topotactic extraction of lithium from lithium manganese oxide $LiMn_2O_4$ as prepared as described in Chapter 3. The identity of the extraction product was confirmed using x-ray powder diffraction, and the stoichiometry of the oxide has been determined using thermal analysis and found to be $MnO_{1.99}$.

The extraction reaction of lithium is thought to follow a disproportionation mechanism where lithium ions and di-valent surface manganese ions are released into solution. The reaction above could be accompanied by a very small amount of surface Li^+/H^+ ion exchange reaction.

Manganese dioxide λ-MnO_2 has been chemically reduced using cinnamic alcohol. The product of the reduction reaction was a single-phase cubic spinel MnOOH, as confirmed by x-ray diffraction and FTIR spectroscopy. The new phase manganese oxide hydroxide MnOOH was given the name λ-MnOOH to distinguish it from the other manganese oxide hydroxides. The composition of the manganese oxide hydroxide was determined using thermal analysis and found to be $[MnO_{1.655}\cdot 0.345\ H_2O]\cdot 0.014\ H_2O$.

The chemical compositions and the specific surface areas (SSA) of λ-MnO_2 and λ-MnOOH are summarised in Table 4.6.

Table 4.6 Chemical compositions and specific surface areas (SSA) of λ-MnO_2 and λ-MnOOH.

	% Li	% Mn	% MnO_2	SSA $m^2 g^{-1}$	Composition
λ-MnO_2					
Literature [18]	0.4	62.1	93.72	15	
This work	0.5	63.2	95.4	6.3 ±1.7	$MnO_{1.99}$
λ-MnOOH					
Theoretical	0	62.5	-	-	
This work	0.5	62.1	-	11.2 ±2.0	$[MnO_{1.655}{\cdot}0.345H_2O]{\cdot}0.014\ H_2O$

References

1 K.M. Parida, S.B. Kanungo, and B.R. Sant, *Electrochimica Acta*, **26**, 435 (1981).

2 B. Scrosati, *Nature*, **373**, 557 (1995).

3 S. Megahed and B. Scrosati, *Interface*, **4**, 34 (1995).

4 M.S. Whittingham, *Science,* **192**, 1126 (1976).

5 J.R. Dahn, T. Zheng, Y. Liu, and J.S. Xue, *Science,* **270**, 590 (1995).

6 M.B. Armand, in *Materials for Advanced Batteries*, D.W. Murphy, J. Broadhead, B.C.H. Steel, Eds., Plenum, New York (1980) p.145.

7 D.W. Murphy and P.A. Christian, *Science,* **205**, 651 (1979).

8 M. Winter, J.O. Besenhard, M.E. Spahr, and P. Novak, *Adv. Materials,* **10**, 725 (1998).

9 R. Koksbang, J. Barker, H. Shi, and M.Y. Saidi, *Solid State Ionics,* **84**, 1 (1996).

10 T. Nagaura and T. Tozawa, *Prog. Batteries Solar Cells*, **9**, 209 (1990).

11 T. Ohzuku and A. Ueda, *Solid State Ionics,* **69**, 201 (1994).

12 D. Wickham and W. Croft, *J. Phys. Chem. Solids*, **7**, 351 (1958).

13 V.I. Ezikyan, G.P. Ereiskaya, U.V. Ivanov, and A.M. Kolomoets, *Langmuir*, **25**, 795 (1989).

14 A. Momchilov, V. Manev, A. Nassalevska, and A. Kozawa, *J. Power Sources*, **41**, 305 (1993).

15 A. Momchilov, V. Manev, A. Nassalevska, and A. Kozawa, *J. Power Sources,* **43/44**, 551 (1993).

16 J.M. Tarascon, W.R. Mckinnon, F. Coowar, T.N. Bowmer, G. Amatucci, and D. Guyomard, *J. Electrochem. Soc.,* **141**, 1421 (1994).

17 V. Manev, A. Momchilov, A. Nassalevska, and A. Sato, *J. Power Sources,* **54**, 323 (1995).

18 J. Hunter, *J. Solid State Chem.*, **39**, 142 (1981).

19 C. Fong, B.J. Kennedy, and M.M. Elcombe, *Zeit. für Kristall.*, **202**, 941 (1994).

20 Y. Kanazaki, A. Taniguchi, and M. Abe, *J. Electrochem. Soc.*, **138**, 333 (1991).

21 B. Ammundsen, P.B. Aitchison, G.R. Burns, D.J. Jones, and J. Roziere, *Solid State Ionics,* **97**, 269 (1997).

22 H. Koyanaka, O. Matsubaya, Y. Koyanaka, and N. Hatta, *J. Electroanal. Chem.*, **559**, 77 (2003).

23 K. Ooi, Y. Miyai, S. Katoh, H. Maeda, and M. Abe, *Bull. Chem. Soc. Jpn.*, **61**, 407 (1988).

24 K. Ooi, Y. Miyai, S. Katoh, H. Maeda, and M. Abe, *Langmuir* **5**, 150 (1989).

25 K. Ooi, Y. Miyai, and J. Sakakihara, *Langmuir*, **7**, 1167 (1991).

26 M.F.S. Teixeira, F.C. Moraes, O. Fatibello-Filho, and N. Bocchi, *Anal. Chim. Acta,* **443**, 249 (2001).

27 M.F. de S. Teixeira, F.C. Moraes, O. Fatibello-Filho, L.C. Ferracin, R.C. Rocha-Filho, and N. Bocchi, *Sensors and Actuators B: Chemical*, **56**, 169 (1999).

28 Y. Onodera, T. Iwasaki, H. Hayashi, and K. Torii, *Chem. Lett.,* 1801 (1990).

29 A. Mosbah, A. Verbaern, and M. Tounoux, *Mater. Res. Bull.*, **18**, 1375 (1983).

30 M.M. Thackeray, P.J. Johnson, L.A. de Picciotto, P.G. Bruce, and J.B. Goodenough, *Mater. Res. Bull.*, **19**, 179 (1984).

31 L. Chen, X. Huang, E. Kelder, and J. Schoonman, *Solid State Ionics*, **76**, 91 (1995).

32 K. Kanamura, H. Naito, T. Yao, and Z. Takehara, *J. Mater. Chem.,* **6**, 33 (1996).

33 F. Petit, M. Lenglet, and J. Arsene, *Mat. Res. Bull.,* **28**, 1093 (1993).

34 T. Ohzuku, I Tari, and T. Hirai, *Electrochimica Acta*, **27**, 1049 (1982).

35 D. Dollimore and K.H. Tonge, *Thermal Analysis*, **2**, 91 (1971).

36 J.P. Gabano, B. Marignat, E. Fialdes, B. Emery, and J.F. Laurent, *Z. Phys. Chem.*, **46**, 359 (1965).

37 T.J. Richardson, S.J. Wen, K.A. Striebel, P.N. Ross, Jr., and E.J. Cairns, *Mater. Res. Bull.*,**32**, 609 (1997).

38 Q. Feng, Y. Miyai, H. Kano, and K. Ooi, *Langmuir*, **8**, 1861 (1992)

39 S. Xiang-mu and A. Clearfield, *J. Solid State Chem.,* **64**, 270 (1986).

40 X. Shen and A. Clearfield, *J. Solid State Chem.,* **64**, 270 (1986).

41 Q. Feng, Y. Miyai, H. Kano, and K. Ooi, *Langmuir*, **8**, 1861 (1992).

42 H. Berg and J.O. Thomas, *Solid State Ionics*, **126**, 227 (1999).

43 Q. Feng, Y. Miyai, H. Kano, and K. Ooi, *Langmuir*, **8**, 1861 (1992)

44 J.J. Coleman, *Trans. Electrochem. Soc.,* **90**, 545 (1946).

45 J.P. Brent, *Compt. Rend.*, **231**, 543 (1950).

46 W.C. Vosburgh and D.T. Ferrell, *J. Electrochem. Soc.*, **98**, 334 (1951).

47 W. Feitknecht, H.R. Oswald, and U. Feitknecht-Steinmann, *Helv. Chim. Acta*, **43**, 1947 (1960).

48 W.C. Maskell, J.E.A. Shaw, and F.L. Tye, *Electrochimica Acta,* **26**, 1403 (1981).

49 T. Ohzuku and T. Hairai, in *Manganese dioxide electrode, theory and practice for electrochemical applications*, B. Schumm, Jr, R.L. Middaugh, M.P. Grotheer, and J.C. Hunter, Editors, The Electrochemical Society Proceedings series, Pennington, NJ (1985) p.141.

50 M. Fukuda, in *Manganese dioxide electrode, theory and practice for electrochemical applications*, B. Schumm, Jr, R.L. Middaugh, M.P. Grotheer, and J.C. Hunter, Editors, The Electrochemical Society Proceedings series, Pennington, NJ (1985) p. 180.

51 X. Xia, H. Li, and Z. Chen, *J. Electrochem. Soc.,* **136**, 266 (1989).

52 P. Brouillet, A. Grund, and F. Jolas, *C.R. Acad. Sci. Paris*, **257,** 3166 (1963).

53 G. Coeffier and J. Brenet, *Electrochimica Acta*, **10,** 1013 (1965).

54 L. Balevski, J. Brenet, G. Coeffier, and P. Lancon, *C.R. Acad. Sci. Paris*, **260,** 106 (1965).

55 P. Ruetchi, *J. Electrochem. Soc.,* **131**, 2737 (1984).

Lithium Extraction Reactions with Spinel Manganese Oxides - A kinetic Study

The extraction reaction of lithium from spinel manganese oxides is discussed in this chapter. The diffusion kinetics of the extraction reaction were studied by measuring the amounts of lithium diffused into solution and the residual lithium in the solid after the extraction. The results of the investigation are presented in this Chapter.

5.1 Introduction and Theory

Lithium can be extracted chemically and electrochemically from $LiMn_2O_4$. The chemical extraction method usually consists of exposing the spinel oxide $LiMn_2O_4$ to a mild acid solution [1], or any other oxidising agents [2]. The electrochemical extraction is carried out by cycling the spinel $LiMn_2O_4$ against lithium reference electrode in an electrochemical cell [3,4]. Before describing the experimental details of the kinetic study of lithium extraction, the laws that describe the diffusion process will be introduced. The following section gives a brief description of the theory of diffusion and Fick's description of such reactions.

Diffusion in solids is best described by Fick's two laws of diffusion [5]. The first law states that the rate of transfer of the diffusing species through of a section of unit area is proportional to the concentration gradient, measured normal to the section, i.e.:

$$J = -D\left(\frac{\partial c}{\partial x}\right) \qquad 5.1$$

where J is the rate of transfer per unit area of section, c is the concentration of diffusing species, D is called the diffusion coefficient and x is the space co-ordinate, measured along the direction of diffusion.

The second law of diffusion states that the rate of change of concentration with time is proportional to the rate of change of concentration with distance, i.e.

$$\frac{\partial c}{\partial t} = \frac{\partial}{\partial x}[D\frac{\partial c}{\partial x}] \qquad 5.2$$

If the diffusion coefficient is independent of position (x), the above equation will become:

$$\frac{\partial c}{\partial t} = D\frac{\partial^2 c}{\partial x^2} \qquad 5.3$$

where symbols are as defined above, and the equation is for diffusion in one dimension. The second law is particularly useful for studying diffusion-controlled reactions. The concentration gradients of the diffusing species in the solid are not easy to measure; therefore, the amounts of species diffused at time t (q_t) were used to solve Fick's second law. To do so, the boundary conditions for the reactions need to be specified. In solids, the boundary conditions, which affect the rate of any diffusion controlled reactions, could be summarised by: -

- The surface area and particle shape;
- The diffusing species' concentration at the surface; and
- The diffusion coefficient in solids.

Equation 5.3 may be easily solved for some boundary condition and insoluble for others. One of the soluble cases is diffusion in semi-infinite solids. At the beginning of the diffusion, the solid will behave as a semi-infinite body, which is described as an infinite surface behind which a solid phase extends to infinity [6].

It is possible to solve Fick's second law of diffusion for a semi-infinite solid with the following boundary conditions:

- Uniform initial concentration of diffusing species all over the solid;
- Constant concentration (C_1) of diffusing species at the surface with respect to time (t); and
- Constant isotropic diffusion coefficient (D) throughout the solid. This assumption is justified due to the fact that the diffusion coefficient will be high at the start of the reaction, so that in the early stages of the reaction, a constant coefficient can be assumed.

Using the above assumptions, Crank [6] quoted the solution

$$q_t = 2C_1\sqrt{\frac{Dt}{\pi}} \qquad 5.4$$

where q_t is the amount of species diffused out of the solid per unit area at time (t).

The diffusion coefficient D is a temperature dependent factor and can be expressed by the Arrhenius type relationship described by Equation 5.5 [7].

$$D = D_o e^{-\frac{E}{RT}} \qquad 5.5$$

where E is the activation energy for diffusion, D_o is a constant, T is the temperature in degrees Kelvin and R is the gas constant. The relationship has a temperature-independent pre-exponential factor (D_o) and an exponential term.

5.2 Kinetic Study of Lithium Extraction from $LiMn_2O_4$

The model described above was applied to the study of lithium diffusion from solid $LiMn_2O_4$. The increase of concentration of lithium ions in solution caused by lithium diffusion from the whole solid sample can be expressed as:

$$Q_t = q_t A \qquad 5.6$$

where Q_t is the amount of lithium ions diffused into solution from the whole powder sample, q_t is the amount of lithium diffused into solution per unit area, and A is the surface area of the powder sample.

From equations 5.4 and 5.6: -

$$Q_t = 2C_1 A\sqrt{\frac{Dt}{\pi}} \qquad 5.7$$

Q_t was experimentally determined and the experimental details of the procedure will be described in this chapter.

In this study, the boundary condition of constant concentration C_1, at the solid surface, throughout the run, was maintained by the relative amounts of solid $LiMn_2O_4$ and solution used. To satisfy the above boundary condition, the amount of solution should be at least ten times bigger than the amount of matter to be exchanged. These amounts correspond to a sufficiently low Berthier ratio. The Berthier ratio is the ratio of exchangeable atoms in the solid and liquid phases [8].

The concentration of diffusing species in solution at equilibrium at $t = \infty$ is Q_∞. All values of Q_t were divided by the total amount of lithium diffused into solution, Q_∞, to give values of the fraction of reaction, $F = Q_t / Q_\infty$, and as at equilibrium $Q_\infty = C_1$, Equation 5.7 gives:

$$F = \frac{Q_t}{C_1} = 2A\sqrt{\frac{Dt}{\pi}} \qquad 5.8$$

By plotting F against $\sqrt{t}$ for each temperature, straight lines are expected (Initial parts of curves in Figure 5.1b and Figure 5.4b) whose slopes are designated m where:

$$m = 2A\sqrt{\frac{D}{\pi}} \qquad 5.9$$

The best values of the slope for each temperature were obtained from the linear portion of the graph.

From Equations 5.5 and 5.9 it follows that:

$$m = 2A\sqrt{\frac{D_o}{\pi}}.e^{(\frac{-E}{2RT})} \qquad 5.10$$

By taking the logarithms of both sides of Equation 5.10:

$$\log_{10} m = \log_{10}(2A\sqrt{\frac{D_o}{\pi}}) - \frac{\mathrm{E}}{2.303 \times 2 \times \mathrm{RT}} \qquad 5.11$$

Values of $\log_{10}$ m were plotted against $\frac{1}{T}$, and from the linear plot values of slope and intercept were calculated by least squares analysis. Plotting the above values should give a straight line from which the values of the activation energy of the diffusion process, E and the temperature-independent factor, D_o, were found as follows: -

$$slope = \frac{-E}{2.303 \times 2 \times R} \qquad 5.12$$

$$\text{intercept} = \log 2A\sqrt{\frac{D_o}{\pi}} \qquad 5.13$$

The fraction of the reaction, F, was also plotted against $t/t_{½}$ where $t_{½}$ is the time for half reaction. The fraction F of the reaction over which the parabolic law is obeyed depends on the variation of the diffusion coefficient (D); but unless this changes discontinuously or extremely rapidly, a well-defined parabolic curve, usually up to at least F = 0.5, is always found.

5.3 Experimental and Results

The experimental details of the lithium extraction reaction from $LiMn_2O_4$, and the results obtained are given in the following sections.

5.3.1 Chemicals

Lithium manganese oxide $LiMn_2O_4$ used throughout this work was prepared using the optimised firing technique described in Chapter 3. G.P.R. grade sulphuric acid was purchased from B.D.H. The water used was double distilled de-ionised water.

5.3.2 Reaction Conditions

The reaction was carried out at various but constant temperatures. These temperatures were obtained by means of thermostatted water bath controlled to within ±0.05 °C. For temperatures below room temperature, a cooler was placed in the water bath and kept there for at least 24 hours before commencing any reaction.

The determination of lithium concentration was carried out using atomic absorption spectroscopy, as described in Chapter 2.

5.3.3 Method

In order to investigate the kinetics of lithium diffusion from $LiMn_2O_4$, the procedure below was followed.

An acid solution at pH = 2 was prepared using concentrated sulphuric acid and distilled water. The solution was kept at the desired reaction temperature. 2 ml aliquots of the acid solution were added to centrifuge tubes containing accurately weighed samples of about 0.1 g of $LiMn_2O_4$ and the suspension stirred. These aliquots were kept for different but increasing periods of time at a constant temperature. The tubes were removed from the bath, centrifuged and the supernatant liquid and the solid were analysed for lithium content using atomic absorption spectroscopy. Using the same arrangement, a sample of $LiMn_2O_4$ was acid treated for at least 24 hours at 30 °C and the results obtained from that were used to calculate the concentration of lithium at equilibrium (Q_∞). To cover a wide range of temperatures, the above procedure was carried out at 2, 10, 25 and 30 °C.

The values of m are tabulated in $min^{-½}$, since time was measured in minutes. In order to convert to S.I. units, all values of slope and intercept were divided by a factor of $\sqrt{60}$ in order to convert $min^{-½}$ to $s^{-½}$.

5.3.4 Lithium concentration in the solution

The concentrations of lithium in solution were measured at the specified times and temperatures. The fractions of the reaction, F, were subsequently calculated by dividing all the results, Q_t, by the concentration of lithium in solution at equilibrium, Q_∞.

When the fractional lithium concentrations F were plotted against √time in Figure 5.1, it was observed that all the initial stages of all the kinetic runs obey a parabolic law. A parabolic law is often indicative of diffusion controlled kinetics and arises from diffusion with a semi-infinite geometry.

From the slope of the linear part of the line at 25 °C and using Equations 12 and 13, the activation energy of the diffusion process was found to be 40.22 ± 0.9 kJ mol^{-1}, and D_o was calculated to be 3.62 x 10^{-7} cm^2 s^{-1} . Thus, D for the system may be written as:

$$D = 3.62 \times 10^{-7} . e^{-\frac{40.22}{RT}}$$

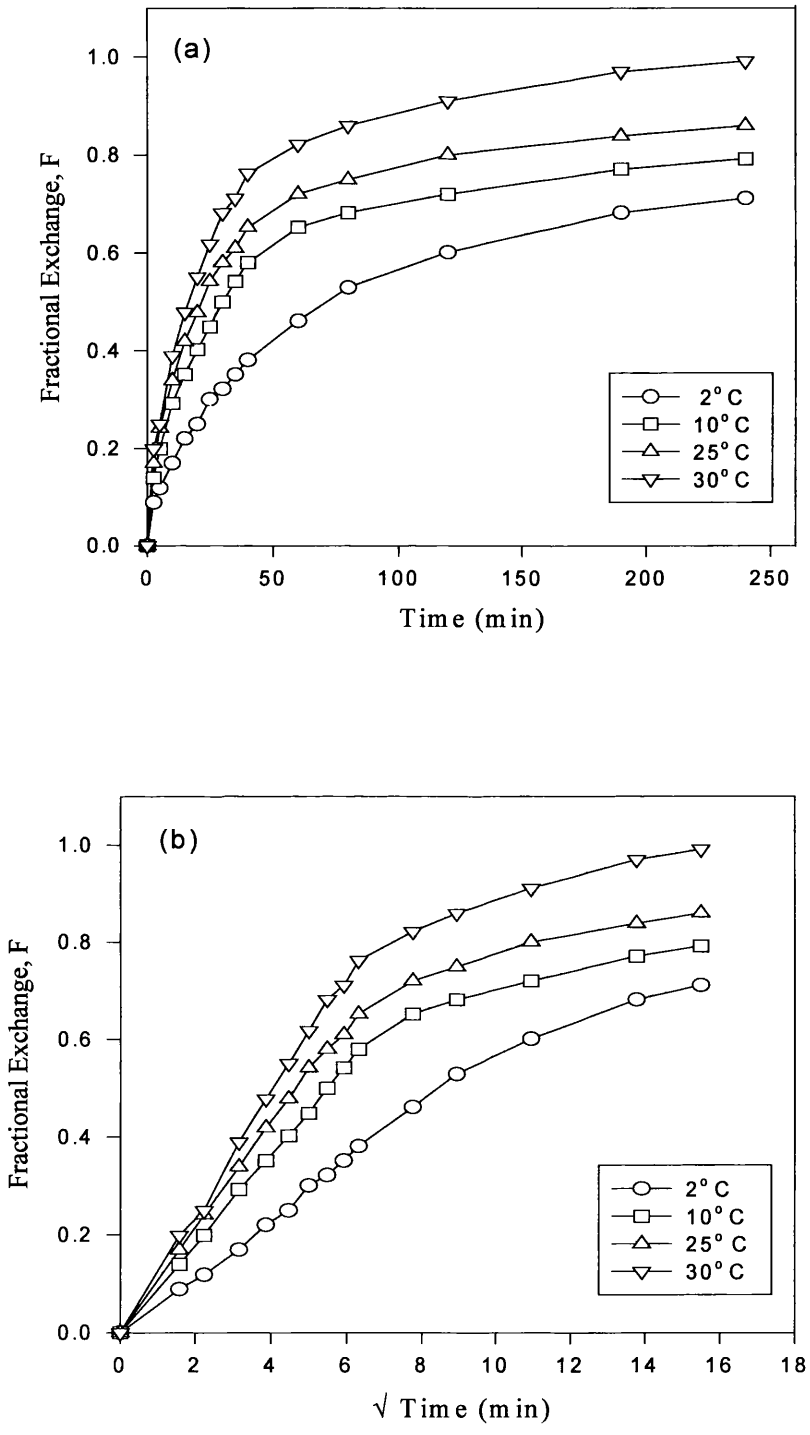

Figure 5.1 Lithium extraction results obtained from the concentration of lithium in the supernatant, (a) against time, (b) against √ time.

5.3.5 Lithium concentration in the solid

The amounts of lithium in the solid samples produced in Section 5.3.3 were also determined. The solid samples were first dissolved by adding a mixture of 2 ml of concentrated hydrochloric acid, 2 ml of concentrated sulphuric acid and about 5 ml of distilled water. The mixture was boiled until the whole sample was dissolved. The solution was diluted to 100 ml in a volumetric flask. The amount of lithium in each solution was determined using Atomic Absorption Spectroscopy as described in Chapter 2. The results obtained were treated in a similar fashion to those described in the previous section.

The fractional lithium concentration (F) was plotted against √time as shown Figure 5.2. The initial stages of all the runs obey a parabolic law but in a decreasing order. This result confirms the initial findings of the kinetic data obtained from the amount of lithium diffused into solution. As mentioned earlier, the parabolic law indicates a diffusion-controlled process from a semi-infinite surface in the initial stages.

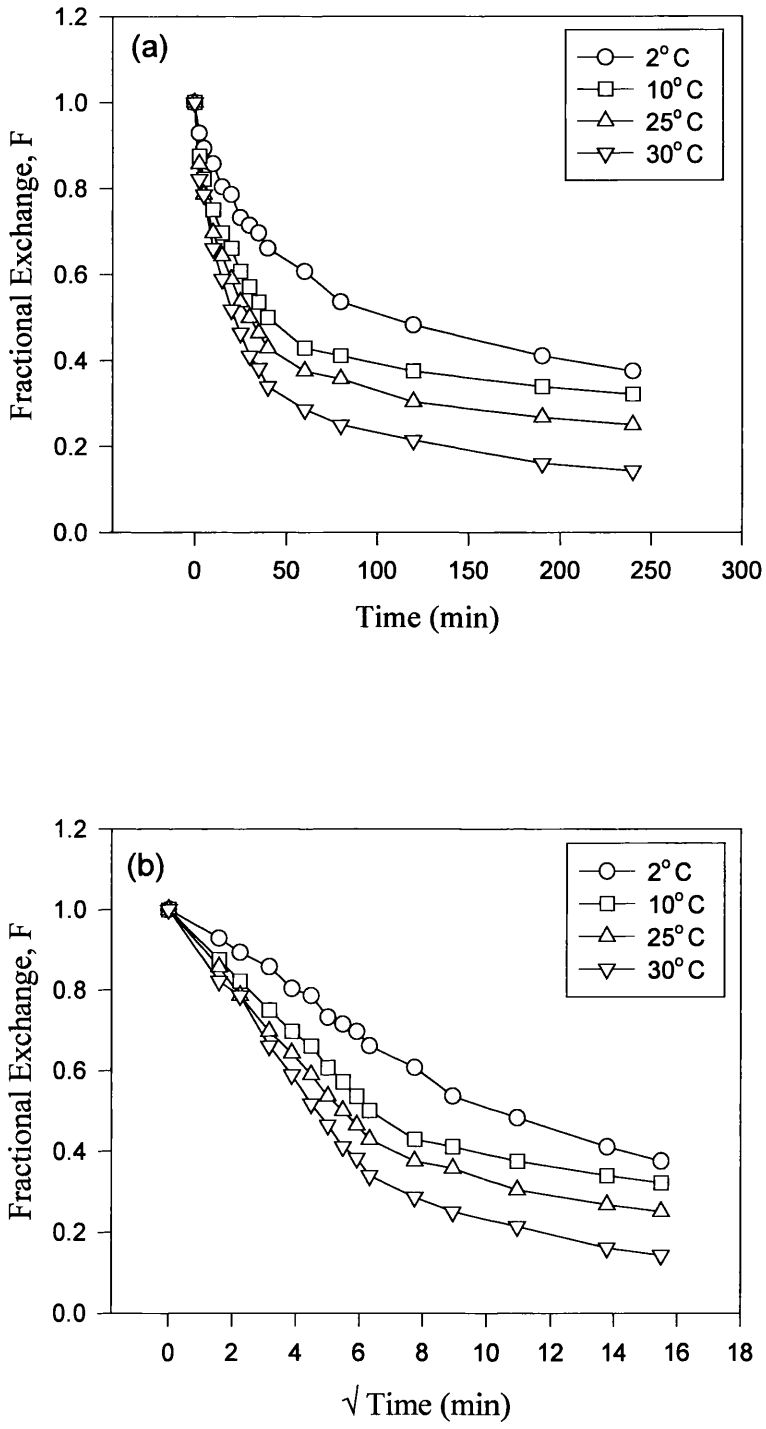

Figure 5.2 Lithium extraction results obtained from the concentration of lithium remaining in the solid, (a) against time, (b) against √time.

From that linear part of the line at 25 °C, the activation energy was calculated and found to be 34.81 ±0.7 kJ mol^{-1}, and D_o was found to be 3.41 x 10^{-7} cm^2 s^{-1}. Thus D for the system found using the residual lithium concentration in the solid after the extraction process might be written as: -

$$D = 3.41 \times 10^{-7} . e^{\frac{34.81}{RT}}$$

5.4 Discussion

The extraction of lithium from spinel $LiMn_2O_4$ is accompanied by the oxidation of manganese (III) to manganese (IV) and produced a defective cubic spinel phase, which was identified by X-ray diffraction. As the product phase is structurally similar to the original material, the extraction-oxidation process can be described as topotactic. The unit cell parameters of the product were measured and found to have reduced, as discussed in Chapter 4.

The kinetic curves presented in this chapter suggest that the process of lithium extraction and manganese oxidation is diffusion-controlled.

For each technique used, D parameters were evaluated as follows:

$$D_{Solution} = 3.62 \times 10^{-7} . e^{-\frac{40.22}{RT}} = 3.56 \times 10^{-7}\ cm^2\ s^{-1}$$

$$D_{Solid} = 3.41 \times 10^{-7} . e^{-\frac{34.81}{RT}} = 3.36 \times 10^{-7}\ cm^2\ s^{-1}$$

where $D_{Solution}$ and D_{Solid} are the diffusion coefficients found using the lithium concentration in solution and in the solid respectively. The diffusion coefficient of lithium extraction from $LiMn_2O_4$ found by measuring the concentration in the solid (D_{Solid}) had a value similar to those found using Galvanostatic Intermittent Titration Technique (GITT) [9, 10, 11, 12]. See Table 1.2.

5.4.1 Diffusion Process

As already mentioned, the extraction process of lithium from $LiMn_2O_4$ is a diffusion-controlled reaction. Diffusion may involve the displacement of oxides, or cations or both. Because of their smaller size, cations are more likely to diffuse than anions, and yet the oxide ion, in spite of its large ionic radius (1.40 Å) and electronic charge of two, diffuses in quite a number of oxidation-reduction reactions in solid oxides, especially those with fluorite –like lattices.

As an example, in UO_2, the four interstitial sites will accommodate extra ions and will even accept oxide ions, since the radius ratio of cation to anion is sufficiently large. Such sites are co-ordinated by oxide ions, and so the interstitial oxide suffers repulsion. The high charge of 6+ on the uranium ion reduces these repulsion forces by polarisation, and so the enthalpy of formation of an interstitial oxide ion is considerably reduced, enabling the oxide ion to move easily to these interstitial sites in the bulk oxidation of UO_2 (See Figure 5.3) [13, 14, 15, 16].

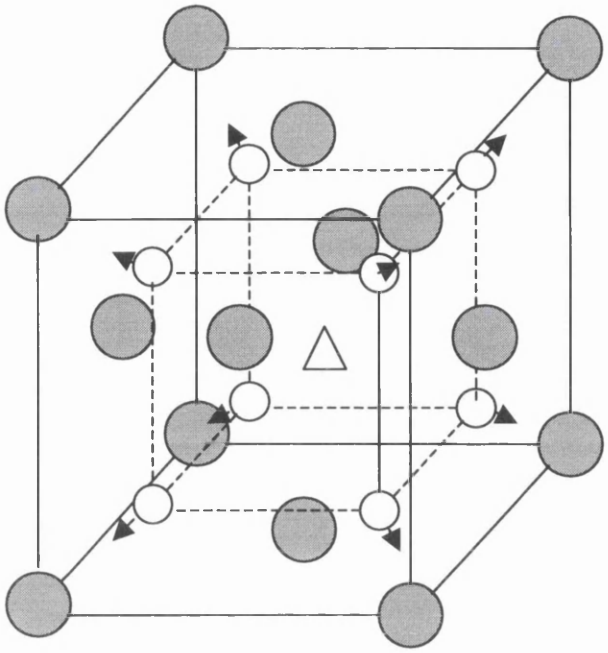

Figure 5.3 The fluorite unit cell of UO_2. There are interstitial sites at ½ ½ ½ (triangle) at ½ 0 0, 0 ½ 0, and 0 0 ½.

In the case of $LiMn_2O_4$ and λ-MnO_2, which are systems in which the oxide ions are cubic close-packed, the concentration of interstitial oxide ions will be negligible, and so the most probable mechanisms of oxide diffusion are those involving Schottky defects. A Schottky defect is a stoichiometric defect found in ionic crystals where a pair of vacant sites exists, an anion vacancy and a cation vacancy [17]. However, the concentration of Schottky defects will be insignificant compared to the concentration of interstitial cations, since interstitial sites are equivalent to lattice cation sites (same size and same co-ordination). Therefore mechanisms involving cation migration via interstitial sites must predominate. For these reasons, the cation diffusion model is the only one that will be discussed. In this model, the cations diffuse from the interior of the solid to the surface where they dissolve into solution and slightly shrink the lattice.

5.4.2 Cation Diffusion Process

As mentioned in Chapter 1, the spinel structure of stoichiometric A^{2+} B_2^{3+} O_4 is formed by distributing cations among the interstitial sites of a cubic close packed array of oxygen ions such that one-eighth of the tetrahedral positions and one half of the octahedral positions are occupied. We may have: (1) an inverse spinel in which all A^{2+} cations are in octahedral sites e.g. Fe_3O_4, and (2) a normal spinel where all B^{3+} cations are in octahedral sites e.g. $MgAl_2O_4$, or (3) a partly or fully random distribution as in $MnFe_2O_4$ [18]. $LiMn_2O_4$ is a normal spinel where all lithium ions are in tetrahedral sites and all manganese ions are in octahedral sites.

Generally, there are three basic mechanisms of diffusion, each of which will be described and discussed.

(a) Interstitial Mechanism

A cation is said to diffuse by the interstitial mechanism when it passes from one interstitial site to one of its nearest neighbour's interstitial sites without permanently displacing any of the matrix ions. As can be seen in Figure 5.4, cations diffuse by the interstitial mechanism by jumping from one site to another.

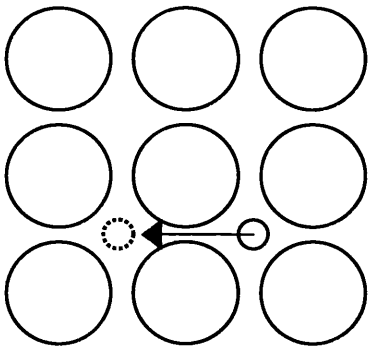

Figure 5.4 The elementary atomic step in interstitial diffusion.

(b) Vacancy Mechanism

In most crystals, some of the lattice sites are unoccupied, and these unoccupied sites are called vacancies. If one of the cations on an adjacent site jumps into the vacancy, the cation is said to have diffused by the vacancy mechanism.

The mechanism as shown in Figure 5.5 illustrates that the distortion required to move a cation is small. In fact, the distortion energy put into a lattice to move a cation into an adjacent vacancy is roughly equal to the energy required to move the cation from one interstitial site to another within the same lattice. [19]

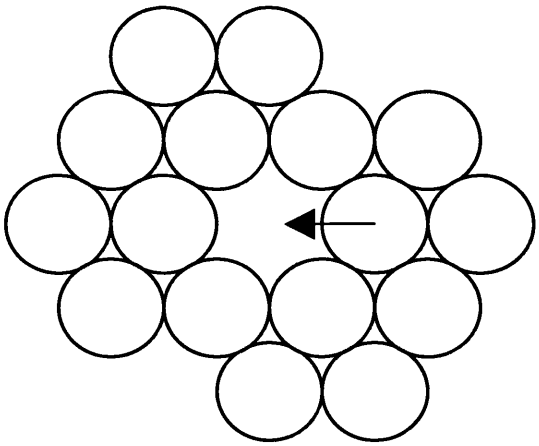

Figure 5.5 The elementary atomic step in vacancy diffusion.

(c) Interstitialcy Mechanism

If a cation diffuses by shoving one of its nearest adjacent atoms into an interstitial position and occupying its site, the diffusion mechanism is called an interstitialcy mechanism, which is illustrated in Figure 5.6.

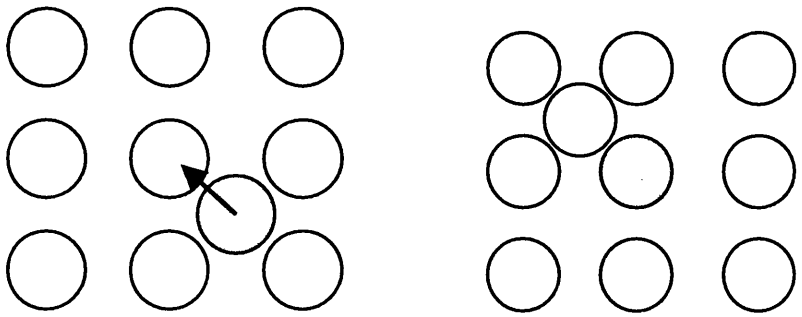

Figure 5.6 The elementary atomic step in the interstitialcy mechanism.

It is obvious that the distortion caused by the interstitialcy movement will be higher than that in the interstitial and vacancy mechanisms, so the significant increase in activation energy makes this mechanism very unlikely in these systems. This type of diffusion mechanism is found largely in the diffusion of Ag in AgBr [20].

5.4.3 Possible Diffusion Mechanism

The relative contributions of the above mechanisms to the rate of diffusion will now be considered.

Due to the increase in activation energy caused by the high degree of distortion required by the interstitialcy mechanism and the low values of the activation energy measured for $LiMn_2O_4$ (34.8-40.22 kJ mol^{-1}), the interstitialcy mechanism clearly does not operates in this system.

In the vacancy mechanism there are two main components controlling the rate of diffusion of the cation: vacancy concentration and vacancy size.

As the vacancy concentrations are very small at the beginning of the oxidation of the spinel system, each cation must wait for a considerable time before a vacancy becomes available. Therefore a vacancy mechanism is not likely to be important in the early stages of the process. As the system oxidises and cations migrate to the surface, more and more vacancies are created on octahedral and tetrahedral sites. Apparently, the vacancy mechanism would be expected to become more important as oxidation progress; in fact, these vacancies are used as interstitial sites during the diffusion

process. This type of behaviour is found in structure of γ-Fe_2O_3, which is related to the $LiFe_5O_8$ structure, but with holes and cations arranged in the order Fe □□ Fe □□ Fe □□ Fe □□ Fe along a spiral of 'lithium' sites [21]. In the system under study, the extraction reaction of lithium in aqueous solution is relatively fast when compared to equivalent reaction carried out electrochemically, therefore the contribution of vacancy mechanism to the diffusion process is believed to be negligible. However, a recent study of the charge order transition of $LiMn_2O_4$ by means of anelastic spectroscopy found evidence of the stress-induced jump of charges from Mn^{3+} to Mn^{4+} sites at around 100K, an action analogous to that found in Fe_2O_3 [22].

This leaves the interstitial mechanism as a possible and predominant path for the diffusion of cations in $LiMn_2O_4$.

The interstitial mechanism is a process in which cations move by jumping into adjacent interstitial sites, as can be seen in Figures 5.4 and 5.7. There are tetrahedral and octahedral interstitial sites in the spinel structure and both could be involved in the diffusion process. To decide which of these interstitial sites could contribute to the diffusion process, differences in the crystal field stabilisation energy (CFSE) and electrostatic energy contribution between octahedral and tetrahedral sites when occupied by Li^+, Mn^{3+}, and Mn^{4+} in the $LiMn_2O_4$ system will later be considered.

By examining the spinel structure, we can see that despite the fact that tetrahedral interstitial sites are separated by 0.684 d/Å from octahedral cations, the cations will

move through the path of minimum energy, which will be the path with the lowest barrier, where d is the distance between a cation and an oxide ion in the spinel lattice.

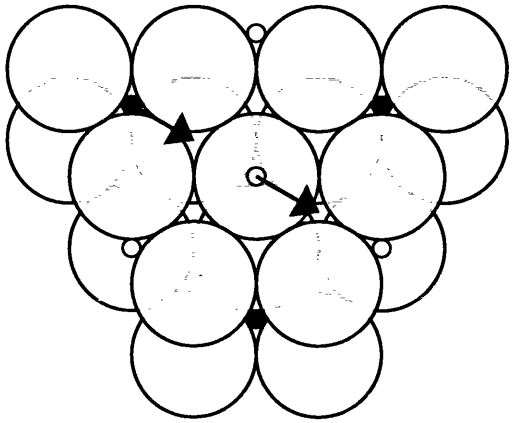

Figure 5.7 Interstitial mechanism in a close-packed layer of $LiMn_2O_4$ (○ Li, ● Mn).

There are two possible pathways that can be considered. First is a pathway in which the cation moves through a saddle point where it is 0.707 d/Å from two oxygens and with which it is co-linear. Second is a pathway in which the cation passes through the centre of a triangle, and is therefore equidistant from the oxide ions at the corners of this triangle, at a distance of 0.816 d/Å from each oxide ion. It is clear from the above considerations that a cation in the centre of the triangle will be at a greater distance from the oxides (by 0.109Å) when compared with a cation at the saddle point where it is co-linear with two oxide ions. The increase in the distance will cause the repulsion energy in the centre of the triangle to be about 27% less than at the other saddle point. Therefore the triangular pathway is the preferred one for cation migration.

The measured activation energies for cation migration generally include two terms: one is the difference in electrostatic energy between the normal site and the saddle point i.e. the trigonal site; the other is a crystal field stabilisation energy term, which will be the difference between the CFSE's of cations in normal sites and trigonal sites.

The calculated d-orbital energy levels in octahedral and trigonal symmetries which have been reported in the literature are nearly the same [23]. The difference in electrostatic energy for Mn^{3+} in octahedral and trigonal positions was calculated to be ~137 kJ mol^{-1} [18]. Since the measured activation energies (34.81-40.22 kJ mol^{-1}) are significantly lower, such Mn^{3+} ions would not be able to overcome the energy barrier and diffuse. See Figure 5.8.

As listed in table 1.1, the calculated CFSE in oxides for octahedral Mn^{3+} (d^4) is 135.4 kJ mol^{-1} and for octahedral Mn^{4+} (d^3) ions is 244.5 kJ mol^{-1}.

By combining the above Mn^{3+} ions discussion and the values of CFSE for both Mn^{3+} and Mn^{4+}, it is clear that Mn^{4+} ions would require an even higher activation energy than Mn^{3+} in order to diffuse. From that it can be concluded that Mn^{4+} will also not be able to contribute to the diffusion process.

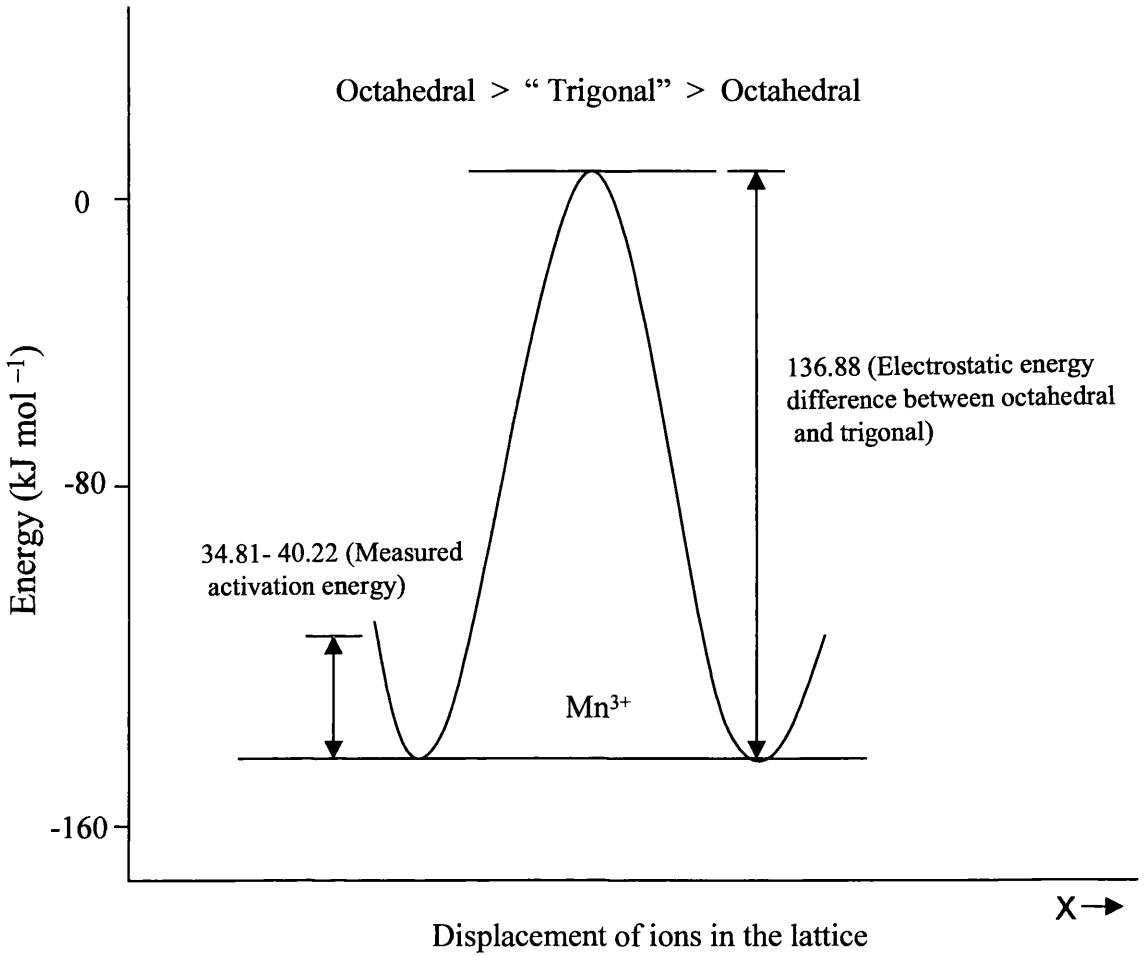

Figure 5.8 Schematic diagram of energy changes for diffusion of Mn^{3+} in the spinel lattice.

Although octahedral manganese ions in the spinel $LiMn_2O_4$ do not diffuse because of the high activation energies, small amounts of manganese were detected in solution when analysed by Atomic Absorption Spectroscopy. The presence of manganese in solution is thought to be the result of the formation of a small amount of Mn^{2+}. Despite the fact that Mn^{2+} (d^5) has a zero CFSE, it would not be able to diffuse to a neighbouring interstitial octahedral site due to the high electrostatic energy of the saddle point (85.96 kJ mol^{-1}) [18]. In this work and in the literature, x-ray and neutron

diffraction examination of the resultant MnO_2 prepared by various techniques did not show any evidence of Mn^{2+} occupying tetrahedral sites [24, 25]. Such evidence is manifested in the Bragg reflection [220], the intensity of which is related to the tetrahedral site occupancy. However, the product of the electrochemical oxidation of $LiMn_2O_4$ did show the presence of Mn^{2+} as confirmed by electron paramagnetic resonance [26]. Hunter [1] explained this phenomenon by electrons moving between neighbouring Mn^{3+} cations to form Mn^{4+} and surface Mn^{2+} cations that subsequently dissolve into solution. The validity of this statement will be discussed in Chapter 5 in relation to the lithium insertion reactions of spinel λ-MnO_2.

The decrease in the unit cell dimensions is thought to be the result of both the removal of lithium ions from the lattice and the removal of the Jahn-Teller effect by the oxidation of all Mn^{3+} to Mn^{4+}.

Cations occupying tetrahedral sites will have similar movements to those occupying octahedral sites and therefore will pass through the same saddle points. So for lithium ions to diffuse through such saddle points, they should have enough energy to overcome the energy barrier possessed by such points. The coordination number for lithium ranges from two to twelve and can be any number in between, though four is most common. Hence, lithium ions favour tetrahedral sites with co-ordination number four [27]. This was confirmed by a neutron diffraction study of a delithiated sample of $LiMn_2O_4$ [24].

Energy barriers, or the energy differences between normal lattice sites, tetrahedral and octahedral, and trigonal sites (saddle points) for Li^+ ions have been calculated by

Atanasov *et al.* [28]. For a lithium ion to move from a tetrahedral site through the saddle point to a neighbouring interstitial tetrahedral site requires at least 15.44 kJ mol^{-1} and for the equivalent octahedral move at least 91.65 kJ mol^{-1} is required, as can be seen in Figure 5.9.

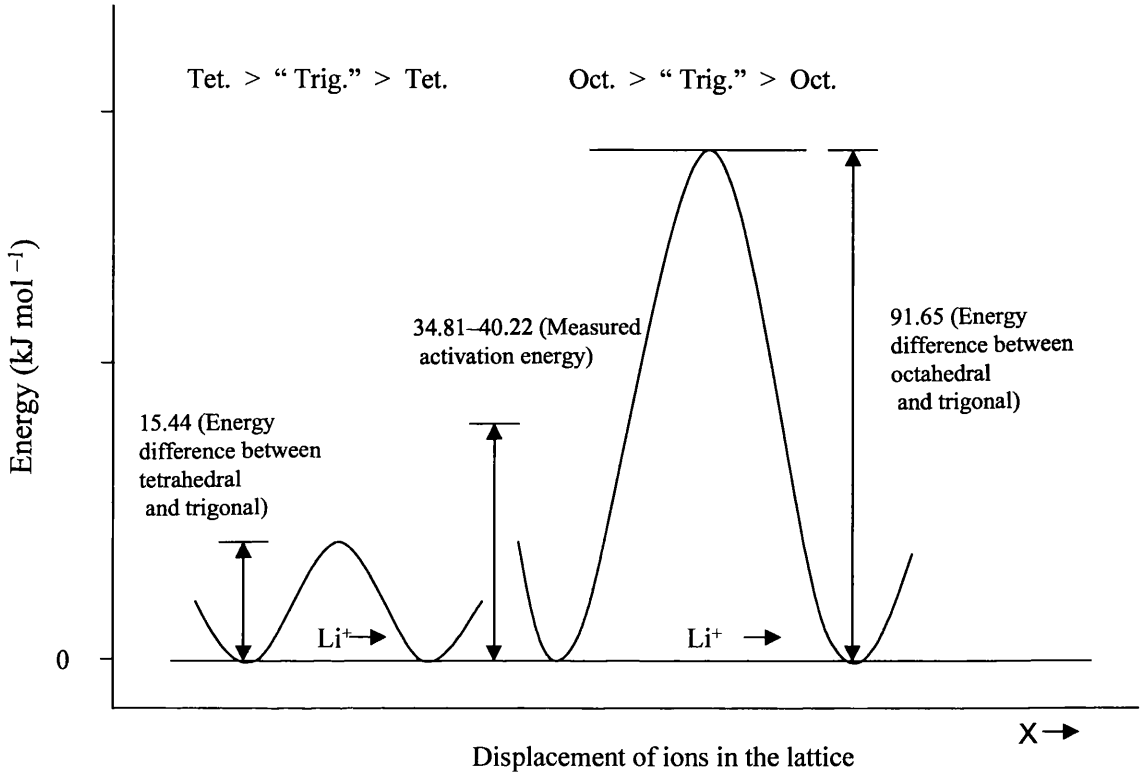

Figure 5.9 Schematic diagram of energy changes for diffusion of Li^+ in the spinel lattice.

By comparing the energy values required for Li^+ to overcome each saddle point and the activation energy of reaction, it can be concluded that Li^+ ions would preferentially diffuse through to a neighbouring tetrahedral interstitial site and continue the diffusion process through to the next tetrahedral interstitial site. These interstitial tetrahedral sites form a network of tunnels with a radius of 1.286 Å [28], large enough for the Li^+ to

move with minimal activation energy when compared to that required for migration between octahedral interstitial sites. Li^+ with a co-ordination number of four has been reported to have ionic and crystal radii of 0.59 Å and 0.73 Å respectively [29]. From the high activation energy value of 91.65 kJ mol^{-1} required for Li^+ to diffuse to octahedral sites, it can be concluded that despite their availability, Li^+ would not move to neighbouring octahedral interstitial sites.

The 3D tunnels of interstitial tetrahedral sites are clearly visible by inspecting the spinel structures shown in Figures 1.2, 1.5 and 5.10. Figure 1.2 shows the locations of the A and B ions within the normal spinel structure while Figure 1.5 shows the spinel structure $[B_2O_4]$ with the tetrahedral A ions removed. On the other hand, Figure 5.10 shows the spinel structure with eight tetrahedral interstitial sites and four octahedral interstitial sites per AB_2O_4 unit.

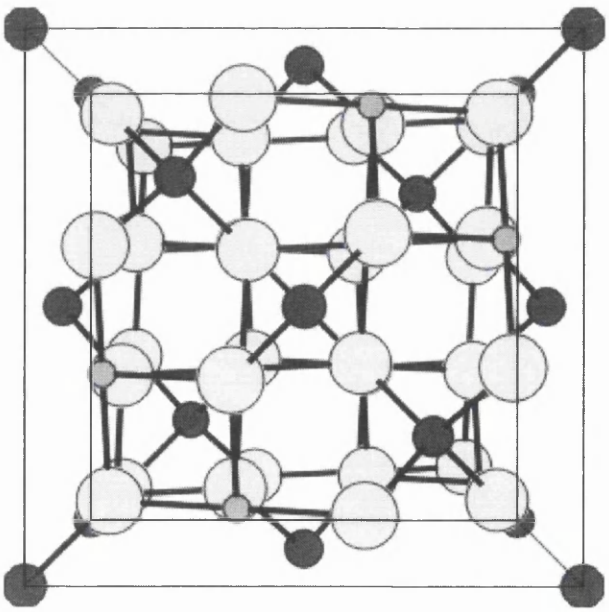

Figure 5.10 Normal spinel structure AB_2O_4 [30]

5.5 Conclusion

The kinetic investigation of the oxidation of the normal spinel $LiMn_2O_4$ by the chemical extraction of Li^+ revealed that the extraction process is diffusion-controlled process. During the diffusion process, cations were migrating via interstitial sites. In this system, Li^+ is the only diffusing cation and is migrating via tetrahedral interstitial sites, as discussed.

The measured activation energy (i.e. 34.8 and 40.22 kJ mol^{-1}) for the oxidation of $LiMn_2O_4$ compared with the difference in the CFSE's of Mn^{3+} and Mn^{4+} in different sites and the electrostatic energy barriers, clearly showed that these ions were not able to overcome the energy barrier (i.e. ~137 kJ mol^{-1}) and diffuse. On the other hand, tetrahedral Li^+ cations, because of their low energy barrier (i.e. ~15 kJ mol^{-1}) compared with the activation energy, would diffuse.

Li^+ cations would diffuse through the lattice using the adjacent interstitial tetrahedral sites and avoid the adjacent interstitial octahedral sites due to their high energy barrier (~92 kJ mol^{-1}). Li^+ cations (r = ~0.7 Å) will diffuse easily through the network of 3D tunnels formed by interstitial tetrahedral sites (r = ~1.3 Å), causing the unit cell of the resulting Mn_2O_4 framework to shrink slightly (a = 8.08 Å) when compared with the starting $LiMn_2O_4$ (a = 8.24 Å). The oxidation of Mn^{+3} to Mn^{4+} and the consequent removal of the Jahn-Teller effect are thought to contribute to unit cell reduction.

References

1 J. Hunter, *J. Solid State Chem.*, **39**, 142 (1981).

2 A. Mosbah, A. Verbaern, and M. Tounoux, *Mat. Res. Bull.*, **18**, 1375 (1983).

3 M.M. Thackeray, P. Johnson, L. de Picciotto, P. Bruce, and J. Goodenough, *Mat. Res. Bull.*, **19**, 179 (1984).

4 M.M. Thackray, L. de Picciotto, A. de Cock, P. Johnson, U. Nicholas, and K. Adendorff, *J. Power Sources*, **21**, 1 (1987).

5 A. Fick, *Ann. Phys.*, LP2, **170**, 59 (1855).

6 J. Crank, *Mathematics of Diffusion*, Oxford University Press, Fair Lawn, N.Y. (1956).

7 P.G. Shewmon, *Diffusion in Solids*, McGraw-Hill, N.Y. (1963).

8 K.J. Gallagher and D.N. Philips, *Trans. Farad. Soc.*, **64**, 785 (1968).

9 L. Chen, X. Huang, E. Kelder, and J. Schoonmann, *Solid State Ionics*, **76**, 91 (1995).

10 L. Chen and J. Schoonman, *Solid State Ionics*, **67**, 17 (1993).

11 M.Y. Saidi, J. Barker, and R. Koksbang, *J. Solid State Chem.*, **122**, 195 (1996).

12 M. Mohamedi, D. Takahashi, T. Itoh, and I. Uchida, *Electrochim. Acta,* **47**, 3483 (2002).

13 J.S. Anderson, L.E.J. Roberts, and E.A. Harper, *J. Chem. Soc.*, 3946 (1955).

14 Z. Dachs, *Z. Krist.* **2**, 791 (1956).

15 J.M. Honig, A.F. Clifford, and P.A. Faeth, *Inorg. Chem.*, **2**, 791 (1963).

16 B.G. Hyde, D.J. M. Bevan, and L. Eyring, *Phil. Trans. Roy. Soc.*, **A, 259**, 583 (1966).

17 A.R. West, *Solid State Chemistry and its Applications*, John Wiley & Sons, New York (1984) p320.

18 A. Nazemi, *Oxidation and Reduction Studies in Oxides with Spinel Structures*, Ph.D. thesis, University of Wales Swansea (1979).

19 H Schmalzried, *solid state reactions*, Academic Press Inc. New York (1974) p.57.

20 P.G. Shewmon, *Diffusion in Solids*, McGraw-Hill, New York (1963) p.151.

21 G.W. Van Oosterhout and C.J.M. Rooymans, *Nature*, **181**, 44 (1948).

22 A. Paolone, R. Cantelli, G. Rousse, and C. Masquelier, *J. Physics: Condensed Matter,* **15**, 457 (2003).

23 F. Basolo and R.G. Pearson, *Mechanism of Ionic Reactions*, John Wiley & Sons Inc., New York (1958) p.55.

24 H. Berg and J.O. Thomas, *Solid State Ionics*, **126**, 227 (1999).

25 H. Berg, H. Rundlov, and O.J. Thomas, *Solid State Ionics*, **144**, 65 (2001).

26 K. Kanamura, H. Naito, T. Yao, and Z. Takehara, *J. Mater. Chem.*, **6**, 33 (1996).

27 M. Hakansson, C.H. Ottoson, A. Boman, and D. Johnels, *Organometallics*, **17**, 1208 (1998).

28 M. Atanasov, J.L. Barras, L. Benco, and C. Dual, *J. Am. Chem. Soc.*, **122**, 4718 (2000).

29 R.D. Shannon, *Acta Crystallographica*, **A32**, 751 (1976).

30 H. Kleinke, *Inorganic Transition Metal Chemistry Course*, University of Waterloo, Canada, (2003). Available at http://hk2.uwaterloo.ca/310/2001_1.html (2 January 2004)

Chapter 6

Lithium Ion Insertion Reactions with Spinel Manganese Oxides

In this chapter, the insertion reaction of lithium ions into λ-MnO_2 is discussed. A new chemical reaction was developed for the insertion of lithium ions into λ-MnO_2. The insertion reaction was performed under different reaction conditions to establish the best reaction environment. The spinel $LiMn_2O_4$ was formed as the end product of the chemical insertion of lithium into λ-MnO_2.

6.1 Introduction

Metal ion insertion into λ-MnO_2 has been studied using the system λ-MnO_2 and (MCl + MOH), where M is Li, Na, K, Rb, or Cs. The adsorptive capacities of alkali metal ions increase in the order $K^+ < Rb^+ < Cs^+ < Na^+ << Li^+$ at pH 10. These results could be easily explained on the basis that the vacant tetrahedral sites in λ-MnO_2 are too small for metal ions, apart from Li^+ and H^+, to enter [1]. Further studies have been done on the topotactic insertion of lithium into λ-MnO_2 using the above system [2, 3, 4, 5].

During the preparation of λ-MnO_2 from $LiMn_2O_4$, some of the manganese was dissolved into solution [6], as can be seen in the equation below.

$$2LiMn_2O_4 + 4H^+ \rightarrow 3\lambda - MnO_2 + 2Li^+ + Mn^{2+} + 2H_2O \qquad 6.1$$

All the reported work on the lithium ion reactions treated the spinel λ-MnO_2 as an intercalation agent and concentrated on the ion exchange ability of the oxide, hence ignoring the role of the dissolved manganese on the insertion reaction. In the present work, lithium insertion into spinel λ-MnO_2 has been studied in the absence and the

presence of manganese, in order to study the effect of manganese on the reversibility of the above reaction. The effects of different reaction conditions e.g. temperatures and times, on the lithium insertion reaction were also investigated. Spinel λ-MnO_2 used in these experiments had been prepared by the acid treatment of $LiMn_2O_4$, as described in Chapter 4.

6.2 Lithium Ion Insertion at 20 °C with $MnCl_2$

Lithium ion insertion into spinel λ-MnO_2 has been studied using lithium and manganese chlorides at room temperature. In order to study the insertion reaction, the procedure in section 6.2.1 was devised. The result of the reaction is designated as sample I-1.

6.2.1 Experimental

100 ml of 2M $MnCl_2.4H_2O$ and 100 ml of 2M LiCl were mixed together in a 400 ml beaker. The mixture had a pH reading of about 5. The temperature of the reaction was set to room temperature (20 °C) using a temperature controlled water bath to within ±0.05 °C. 1 g of powdered λ-MnO_2 was added to the chloride mixture causing the pH to drop to about 1.5. The pH of the solution was adjusted with a drop of 2M LiOH to about 2.5. The solution was kept stirred for the whole course of the reaction. The pH was adjusted four times over a period of 24 hours to settle on a constant pH value of 3.81. The solid precipitate, designated sample I-1, was collected by filtration using a Gooch crucible and dried at 100 °C.

6.2.2 Results and Discussion

The product of the reaction, sample I-1, showed an increase in weight of about 20%, which could be attributed to lithium and manganese uptake by λ-MnO_2, or to the surface and molecular water attached to the sample despite drying at 100 °C.

The lithium concentration in sample I-1 was determined using Atomic Absorption Spectroscopy, as described in Chapter 2, and found to be 3.61%. The amount of lithium found in sample I-1 is in good agreement with the theoretical lithium concentration in $LiMn_2O_4$ (3.84%) and with the amount of lithium in the original $LiMn_2O_4$ prepared in this work (3.73%) as described in Chapter 3. This is a positive indication of a possible lithium insertion into λ-MnO_2.

Identification of the product using the x-ray diffraction technique showed that the solid precipitate had a diffraction pattern similar to that of $LiMn_2O_4$, except that the lines were a bit diffuse and broader than those of $LiMn_2O_4$. This indicates the diffusion of lithium into the spinel λ-MnO_2 crystal structure and the formation of the spinel $LiMn_2O_4$. The x-ray diffraction pattern of the product, sample I-1 is shown in Figure 5.1 along with those of λ-MnO_2 and $LiMn_2O_4$ for comparison. Table 6.1 lists d-values/Å of the lithium-inserted λ-MnO_2, sample I-1, with those of λ-MnO_2 and $LiMn_2O_4$. By comparing d-values/Å for sample I-1 with those of λ-MnO_2 and $LiMn_2O_4$, the increase in the lattice parameters of λ-MnO_2 as a result of lithium insertion and the formation of $LiMn_2O_4$ can easily be seen. From the data in Table 6.1, the lattice constant (a) for each of these samples was calculated to be: 8.3, 8.108 and 8.24 Å for $LiMn_2O_4$, λ-MnO_2 and sample I-1 respectively.

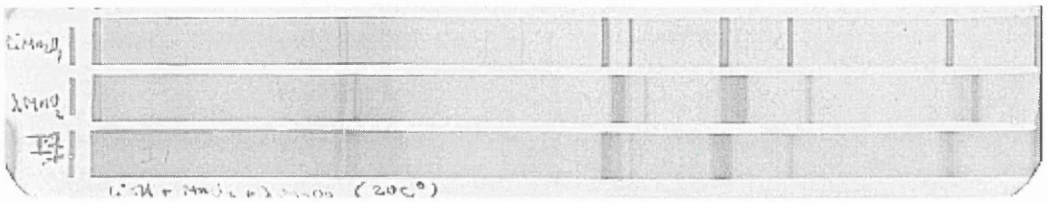

Figure 6.1 X-ray diffraction patterns of $LiMn_2O_4$, λ-MnO_2 and sample I-1.

Table 6.1 d-values/Å of $LiMn_2O_4$, λ-MnO_2 and sample I-1.

hkl	d-values/Å $LiMn_2O_4$	d-values/Å λ-MnO_2	d-values/Å sample I-1
111	4.763	4.663	4.732
311	2.483	2.427	2.505
222	2.375	2.328	2.394
400	2.075	2.027	2.060
331	1.895	1.833	1.883
333	1.585	1.550	1.576
440	1.460	1.425	1.454

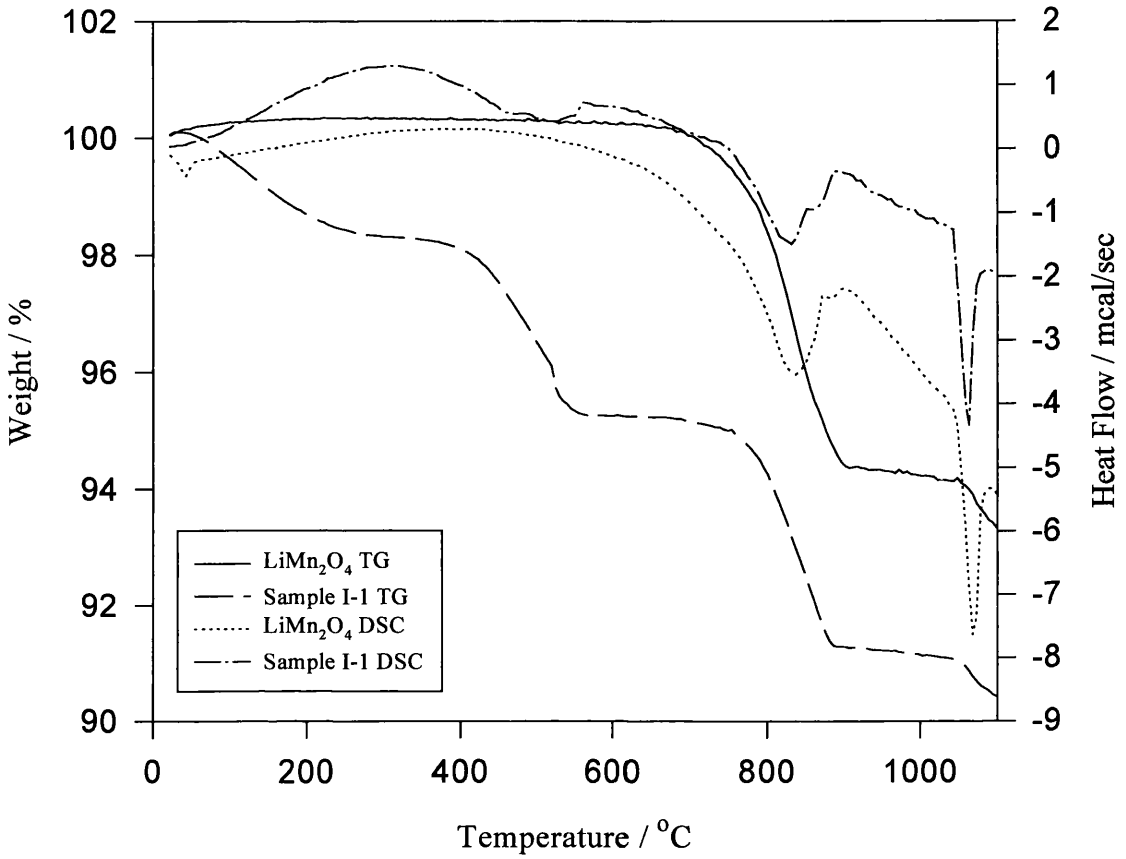

Figure 6.2 Thermal analysis results for sample I-1 and $LiMn_2O_4$.

Thermogravimetric analysis (TG) revealed that the product undergoes three weight changes, as can be seen in Figure 6.2. The loss in the first step was approximately 2% by mass during heating to 250 °C; this mass loss could be attributed predominantly to adsorbed water on the surface of the particles and to molecular water. In the second step, the sample lost approximately 3% by mass during heating to 600 °C. This could be attributed to the removal of more strongly bonded water or hydroxyl groups, or to the

conversion of the remaining MnO_2 to Mn_2O_3, since it coincides with the temperature at which MnO_2 transforms to Mn_2O_3 in the analysis of λ-MnO_2 (Figure 4.4). This would correlate with the broad and diffuse lines in the sample diffraction pattern. The removal of the water and the transformation to Mn_2O_3 were also manifest by the endothermic peaks below 600 °C in the DSC data in Figure 6.2. The third mass loss in the sample's TG of about 4% is similar to that found on heating $LiMn_2O_4$ to the same temperature, as illustrated during discussion of the thermal stability study of $LiMn_2O_4$ in Chapter 3.

6.3 Acid Treatment of Sample I-1

In order to illustrate the reversibility of the lithium ion insertion and the possibility of reversion to the lithium deficient Mn_2O_4 or λ-MnO_2, lithium ions have been leached out again from the lithiated sample I-1 using the procedure used to prepare λ-MnO_2 from $LiMn_2O_4$, as described in Chapter 4.

6.3.1 Experimental

5 g of sample I-1 was placed in a beaker containing 200 ml of water. A solution of dilute acid (2M H_2SO_4) was added with stirring, while monitoring the pH changes. The stirring was continued for about 45 minutes or until the pH settled at one value. The solution was decanted and the solid washed with five 100 ml portions of distilled water. The solid was then isolated by filtration and dried in air at 90 °C.

6.3.2 Results and Discussion

The sample resulting from the acid treatment above was subjected to the same identification techniques.

X-ray diffraction confirmed the conversion of lithiated λ-MnO_2 (sample I-1) to its original state, λ-MnO_2. Figure 6.3 shows the x-ray diffraction photograph for the acid treated sample along with the diffraction patterns for $LiMn_2O_4$, λ-MnO_2 and lithiated λ-MnO_2 for comparison. As can be seen in the photograph, the x-ray diffraction lines were diffuse and fainter than those of the mother oxides. This feature could be attributed to the partial extraction of the residual amount of lithium ion in the original λ-MnO_2, remaining after its preparation from $LiMn_2O_4$. In addition to that, the sample has become less crystalline after the second acid treatment. This was exhibited by the slow rate of filtration of the sample, due to the fine particles obtained.

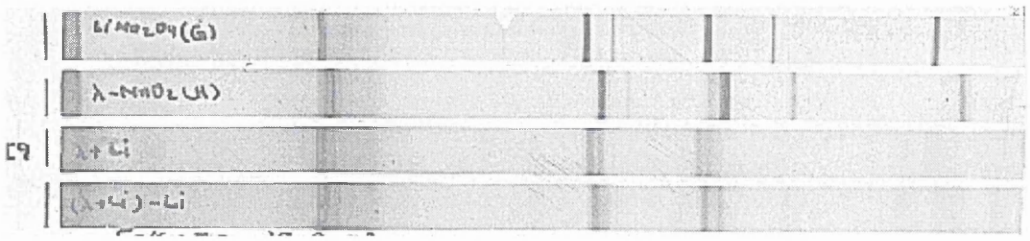

Figure 6.3 X-ray diffraction photographs of $LiMn_2O_4$, λ-MnO_2, sample I-1, and acid treated I-1.

Atomic Absorption Spectroscopy results showed that most of the lithium had been extracted out of sample I-1. The amount of lithium recorded for the acid treated sample I-1 was 0.44%, which is less than 0.5%, the amount recorded for the original λ-MnO_2.

Thermal analysis of the acid treated sample I-1 showed almost identical TG and DSC traces to those of λ-MnO_2, as can be seen in Figure 6.4. The amount of heat produced during the conversion of λ-MnO_2 to β-MnO_2 is smaller for the acid treated I-1, but it has a higher weight loss during the conversion from β-MnO_2 to Mn_2O_3. The above findings suggest a lower amount of λ-MnO_2 in the acid treated I-1 sample. Table 6.2 summarises the weight changes exhibited by both λ-MnO_2 and the acid treated sample I-1 when both were heated in air (see Figure 6.4).

Table 6.2 Thermal analysis results for acid treated I-1 sample and λ-MnO_2.

	Acid treated sample I-1	λ-MnO_2
1st change in DSC	-19.93 mcal/mg @ 270 °C	-30.16 mcal/mg @ 268 °C
2nd change in DSC	41.21 mcal/mg @ 538 °C	55.85 mcal/mg @ 537°C
3rd change in DSC	22.65 mcal/mg @ 761 °C	26.62 mcal/mg @ 759 °C
4th change in DSC	1.67 mcal/mg @ 799 °C	10.81 mcal/mg @ 813 °C
1st change in TG	8.72 % @ 512 °C	7.12 % @ 513 °C
2nd change in TG	3.53 % @ 753 °C	3.47 % @ 752 °C

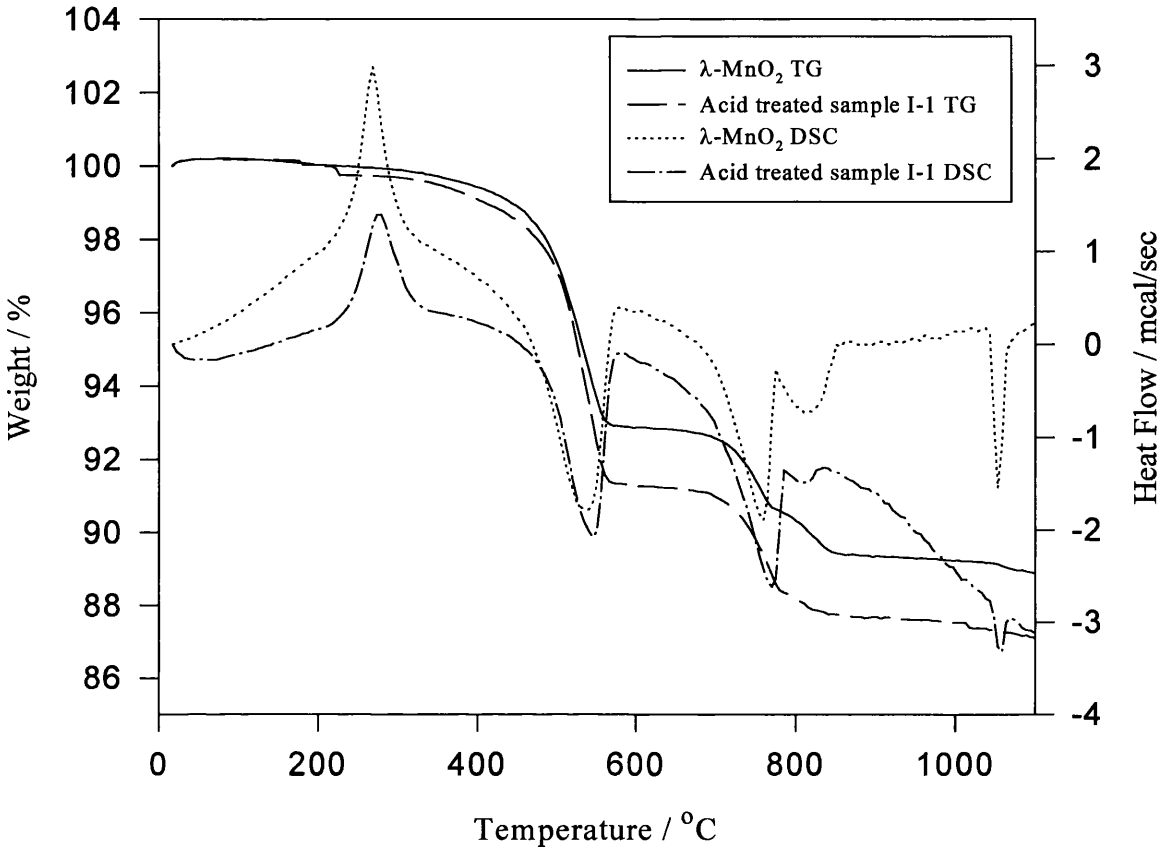

Figure 6.4 Thermal analysis results for acid treated I-1 and λ-MnO_2.

From the results shown in Table 6.2 and the x-ray diffraction patterns, it can be concluded that when a chemically lithiated sample of λ-MnO_2, e.g. sample I-1, is treated with a mild acid solution, lithium ions are extracted and the sample is returned to its original state, indicating a reversible chemical extraction/insertion reaction for the spinel manganese oxides.

6.4 Lithium Ion Insertion at 20 °C with no $MnCl_2$

In order to clarify the role of Mn^{2+} ions in the insertion reaction, the insertion reaction at 20 °C described in Section 6.1 above was repeated without the use of $MnCl_2$. The product of this experiment was designated as sample I-2.

6.4.1 Experimental

200 ml of 2M LiCl at pH 5.9 was placed in 400 ml beaker and about 1 g of powdered λ-MnO_2 was added to the solution. The addition of the oxide caused the pH to drop to about 3 in 30 minutes of stirring at room temperature. The pH of the solution was adjusted to about 6 by adding a drop of 2M LiOH. The pH dropped to about 5 in 60 minutes of stirring. The solution pH was adjusted four times in a total reaction time of 24 hours and the last pH value recorded was 3. The sample was collected by filtration using a Gooch crucible and dried at 100 °C.

6.4.2 Results and Discussion

An 18% loss from the original weight was observed after sample I-2 was filtered and dried at 100 °C. The amount of lithium found using Atomic Absorption Spectroscopy was negligible (0.56%) when compared with that found in sample I-1 (3.61%). Therefore, no significant amount of lithium has been introduced into the spinel λ-MnO_2 as a result of the reaction.

The x-ray photograph of sample I-2 shows that the x-ray diffraction pattern of λ-MnO_2 has not changed after the treatment of λ-MnO_2 with LiCl only. The x-ray diffraction pattern of the product is identical to that of λ-MnO_2 but with more diffuse lines. This diffusion of the lines could be attributed to the weight loss hence lowering the degree of crystallinity during the acid treatment of λ-MnO_2 with LiCl. Figure 6.5 shows the x-ray diffraction pattern of the treated λ-MnO_2 along with the original λ-MnO_2 and $LiMn_2O_4$ for comparison. The d-values/Å obtained from the x-ray photograph are listed in Table 6.3.

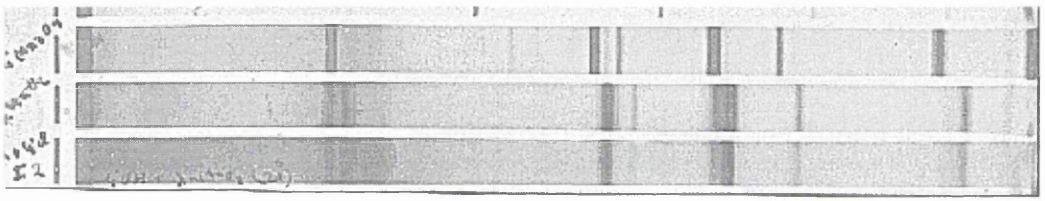

Figure 6.5 X-ray diffraction patterns of $LiMn_2O_4$, λ-MnO_2 and sample I-2.

Table 6.3 d-values/Å of $LiMn_2O_4$, λ-MnO_2 and sample I-2.

hkl	d-values/Å $LiMn_2O_4$	d-values/Å λ-MnO_2	d-values/Å sample I-2
111	4.763	4.663	4.668
311	2.483	2.427	2.439
222	2.375	2.328	2.339
400	2.075	2.027	2.027
331	1.895	1.833	1.857
333	1.585	1.550	1.561
440	1.460	1.425	-

Thermal analysis of sample I-2 gave traces identical to those of λ-MnO_2, as can be seen in Figure 6.6. The exothermic peak at ~250 °C for sample I-2 is slightly smaller than that for the original λ-MnO_2. Since the exothermic peak in the DSC trace is a diagnostic of the presence of λ-MnO_2, it can be concluded that λ-MnO_2 did not change during the course of the reaction.

From the above results, it is clear that manganese chloride is a vital factor in the lithium ion insertion reaction at room temperature.

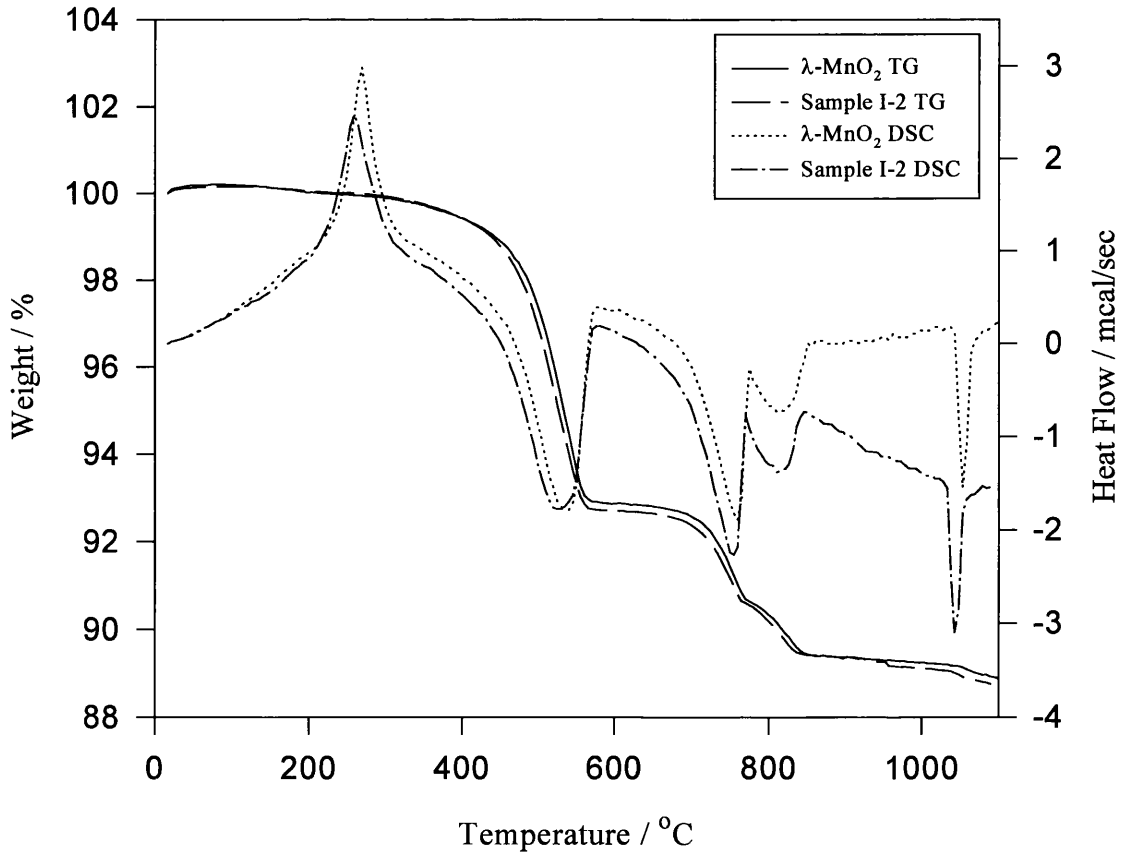

Figure 6.6 Thermal analysis results of sample I-2 and λ-MnO_2.

6.5 Lithium Ion Insertion at 80°C with no $MnCl_2$

The experiment described Section 6.4 has been performed at 80 °C to reveal the effect of temperature on lithium insertion into λ-MnO_2 in the absence of $MnCl_2$. The product of this experiment was designated as sample I-3.

6.5.1 Experimental

200 ml of 2M LiCl with pH about 5 was placed in a 400 ml beaker, and about 1 g of powdered λ-MnO_2 was added to the solution. The addition of the oxide caused the pH to drop to about 3 at room temperature. The temperature of the reaction was increased gradually to 80 °C using a temperature controlled water bath to within ±0.05 °C. The pH of the solution decreased, as the temperature of the solution increased, to settle at 2.2 at 80 °C. After the solution reached 80 °C, the pH was adjusted to about 6 using drops of 2M LiOH. The pH dropped to about 5 in 60 minutes of stirring. The solution pH was adjusted four times in a total reaction time of 24 hours. The solid then filtered off and dried at 100 °C.

6.5.2 Results and Discussion

A weight loss of 3.3% was observed as a result of the reaction, a percentage, which is different from the 18% recorded for the same reaction at room temperature (Section 6.5.1). This indicates a positive effect of higher temperature on reducing the amount of weight loss during the insertion of lithium ions into λ-MnO_2 at 80 °C in the absence of $MnCl_2$.

The lithium concentration in the sample I-3 was determined using Atomic Absorption Spectroscopy, and found to be 1.43%. This amount of lithium in sample I-3 is still low compared to the 3.61% and 3.84% found in sample I-1 and $LiMn_2O_4$ respectively.

The x-ray diffraction pattern of sample I-3 revealed a partial shift of the diffraction lines from the λ-MnO_2 positions towards the $LiMn_2O_4$ positions (see Figure 6.7). This behaviour indicates a tendency of lithium ions to intercalate the empty spaces of spinel λ-MnO_2 at higher temperatures, without manganese chloride. It is clear from the x-ray diffraction pattern photograph that some lithium has been introduced near the surface of the oxide sample λ-MnO_2 at high temperature, leaving the inside of the sample unchanged. This could explain the low percentage (1.43%) of lithium found in sample I-3. Table 6.4 lists the d-values/Å obtained from the photograph shown in Figure 6.7.

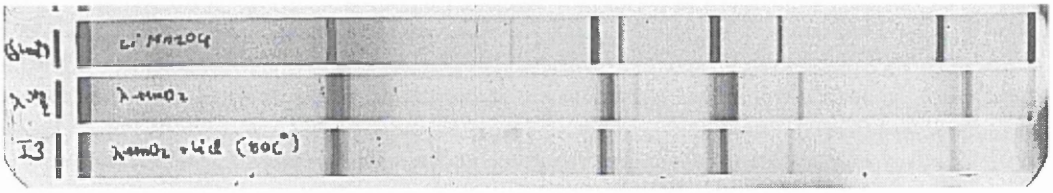

Figure 6.7 X-ray diffraction patterns of $LiMn_2O_4$, λ-MnO_2 and sample I-3.

Thermal analysis (Figure 6.8) showed a reduction in the size of the exothermic peak on the DSC trace for sample I-3 when compared with λ-MnO_2. This peak corresponds to the conversion of λ-MnO_2 to β-MnO_2. The reduction of the amount of heat produced during this process, from -27.86 mcal mg^{-1} to -17.41 mcal mg^{-1}, indicates a reduction in

the amount of spinel λ-MnO_2, as a result of the introduction of lithium into the sample. The drop in the weight lost during the heating of the sample to about 500 °C, from 7.12% to 5.53%, confirms this interpretation. However, the characteristics of the TG trace shown in Figure 6.8 do not resemble the behaviour of $LiMn_2O_4$ but are like that of λ-MnO_2 with minor differences.

Table 6.4 d-values/Å of $LiMn_2O_4$, λ-MnO_2 and sample I-3.

hkl	d-values/Å $LiMn_2O_4$	d-values/Å λ-MnO_2	d-values/Å sample I-3
111	4.763	4.663	4.733
311	2.483	2.427	2.471
222	2.375	2.328	2.370
400	2.075	2.027	2.037
331	1.895	1.833	1.872
333	1.585	1.550	1.572
440	1.460	1.425	-

From the above results, it can be concluded that increasing the reaction temperature has a partial positive effect on lithium insertion into λ-MnO_2, despite the absence of manganese chloride, which is essential for the lithium insertion reaction at room temperature. The of higher reaction temperature could have enhanced the ion-sieve

properties of λ-MnO_2, leading to the increase in the amount of lithium found in sample I-3. The effect of increasing the temperature of the lithium insertion reaction in the presence of manganese chloride was therefore examined.

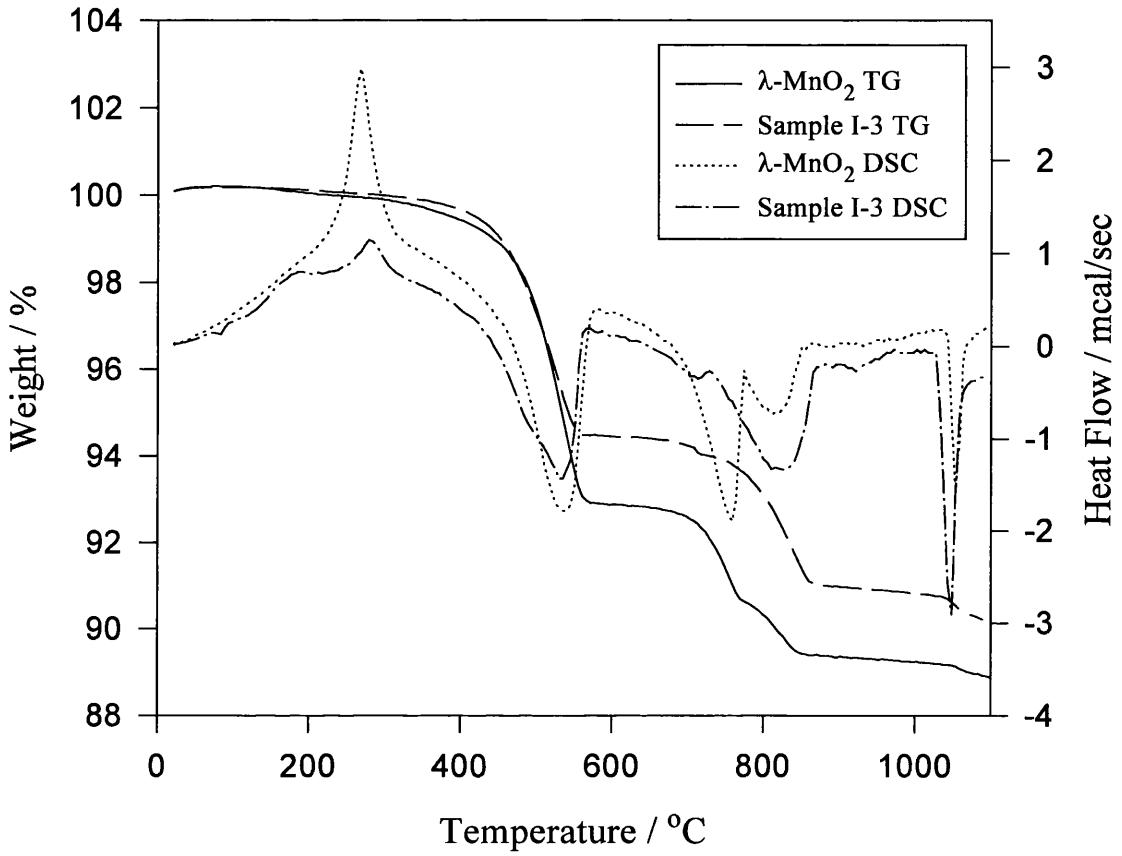

Figure 6.8 Thermal analysis results for sample I-3 and λ-MnO_2.

6.6 Lithium Ion Insertion at 80 °C with $MnCl_2$

In the previous section, a partial positive effect of high temperature on lithium uptake by λ-MnO_2 in the absence of manganese chloride was noted. This section examines the effect of high temperature on the insertion reaction of lithium ions in the presence of manganese chloride. The product of this experiment was designated sample I-4.

6.6.1 Experimental

100 ml of 2M $MnCl_2.4H_2O$ and a 100 ml of 2M LiCl were mixed together in a 400 ml beaker. The mixture had a pH of about 5. The temperature of the reaction was raised to 80 °C using a temperature controlled water bath to within ±0.05 °C. The pH of the solution at this temperature was about 3. 1 g of powdered λ-MnO_2 was added to the chloride mixture causing the pH to drop to about 0.3. The pH of the solution was adjusted with a drop of 2M LiOH to about 5. The solution pH droped to about 3 in one hour's time, and to about 2 in two hour's time. The pH of the solution was adjusted to about 5 for second time. The black suspension changed to a thick brown suspension which was then allowed to cool to room temperature. The brown solid precipitate was collected by filtration, washed several times with distilled water, and dried at 100 °C. The brown colour remained unchanged during the washing procedure.

6.6.2 Results and Discussion

Despite the unusual nature of sample I-4, it was subjected to the same identification techniques used for other samples.

X-ray diffraction revealed the formation of a new and unknown product along with some unchanged λ-MnO_2, which can be easily identified in the x-ray photograph, shown in Figure 6.9.

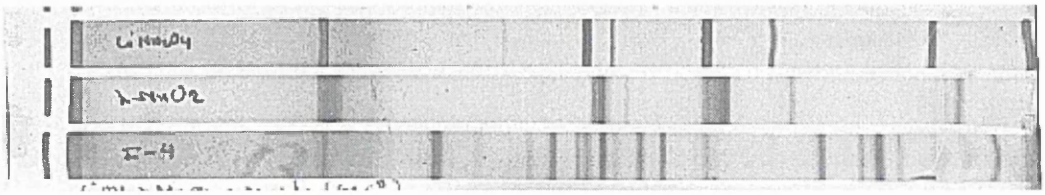

Figure 6.9 X-ray diffraction patterns of $LiMn_2O_4$, λ-MnO_2 and sample I-4.

d-values/Å for sample I-4 are listed in Table 5.5 along with their corresponding intensities. The values indicated with (*) are believed to belong to the spinel λ-MnO_2.

Thermogravimetric analysis revealed that sample I-4 exhibits totally different behaviour from that of λ-MnO_2 when it is heated up to 1000 °C (Figure 5.10). Sample I-4 suffers a weight loss of about 7.23% at about 288 °C accompanied by a large endothermic peak shown on the DSC trace. This large endothermic peak would obscure any possible exothermic peak resulting from the conversion of λ-MnO_2 to β-MnO_2, since both

reactions take place at about the same temperature. The second weight loss for sample I-4 of ~1.7% takes place at ~540 °C. This weight loss might be an indication of the presence of some MnO_2, as it is similar to that corresponding to the conversion of MnO_2 to Mn_2O_3 in the λ-MnO_2 TG trace.

Table 6.5 d-values/Å and their intensities for sample I-4. Those marked with (*) are believed to be due to residual λ-MnO_2.

d-values/Å	Intensity	d-values/Å	Intensity
4.75*	50	2.19	30
3.41	100	2.07*	10
2.77	10	1.790	30
2.64	30	1.710	20
2.53	20	1.678	50
2.49*	20	1.640	10
2.42*	50	1.500	20
2.28	50		

From the evidence above, it can be concluded that reacting λ-MnO_2 with manganese chloride, lithium chloride and lithium hydroxide at 80 °C produced an unknown brown powder, which has different characteristics from those expected of λ-MnO_2 or $LiMn_2O_4$. No further attempts were made to identify sample I-4 and its formation is thought to be the result of the catalytic properties of λ-MnO_2 at high temperature.

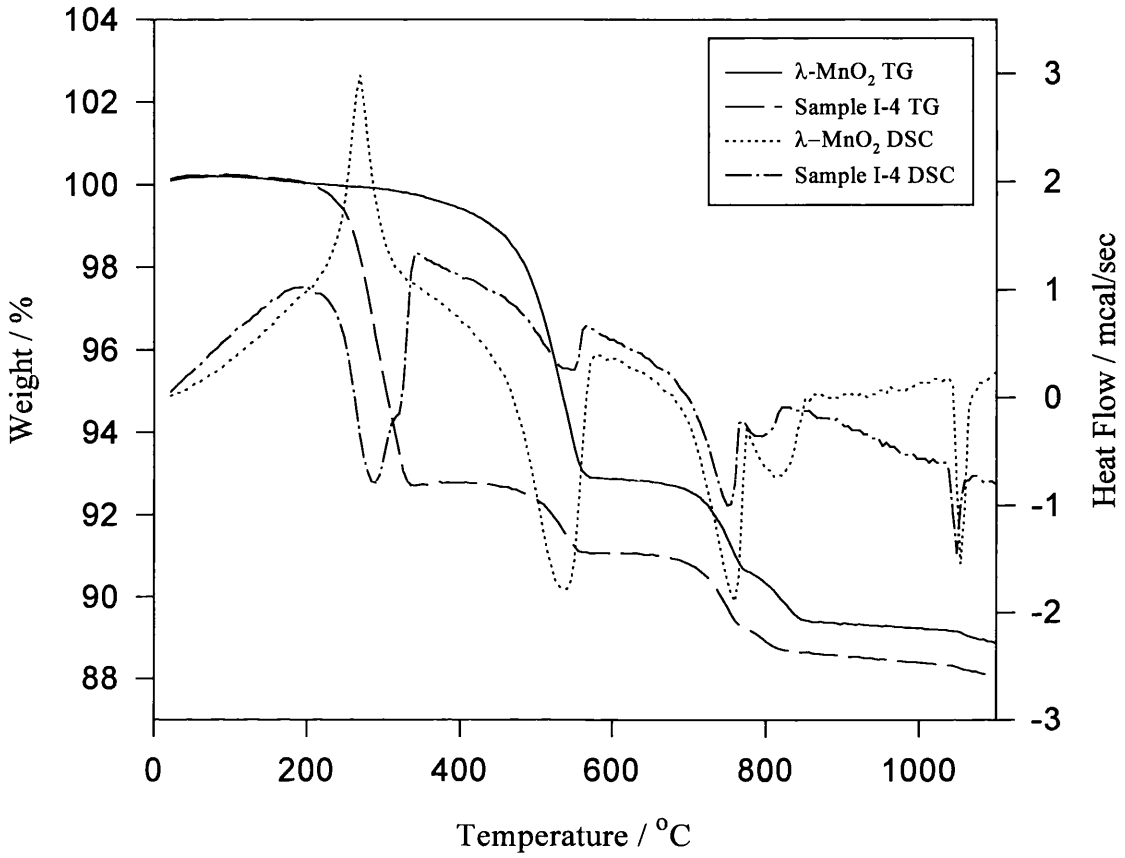

Figure 6.10 Thermal analysis results for sample I-4 and λ-MnO_2.

6.7 Lithium Ion Insertion at 50 °C with $MnCl_2$

The reaction in the previous section was carried out at 80 °C and yielded an undesirable product. To clarify the role of the temperature in the behaviour of the reaction, the procedure in the previous section was carried out at 50 °C. The product of the reaction was designated sample I-5.

6.7.1 Experimental

100 ml of 2M $MnCl_2.4H_2O$ and a 100 ml of 2M LiCl were mixed together in a 400 ml beaker. The mixture had a pH of about 5. The temperature of the reaction was raised to 50 °C using a temperature controlled water bath to within ±0.05 °C. 1 g of powdered λ-MnO_2 was added to the chloride mixture causing the pH to drop to about 1.5. The pH of the solution was adjusted to 4 four times using 2M lithium hydroxide. A trace of brown colour was observed at the end of the reaction. This colour was removed by washing the solid sample by the decantation method. The sample was then collected by filtration and dried at 100 °C.

6.7.2 Results and Discussion

The x-ray diffraction photograph of the sample I-5 is shown in Figure 6.11. The diffraction pattern of sample I-5 reveals a few differences when it is compared with that of λ-MnO_2, $LiMn_2O_4$ and sample I-4. All the new lines that were observed in sample I-4 has disappeared, except a weak line at 3.41 Å, which corresponds to the strongest line found in the I-4 diffraction pattern. This line suggests that the washing procedure was

not enough to get rid of all the impurities, despite the fact that the entire brown colour had disappeared.

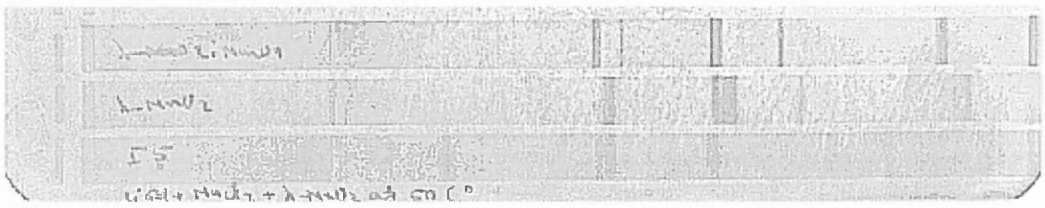

Figure 6.11 X-ray diffraction patterns of $LiMn_2O_4$, λ-MnO_2 and sample I-5.

The other interesting observation is that some of the lines have shifted back to the $LiMn_2O_4$ diffraction positions, leaving the rest of the diffraction lines the same as those for λ-MnO_2. Bragg reflection 400 did not shift a higher d-value, suggesting no change from the unit cell of λ-MnO_2 as a result of the reaction, at least in the 400 plane.

Figure 6.12 shows the TG trace resulting from heating sample I-5 up to 1000 °C, along with those for $LiMn_2O_4$ and λ-MnO_2. Sample I-5 exhibits totally different behaviour from that of sample I-4. It shows a smaller weight loss of 2.61% at about 200 °C, and a bigger weight loss of 4.21% at about 500 °C, when compared with sample I-4. This illustrates that sample I-5 has less impurity than sample I-4.

The second weight loss of 4.21% in the TG trace of Sample I-5 suggests that it has a closer relationship to the original sample of λ-MnO_2. It is clear from the evidence above

that the insertion reaction of lithium ions at 50 °C in the presence of manganese chloride does not proceed to form the lithiated manganese oxide or $LiMn_2O_4$.

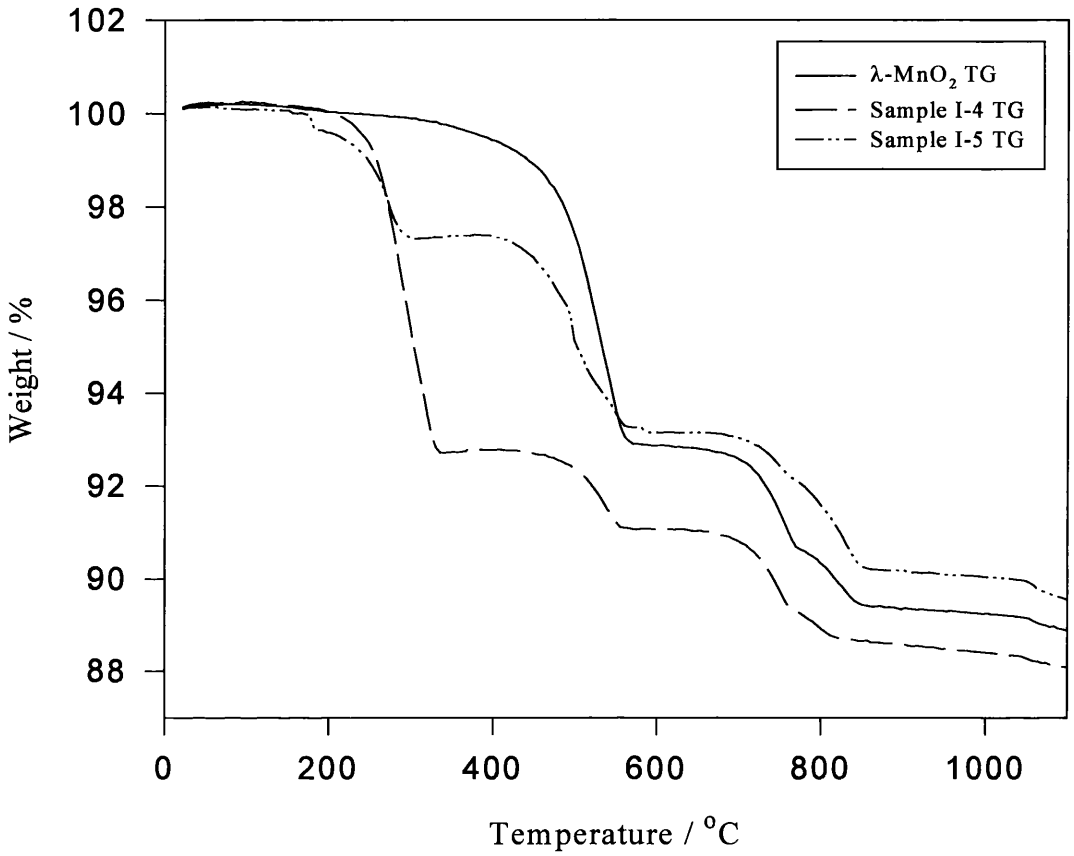

Figure 6.12 Thermal analysis results for samples I-4, I-5 and λ-MnO_2.

From this experiment, it can be concluded that higher reaction temperature has a negative effect on the insertion reaction of lithium ions into λ-MnO_2 in the presence of manganese chloride and lithium chloride. The increase in temperature led to the formation of an unknown product, while λ-MnO_2 preserved its crystal structure.

6.8 Lithium Ion Insertion at 2 °C Using $MnCl_2$

In the previous two sections, the effect of higher temperature on the insertion reaction of lithium into λ-MnO_2 was examined. In this section, the effect of lower temperature on the same reaction will be discussed. The lithium insertion reaction used a mixture of lithium chloride and manganese chloride, with lithium hydroxide as the pH controller. The product of this experiment was designated sample I-6.

6.8.1 Experimental

100 ml of 2M $MnCl_2.4H_2O$ and a 100 ml of 2M LiCl were mixed together in a 400 ml beaker. The temperature of the reaction was brought down to 2 °C using a cooling coil placed in a temperature controlled water bath to within ±0.05 °C. The chloride mixture was placed in the water bath overnight in order to reach the desired reaction temperature. The mixture at this temperature had a pH of about 5. 1 g of powdered λ-MnO_2 was added to the chloride mixture causing the pH to drop to about 2. The pH of the solution was adjusted with a drop of 2M LiOH to about 5. The lithium hydroxide and powdered λ-MnO_2 were also kept at the reaction temperature, 2 °C. The solution was kept stirring, and the pH started to drop and needed to be adjusted again to about 5. No change in the solution pH reading was observed after the second adjustment, although the solution was stirred for 24 hours. The solid precipitate was collected by filtration using a Gosh crucible and dried at 100 °C.

6.8.2 Results and Discussion

A weight gain of about 20% of the original sample weight was obtained. The increase in weight suggests a possible lithium intercalation into λ-MnO_2. The lithium ion concentration was determined using Atomic Absorption Spectroscopy, and found to be 3.48%, which is in good agreement with the theoretical lithium concentration in $LiMn_2O_4$ (3.84%) and with the amount of lithium in the original $LiMn_2O_4$ prepared in this work (3.73%).

Sample I-6 has been examined by x-ray diffraction and the result is shown in Figure 6.13. The corresponding d-values/Å of the reflections shown in Figure 6.13 are listed in Table 6.6.

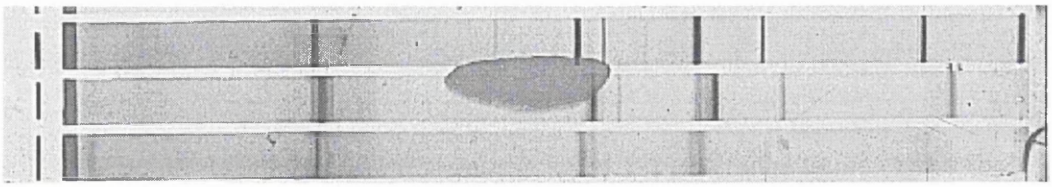

Figure 6.13 X-ray diffraction patterns of $LiMn_2O_4$, λ-MnO_2 and sample I-6.

The x-ray diffraction pattern of sample I-6 shows the shift of the main lines towards those of the original $LiMn_2O_4$ as a result of lithium insertion into the spinel λ-MnO_2. The intensity of the lines has reduced indicating an incomplete lithium insertion. This suggestion is confirmed by the appearance of Bragg reflection 311, which belongs to the spinel λ-MnO_2.

Table 6.6 d-values/Å of $LiMn_2O_4$, λ-MnO_2 and sample I-6.

hkl	d-values/Å $LiMn_2O_4$	d-values/Å λ-MnO_2	d-values/Å sample I-6
111	4.763	4.663	4.689
311	2.483	2.427	2.478
222	2.375	2.328	2.379
400	2.075	2.027	2.050
331	1.895	1.833	1.886
333	1.585	1.550	1.587
440	1.460	1.425	-

Figure 6.14 shows TG traces for sample I-6, sample I-1, λ-MnO_2 and $LiMn_2O_4$. The TG trace for the lithium-inserted sample at 2 °C (sample I-6) shows more affinity with that for λ-MnO_2, than does the TG trace for sample I-1. Sample I-1 is the lithium-inserted λ-MnO_2 at room temperature described in Section 6.1.

Table 6.7 lists the weight percentages on the curves shown in Figure 6.14 at the selected temperatures. It is clear from the table that the use of temperature of 2 °C has a small negative effect on the amount of lithium inserted into λ-MnO_2. It appears that the insertion reaction is best performed at around room temperature. Furthermore, lowering the reaction temperature has lessened the x-ray reflection intensity, an effect not observed when the reaction was done at room temperature, sample I-1.

Table 6.7 Weight percentage of sample I-1, I-6, λ-MnO_2.and $LiMn_2O_4$ at selected temperatures.

	$LiMn_2O_4$	Sample I-1	Sample I-6	λ-MnO_2
300 °C	100.00	98.316	98.577	99.887
600 °C	100.00	95.252	94.837	92.879
900 °C	95.085	91.278	90.449	89.372
1100 °C	94.020	90.400	89.280	88.900

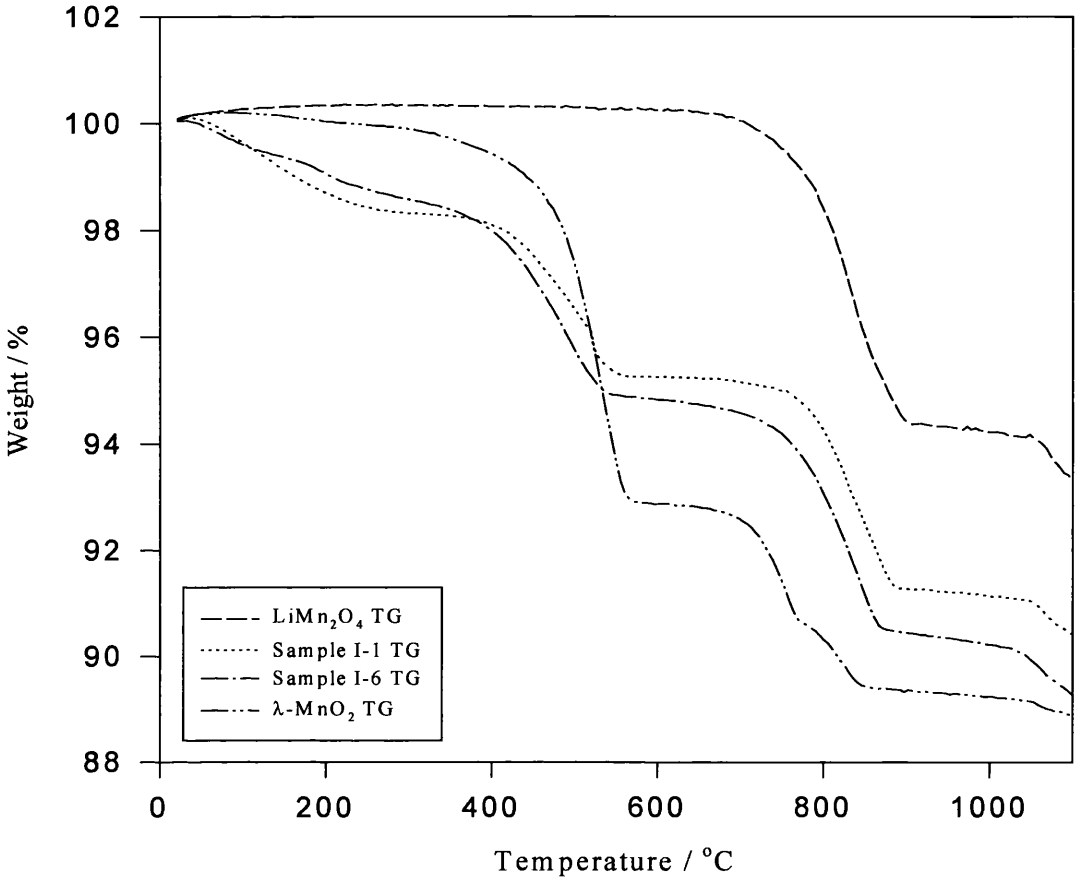

Figure 6.14 Thermal analysis results for sample I-1, I-6, λ-MnO_2.and $LiMn_2O_4$.

6.9 Lithium Ion Insertion at 20 °C With Longer Reaction Time

In the previous sections, it was concluded that the lithium insertion reaction using lithium and manganese chlorides is best carried out at around room temperature. The experiments involved a total reaction time of 24 hours. In this section, the effect of a longer reaction time on the outcome of the reaction will be examined. The product of this reaction is designated sample I-7.

6.9.1 Experimental

100 ml of 2M $MnCl_2.4H_2O$ and 100 ml of 2M LiCl were mixed together in a 400 ml beaker. The mixture had a pH of about 4.5. The temperature of the reaction was set to room temperature (20 °C) using a temperature controlled water bath to within ±0.05 °C. 1 g of powdered λ-MnO_2 was added to the chloride mixture causing the pH to drop to about 2. The pH of the solution was adjusted with a drop of 2M LiOH to about 5. The solution was kept stirred for the whole course of the reaction. The solution pH also started to drop and needed to be adjusted four times over a period of 48 hours to settle on a constant value of 3.4. The solid precipitate was collected by filtration using a Gooch crucible and dried at 100 °C.

6.9.2 Results and Discussion

Sample I-7 showed an increase in weight of about 17% compared to the starting material, which could be attributed to lithium and manganese uptake by λ-MnO_2, and to

the surface and molecular water attached to the crystals despite the drying procedure at 100 °C.

Lithium concentration in the lithiated sample was determined using Atomic Absorption Spectroscopy, as described in Chapter 2, and found to be 3.69%. The amount of lithium found in sample I-7 is in good agreement with the theoretical lithium concentration in $LiMn_2O_4$ (3.84%) and with the lithium concentration in $LiMn_2O_4$ prepared in this work (3.73%). It is higher than the percentage recorded for sample I-1. This is an indication of the positive effect of longer reaction time on the amount of lithium inserted into λ-MnO_2.

Sample I-7 had a very similar x-ray diffraction pattern to that of $LiMn_2O_4$ and sample I-1, as can be seen in Figure 6.15. The d-values/Å obtained from Figure 6.15 showed that sample I-7 has an identical lattice constant to that of $LiMn_2O_4$ (a = 2.068 Å), while sample I-1 exhibit a smaller lattice constant (a = 2.060 Å). Table 6.8 lists d-values/Å of sample I-7 along with those of sample I-1 and $LiMn_2O_4$ for comparison.

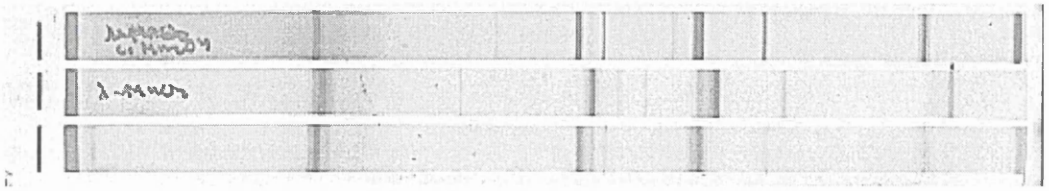

Figure 6.15 X-ray diffraction patterns of $LiMn_2O_4$, λ-MnO_2 and sample I-7.

Table 6.8 d-values/Å of $LiMn_2O_4$ sample I-1 and sample I-7.

hkl	d-values/Å $LiMn_2O_4$	d-values/Å sample I-1	d-values/Å sample I-7
111	4.763	4.732	4.750
311	2.483	2.505	2.478
222	2.375	2.394	2.378
400	2.075	2.060	2.068
331	1.895	1.883	1.892
333	1.585	1.576	1.591
440	1.460	1.454	1.462

Thermal analysis of sample I-7 shows no important differences from that of sample I-1, with the only noticeable one being a small difference in the weight percentage of about 0.219 % at about 300 °C, as can be seen in Figure 6.16. Therefore the increase in reaction time had no substantial effect on the thermal properties of the lithium-inserted λ-MnO_2.

From the above results it could be concluded that the increase in reaction time has increased the amount of lithium inserted into λ-MnO_2. Hence the x-ray diffraction pattern of the product has improved in quality and produced a lattice constant identical

to that of $LiMn_2O_4$. $LiMn_2O_4$ has therefore been obtained by inserting lithium ions into λ-MnO_2 at room temperature. The insertion of lithium was achieved using lithium chloride as the lithium ion source, manganese chloride as the manganese ion source and lithium hydroxide as the pH controller.

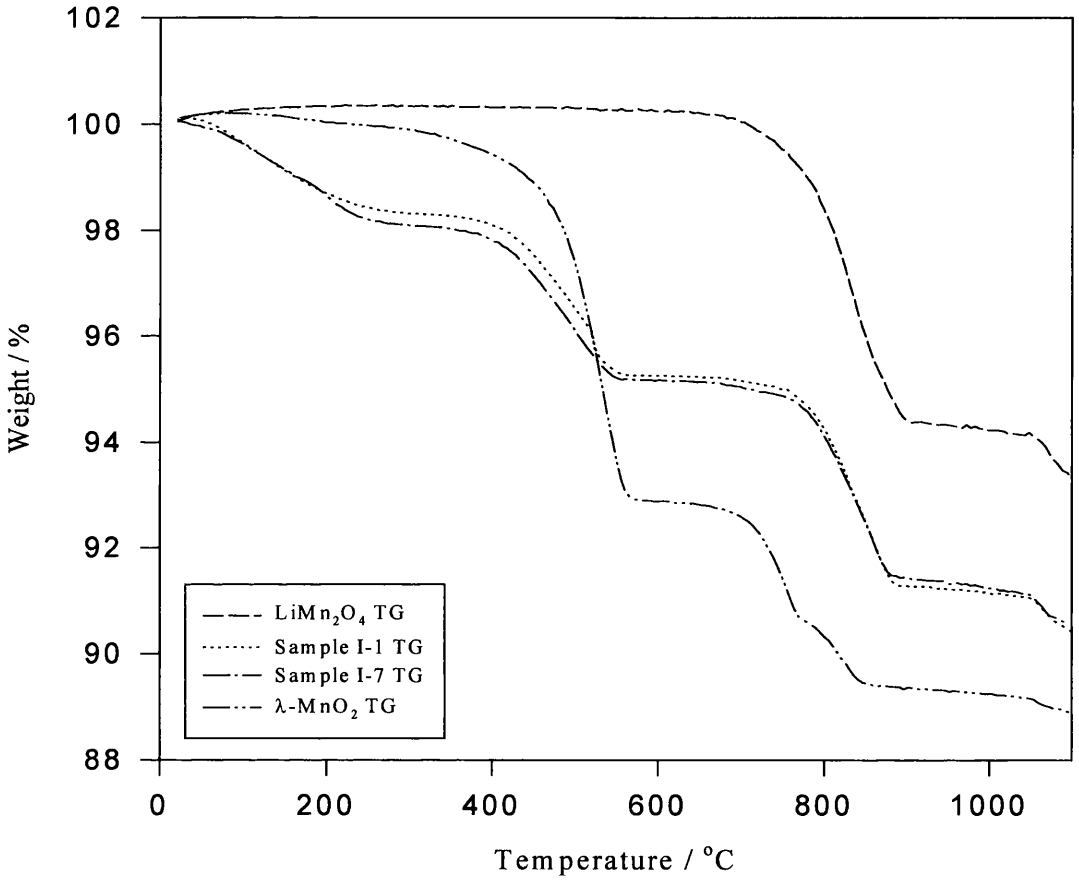

Figure 6.16 Thermal analysis results for samples I-1, I-7, λ-MnO_2.and $LiMn_2O_4$.

6.10 Conclusion

The lithium deficient λ-MnO_2 was originally prepared by extracting lithium ions from $LiMn_2O_4$ using a mildly acidic solution. The extraction of lithium ions is thought to leave the spinel structure intact and lithium ions can be reversibly introduced back to form $LiMn_2O_4$. For the purpose of establishing the best reaction conditions, λ-MnO_2 was reacted with LiCl as the source of lithium ion, $MnCl_2$ as the source of the additional manganese when needed, and LiOH as a pH controller. The reaction was carried out at various temperatures and for various lengths of time.

The results obtained from the insertion reactions of lithium into λ-MnO_2, i.e. the d-values/Å obtained from x-ray diffraction photographs, and lithium concentrations, are summarised in Table 6.9.

Samples have been arranged to show their position in terms of d-values/Å and lithium percentages in relation to the end members of the series, λ-MnO_2 and $LiMn_2O_4$. It is clear from Table 6.9 that sample I-7 is the closest one to $LiMn_2O_4$. Therefore lithium-inserted sample I-7 is believed to have the spinel structure $LiMn_2O_4$ which has been achieved through the chemical insertion of lithium into spinel λ-MnO_2.

So it can be concluded that the chemical extraction of lithium from $LiMn_2O_4$ has been reversed chemically at room temperature.

Table 6.9 d-values/Å and lithium concentrations for the lithium inserted samples, λ-MnO_2 and $LiMn_2O_4$.

d-values /Å hkl	λ-MnO_2	Sample I-2	Sample I-3	Sample I-6	Sample I-1	Sample I-7	$LiMn_2O_4$
111	4.662	4.668	4.733	4.689	4.732	4.750	4.763
311	2.427	2.439	2.471	2.478	2.505	2.478	2.483
222	2.328	2.339	2.370	2.379	2.394	2.378	2.375
400	2.027	2.027	2.037	2.050	2.060	2.068	2.075
331	1.833	1.857	1.872	1.886	1.883	1.892	1.895
333	1.550	1.561	1.572	1.587	1.576	1.591	1.585
440	1.425	-	-	-	1.454	1.462	1.460
% Li	0.5	0.6	1.4	3.5	3.6	3.7	3.8

The reaction requires lithium and manganese chlorides as lithium and manganese sources respectively and lithium hydroxide as the pH controller. The reaction pH needed to be adjusted four times in a total reaction time of 48 hours. The reactants were kept stirred during the course of the reaction and at a constant room temperature. The product of the insertion reaction shows characteristics, which can be identified as those of $LiMn_2O_4$, and the reversible reaction would be written as below.

$$2LiMn_2O_4 + 4H^+ \Leftrightarrow 3\lambda - MnO_2 + 2Li^+ + Mn^{2+} + 2H_2O$$

References

1 K. Ooi, Y. Miyai, S. Katoh, H. Maeda, and M. Abe, *Bull. Chem. Soc. Jpn.*, **61**, 407 (1988).

2 K. Ooi, Y. Miyai, S. Katoh, H. Maeda, and M. Abe, *Chem. Lett.*, 989 (1988).

3 K. Ooi, Y. Miyai, and J. Sakakihara, *Langmuir*, **7**, 1167 (1991).

4 K. Ooi, Y. Miyai, S. Katoh, H. Maeda, and M. Abe, *Langmuir* **5**, 150 (1989).

5 Q. Feng, Y. Miyai, H. Kano, and K. Ooi, *Langmuir*, **8**, 1861 (1992).

6 J. Hunter, *J. Solid State Chem.*, **39**, 142 (1981).

Preparation of Other Members of the Li-Mn-O System

7.1 Introduction

During the thermal stability studies of the spinel $LiMn_2O_4$, other members of the Li-Mn-O oxide system were formed, e.g. $Li_2Mn_4O_7$ and $LiMn_2O_3$. These oxides were formed when the precursors were mixed at a molar ratio of 1:2 and heated in an inert atmosphere, in this case nitrogen. The reaction progress was followed using the Stanton Redcroft TG-DSC simultaneous thermal analyser STA625. The procedure above proved to be successful in testing the viability of the preparation method prior to its scale up operation.

Figure 7.1 shows part of the Li-Mn-O system (See Figure 1.4). Figure 7.1 shows the positions of lithium manganese oxides that are of interest to battery applications [1].

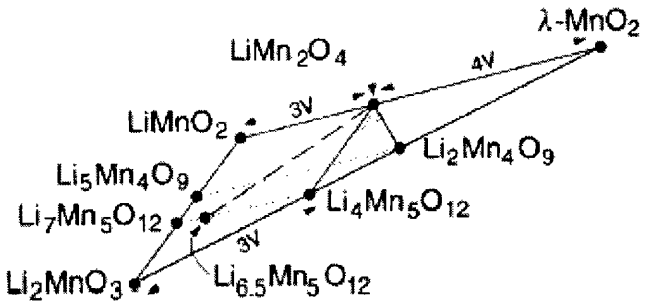

Figure 7.1 Part of the Li-Mn-O system [1].

In order to obtain some of these oxides, a series of reactions using various ratios of Li_2CO_3 and Mn_2O_3 in nitrogen and in air was attempted. Table 7.1 summaries the various ratios suggested along with their theoretical products when reacted in nitrogen and air.

Table 7.1 The possible products of reacting various ratios of Li:Mn in nitrogen and air.

Ratio Li:Mn	Reaction possible product in N_2 and air
1:1	$2LiMnO_2 \xleftarrow{N_2,\Delta} Li_2CO_3 + Mn_2O_3 \xrightarrow{Air,\Delta} Li_2Mn_2O_5$
1:2	$Li_2Mn_4O_7 \xleftarrow{N_2,\Delta} Li_2CO_3 + 2Mn_2O_3 \xrightarrow{Air,\Delta} 2LiMn_2O_4$
1:3	$2LiMn_3O_5 \xleftarrow{N_2,\Delta} Li_2CO_3 + 3Mn_2O_3 \xrightarrow{Air,\Delta} Li_2Mn_6O_{11}$
1:4	$Li_2Mn_8O_{13} \xleftarrow{N_2,\Delta} Li_2CO_3 + 4Mn_2O_3 \xrightarrow{Air,\Delta} Li_2Mn_4O_7$
2:1	$Li_4Mn_2O_5 \xleftarrow{N_2,\Delta} 2Li_2CO_3 + Mn_2O_3 \xrightarrow{Air,\Delta} 2Li_2MnO_3$
3:1	$2Li_3MnO_3 \xleftarrow{N_2,\Delta} 3Li_2CO_3 + Mn_2O_3 \xrightarrow{Air,\Delta} Li_6Mn_2O_7$
2:3	$Li_4Mn_6O_{11} \xleftarrow{N_2,\Delta} 2Li_2CO_3 + 3Mn_2O_3 \xrightarrow{Air,\Delta} 2Li_2Mn_3O_6$
3:2	$Li_6Mn_4O_9 \xleftarrow{N_2,\Delta} 3Li_2CO_3 + 2Mn_2O_3 \xrightarrow{Air,\Delta} 2Li_3Mn_2O_5$

The products of reacting Li_2CO_3 and Mn_2O_3 in a ratio of 1:2 were discussed in Section 3.2.1, as this method was used to prepare $LiMn_2O_4$.

Reacting Li_2CO_3 and Mn_2O_3 in a 1:1 Li:Mn ratio should produce one of the other alternative cathode materials that have been widely investigated, $LiMnO_2$ or lithium rich $LiMn_2O_4$ ($Li_2Mn_2O_4$). The lithiated spinel $Li_2Mn_2O_4$ has a rock salt stoichiometry and tetragonal symmetry, $I4_1/amd$ (or $F4_1/ddm$) [2], while orthorhombic $LiMnO_2$ has

symmetry Pmmn [3]. These compounds are electrochemically different in terms of usefulness as electrode materials. The lithiated spinel $Li_2Mn_2O_4$ has been well characterized as a good cathode material for lithium batteries [4]. On the other hand, the electrochemical activity of $LiMnO_2$ is dependent on the reaction conditions [3, 5, 6].

Orthorhomic $LiMnO_2$ is usually prepared by reacting $LiMn_2O_4$ with LiOH between 300-400 °C under a constant flow of hydrogen. The reaction proceeds according to Equation 7.1.

$$LiMn_2O_4 + LiOH.H_2O + 0.5H_2 \xrightarrow{300-400\ ^\circ C} 2LiMnO_2 + 2H_2O \qquad 7.1$$

In practice, it is not easy to control the formation of single phase $Li_2Mn_2O_4$ or $LiMnO_2$ as some of the product will react with hydrogen to produce multiphase mixtures of $LiMn_2O_4$ and either MnO or Li_2MnO_3, according to Equation 7.2 [3].

$$Li_2Mn_2O_4 + H_2 \longrightarrow 2MnO + 2LiOH \qquad 7.2$$

Another preparation method was suggested by Barboux *et al.* [7]. They tried to prepare the tetragonal $Li_2Mn_2O_4$ from manganese acetate and lithium acetate by heating the reagents at 400 °C at low oxygen pressure in argon. They also reported the presence of multiphase mixtures that contain the electrochemically inactive phase of MnO.

Gummow *et al.* [6] proposed a method for the synthesis of orthorhombic $LiMnO_2$ at moderate temperature in an inert atmosphere. The oxide was synthesised by reacting γ-

MnO_2 (CMD) with LiOH using carbon black in an argon atmosphere according to Equation 7.3.

$$MnO_2 + LiOH.H_2O + 0.25C \xrightarrow{600\ ^\circ C, Ar} LiMnO_2 + 0.25CO_2 + 1.5H_2O \qquad 7.3$$

They reported a single phase orthorhombic $LiMnO_2$ which had a rechargeable capacity of 160 mA h g^{-1}.

In this work, the preparation of $LiMnO_2$ was attempted the reaction of stoichiometric amounts of Li_2CO_3 and Mn_2O_3 in nitrogen. The proposed reaction in nitrogen should follow Equation 7.4.

$$Li_2CO_3 + Mn_2O_3 \xrightarrow{N_2, \Delta} 2LiMnO_2 \text{ or } Li_2Mn_2O_4 + CO_2 \qquad 7.4$$

7.2 Preparation Method with 1:1 Li:Mn Ratio

7.2.1 Experimental

Li_2CO_3 and Mn_2O_3 were mixed thoroughly using a ball mill with steel balls in a 1:1 Li:Mn molar ratio. Cyclohexane was added to the contents of the ball mill and the mixture ground for 3 hours to form a homogeneous paste of the reactants. Cyclohexane was subsequently evaporated. Samples of the mixture were gradually heated in nitrogen and air independently, and the progress of the reactions was recorded on the Stanton Redcroft thermal analyser. The results of those reactions are illustrated in Figure 7.2.

7.2.2 Results and discussion

Figure 7.2 shows the weight loss curves for samples heated in air and nitrogen along with values of the weight recorded at the positions indicated. Values below the curve are those for the nitrogen curve and those above the curve are for the air curve.

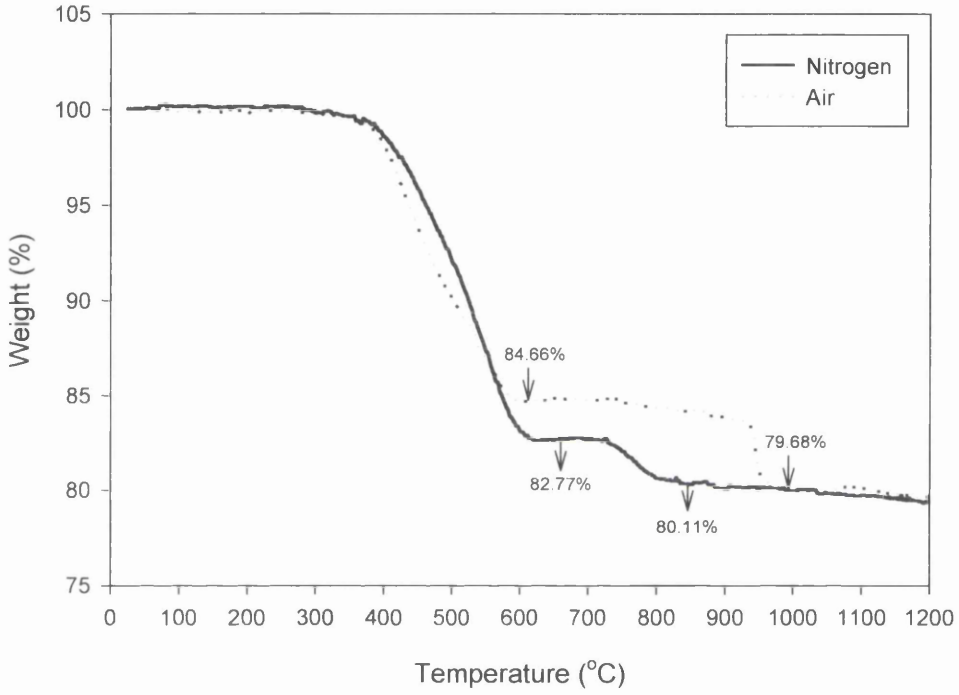

Figure 7.2 TGA traces of reacting Li_2CO_3 and Mn_2O_3 in 1:1 Li:Mn molar ratio in nitrogen and air.

For the run under nitrogen, the curve clearly shows a two-stage reaction. The first weight loss of about 17.23% happens at about 650 °C and a second weight loss of about 2.66% is complete at around 850 °C. Based on the reaction represented in Equation 7.4 the theoretical weight loss corresponding to one CO_2 is 18.98%. The total experimental

weight loss is about 19.89% indicating possible formation of the oxide $LiMnO_2$. Obviously the reaction passes through an intermediate state at about 650 °C with a weight loss of about 17.23%.

In order to identify the middle and final stages of the reaction, two samples were run under nitrogen and annealed at 650 °C and 850 °C respectively. Samples were allowed to cool to room temperature under nitrogen before examination by x-ray diffraction. Figure 7.3 shows the x-ray diffraction patterns for both samples.

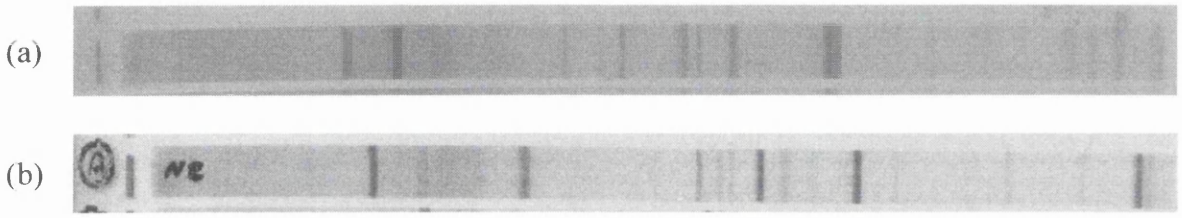

Figure 7.3 X-ray diffraction of Li_2CO_3 + Mn_2O_3 in 1:1 molar ratio heated in nitrogen, (a) at 650 °C and (b) at 850 °C.

Table 7.2 lists d-values for the diffraction patterns shown in Figure 7.3 along with those of $LiMnO_2$ taken from JCPDS file 23-361.

From the results shown in Table 7.2, we can see that the product of reacting Li_2CO_3 and Mn_2O_3 in nitrogen in 1:1 Li:Mn molar ratio is a single phase orthorhombic $LiMnO_2$ with unit cell dimensions a = 2.790 Å, b = 5.614 Å and c = 4.564 Å. Based on the above results, a larger sample of $LiMnO_2$ was prepared under an atmosphere of nitrogen using the high temperature furnace. The sample was heated to and annealed at 850 °C for one

hour before cooling to room temperature. The product was a dark brown powder that upon examination by x-ray diffraction was confirmed to be single phase orthorhombic $LiMnO_2$, similar to that produced in the Stanton Redcroft Thermal Analyser.

Table 7.2 d-values/Å for $Li_2CO_3 + Mn_2O_3$ in 1:1 molar ratio heated in nitrogen to 650 and 850 °C along with those for $LiMnO_2$

d-values 650 °C	I	d-values 850 °C	I	$LiMnO_2$ 23-361	I	hkl
5.75	5	5.75	10	5.80	10	010
4.90	1	3.55	5	3.62	7	011
4.75	10	2.52	4	2.533	2	110
4.3	1	2.44	3	2.444	1.5	021
4.10	0.5	2.39	2	2.405	1	101
3.10	2	2.28	8	2.298	6	002
2.88	1	2.20	1	2.220	3	111
2.77	4	2.13	0.5	2.130	1.5	012
2.53	1	2.01	10	2.017	7	120
2.49	5	1.91	0.5	1.923	0.5	030
2.43	4	1.81	0.5	1.773	0.5	031
2.37	1	1.69	0.5	1.697	1	112
2.32	4	1.575	1	1.586	1	130
2.03	9	1.505	8	1.510	5	122
2.01	5	1.490	3	1.495	1.5	131
1.870	0.5			1.472	0.5	013
1.800	0.5			1.438	1	040
1.642	0.5			1.401	1	200
1.575	1			1.362	0.5	210
1.545	1			1.306	1	113
1.515	1			1.233	1	141

The nature of the intermediate product may be determined by noting that the first weight loss of 17.23% at 650 °C corresponds to $CO_{1.75}$. The intermediate compound could therefore be mixed phases of oxides represented by the formula [$Li_2Mn_2O_{4.25}$]. Equation 7.5 summaries the overall reaction in nitrogen.

$$Li_2CO_3 + Mn_2O_3 \xrightarrow{N_2,\Delta} Li_2Mn_2O_{4.25} \xrightarrow{N_2,\Delta} 2LiMnO_2 \qquad 7.5$$

Reacting the same mixture in air showed completely different behaviour. From Figure 7.2 it can be seen that the first weight loss of 15.34% completes at about 600 °C. This is followed by a slight weight gain of about 0.25% between 600 and 750 °C. Increasing the temperature beyond that showed a gradual weight loss up to around 950 °C where a sudden weight loss of 4.2% takes place. The sample showed no further degradation up to 1200 °C. The total weight loss for the reaction is about 20.32%. Obviously, the reaction in air is more complex as the involvement of oxygen in the region between 600 and 900 °C changes the weight behaviour recorded on the thermal analyser. The initial weight loss of 15.34% corresponds to the loss of $CO_{1.5}$ produced an "oxygen rich" intermediate oxide. The second weight loss of 4.2% achieved by heating the mixture beyond 1000 °C corresponds to the loss of more oxygen to form $Li_2Mn_2O_4$. The intermediate compounds formed between 600 and 900 °C will probably be a mixture of interchanging phases due to the dynamic nature of the reaction with oxygen. Therefore the overall reaction could progress as described in Equation 7.6.

$$Li_2CO_3 + Mn_2O_3 \xrightarrow{Air,\Delta} Li_2Mn_2O_{4.5} \xrightarrow{Air,\Delta} Li_2Mn_2O_4 \qquad 7.6$$

In an attempt to understand the nature of the oxides formed during the course of the reaction above, three samples were prepared for the purpose of a snapshot x-ray analysis at three positions: after the first weight loss completes at 600 °C, after the slight weight gain at 750 °C, and finally after the last weight loss at 1200 °C. The x-ray diffraction photographs of the above samples are shown in Figure 7.4. Table 7.3 lists d-values for the diffraction patterns shown in Figure 7.4.

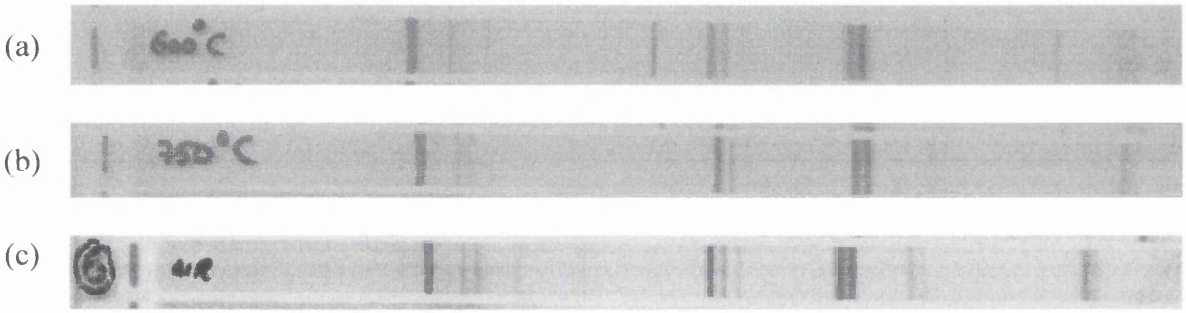

Figure 7.4 X-ray diffraction of Li_2CO_3 + Mn_2O_3 in 1:1 molar ratio heated in air, (a) at 600 °C, (b) at 750 °C, and (c) at 1200 °C.

From Figure 7.4 and Table 7.3, it can easily be seen that there are structural changes taking place during the progress from 600 to 1200°C. There is a similarity between the samples obtained at 600 and 750 °C except for the absence of some lines for the 750 °C sample indicating structural rearrangement as a result of the oxygen uptake noticed on the thermogram between 600 and 800 °C.

Table 7.3 d-values/Å for the Li_2CO_3 + Mn_2O_3 in 1:1 molar ratio heated in air to 600, 750 and 1200 °C.

d-values 600 °C	I	d-values 750 °C	I	d-values 1200 °C	I
4.45	10	4.45	10	4.70	10
4.00	2	4.00	1	4.28	2
3.85	1	3.86	1	4.08*	2
3.61	2	-	-	3.68	1
2.56	5	-	-	3.15	1
2.34	5	2.35	6	2.885	1
2.29	4	2.30	4	2.469*	9
2.23	1	2.25	1	2.430	4
1.95	4	1.950	8	2.370	1
1.915	6	1.920	8	2.067	9
1.785	1	1.790	1	2.038	9
1.750	1	1.760	1	1.896	2
1.570	2	-	-	1.871	1
1.491	2	1.495	2	1.591*	3
1.480	1	1.479	1	1.576	1

On the other hand, the diffraction pattern of the sample prepared at 1200 °C did not fit any of the reported diffraction pattern for $LiMnO_2$ and $Li_2Mn_2O_4$ indicating the formation of a phase that relates the previous phases observed in the other diffraction photographs but with some fundamental structural rearrangement. These changes are shown in terms of the appearance of new diffraction lines and the shift of the lines towards higher d-values.

The oxide prepared at 1200 °C is expected to have a similar diffraction pattern to that of sample obtained at 850 °C under nitrogen as they both have the same mass. The diffraction patterns obviously differ greatly. This could be attributed to the path taken to reach the end oxide $LiMnO_2$. The variation in crystal structure observed here is a confirmation of the sensitivity of the final product to the reaction conditions observed by other researches [3, 5, 6].

An attempt was made to correlate the structures observed at the temperatures above with the known oxides that contain lithium and manganese. For the oxide prepared at 1200 °C, the diffraction pattern shown in Figure 7.4c and its d-values listed in the third column of Table 7.3 can be referenced to an intergrowth of two oxides, Li_2MnO_3 and MnO_2. Most of the lines were confirmed to be due to Li_2MnO_3 when compared to those published in the JCPDS-ICDD File 27-1252. Those values indicated with (*) were linked to the MnO_2 phase by comparison with the values published in the JCPDS-ICDD File 4-0326 for Mn_xO_y. Based on the assumption that most of the sample is monoclinic Li_2MnO_3, the unit cell were calculated to be a = 4.86 Å, b = 8.552 Å and c = 9.456 Å.

As for those oxides produced at 600 and 750 °C, no matches were found in the literature or the JCPDS-ICDD files with the diffraction lines observed. No further attempts were made to analyse these "intermediate" oxide phases.

7.3 Preparation Method with 1:3 Li:Mn Ratio

As mentioned in Table 7.1, the expected results of the reactions with a 1:3 Li:Mn ratio are $LiMn_3O_5$ and $Li_2Mn_6O_{11}$ for the reactions in nitrogen and air respectively.

7.3.1 Experimental

Stoichiometric amounts of Li_2CO_3 and Mn_2O_3 were ball milled using cyclohexane as described earlier. After evaporating the organic solvent, samples of the resulting homogeneous mix were heated to 1200 °C in nitrogen or air while monitoring their weight changes using the Stanton Redcroft thermal analyser. The results of both experiments are shown in Figure 7.5.

7.3.2 Results and Discussion

As expected, the reaction under air exhibited different and more complex behaviour than that under nitrogen. Thus, only the nitrogen experiment will be discussed. As can be seen in Figure 3.23, the first weight change is completed at 700 °C with a loss of about 7.8%, a change which can easily be assigned to the loss of one CO_2 as its theoretical weight percentage is 8%. On further heating, another weight loss of about 3.1% is recorded, a change that appears to result from the loss of one more oxygen from the oxide at 900 °C. The theoretical value of losing one oxygen is 2.92%.

The sample seems to be stable between 850 and 1030 °C, after which a sudden change takes place at 1050 °C and continues gradually to 1200 °C, the limit of the thermal analyzer. The residue of 86% at 1200 °C indicates another weight loss of 3.1% which

would be attributed to loss of an oxygen. The steps that describe the weight changes found for the reaction under nitrogen can be written as in Equation 7.7.

$$Li_2CO_3 + 3Mn_2O_3 \xrightarrow{700\ ^\circ C} 2LiMn_3O_5 \xrightarrow{900\ ^\circ C} Li_2Mn_6O_9 \xrightarrow{1200\ ^\circ C} 2LiMn_3O_4 \quad 7.7$$

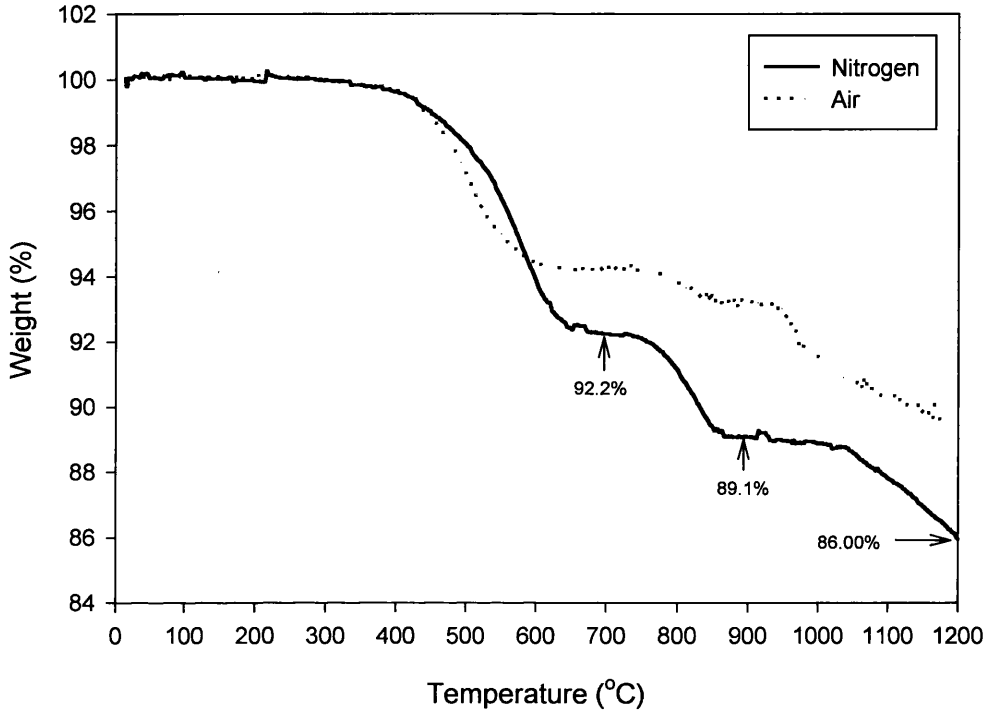

Figure 7.5 TGA traces of reacting Li_2CO_3 and Mn_2O_3 in 1:3 Li:Mn molar ratio in nitrogen and air.

Samples were prepared at 700, 900 and 1200 °C for x-ray examination. Unfortunately, the x-ray photograph was not suitable for reproduction but the d-values were extracted for the three samples above and are listed in Table 7.4 along with that for $LiMn_3O_4$ reported in JCPDS-ICDD File 38-298.

As can be seen from Table 7.4, none of the samples fits those values reported in File 38-298. Thus the products at these three temperatures are not single-phase oxides as predicted by Equation 7.7. Some of the lines could be assigned to known lithium manganese oxides and manganese oxides, but no single or dual phase could be found in any of the diffraction patterns, at least when compared to the known JCPDS-ICDD files. Further investigations into the crystal structures of the resulting oxides are beyond the scope of this thesis.

Table 7.4 d-values/Å for the Li_2CO_3 + Mn_2O_3 in 1:3 molar ratio heated in nitrogen to 700, 900 and 1200 °C along with those for $LiMn_3O_4$.

d-values 700 °C	I	d-values 900 °C	I	d-values 1200 °C	I	$LiMn_3O_4$ 38-298	I
5.80	8	4.90	6	5.80	6	5.01	3
4.90	6	4.75	10	4.90	4	3.095	<1
4.80	4	3.10	4	3.60	1	3.011	<1
3.60	1	2.88	3	3.10	5	2.688	0.3
3.10	6	2.77	8	2.90	3	2.580	0.5
2.90	4	2.5	9	2.77	5	2.503	7
2.77	9	2.36	1	2.56	4	2.253	5
2.53	2	2.07	3	2.37	6	2.129	10
2.50	10	2.03	2	2.30	2	2.005	<1
2.49	1	1.90	1	2.21	1	1.959	<1
2.45	1	1.83	1	2.04	2	1.669	<1
2.40	1	1.80	1	2.02	1	1.642	<1
2.37	3	1.71	2	1.83	2	1.547	5
2.30	4	1.45	1	1.80	1	1.506	3
2.04	4	1.58	1	1.7	1	1.498	3
2.02	6	1.55	2	1.65	1	1.460	0.5
1.83	1			1.58	1	1.442	0.5
1.80	3			1.57	1	1.344	1
1.71	1			1.55	1	1.314	0.4
1.65	1			1.52	1	1.290	2
1.58	2					1.260	2.5
1.55	4					1.252	2.5
1.51	2					1.135	0.4

7.4 Preparation Methods with other Li:Mn Ratios

Other lithium to manganese ratios examined following the same route outlined in this chapter were 2:1 and 3:1. These were chosen to illustrate the effect of increasing the amount of lithium, as opposed to those tried earlier where the amount of manganese was altered.

To achieve the required ratios, stoichiometric amounts of Li_2CO_3 and Mn_2O_3 were ball milled together in presence of cyclohexane for 3 hours. Samples of the mixtures were heated in the presence of nitrogen or air and the behaviour of the reactions was followed using the Stanton Redcroft thermal analyser.

The results of experiments using 2:1 and 3:1 ratios are shown in Figures 7.6 and 7.7 respectively. The recorded weight losses of 26.47% and 32.24% in nitrogen at 1200 °C for 2:1 and 3:1 ratios correspond to the loss of 2 and 3 moles CO_2 respectively. The theoretical values for the loss of 2 and 3 moles of CO_2 are 28.8% and 34.8% respectively.

From Figures 7.6 and 7.7 we can see that the thermograms are dominated by reactions that are taking place over a broad range of temperatures. DSC analysis of those reactions revealed that at least five endothermic steps are taking place between 500 and 1200 °C for experiments carried out under nitrogen and two endothermic steps are taking place between 400 and 1200 °C for experiments carried out in air. Example DSC traces in nitrogen and air for a 2:1 mixture are shown in Figure 7.8.

Regrettably, further investigation into the nature of the oxides produced here and using stoichiometric amounts of lithium and manganese was not possible for technical reasons. Thus, no further attempts to identify any of the oxides were made.

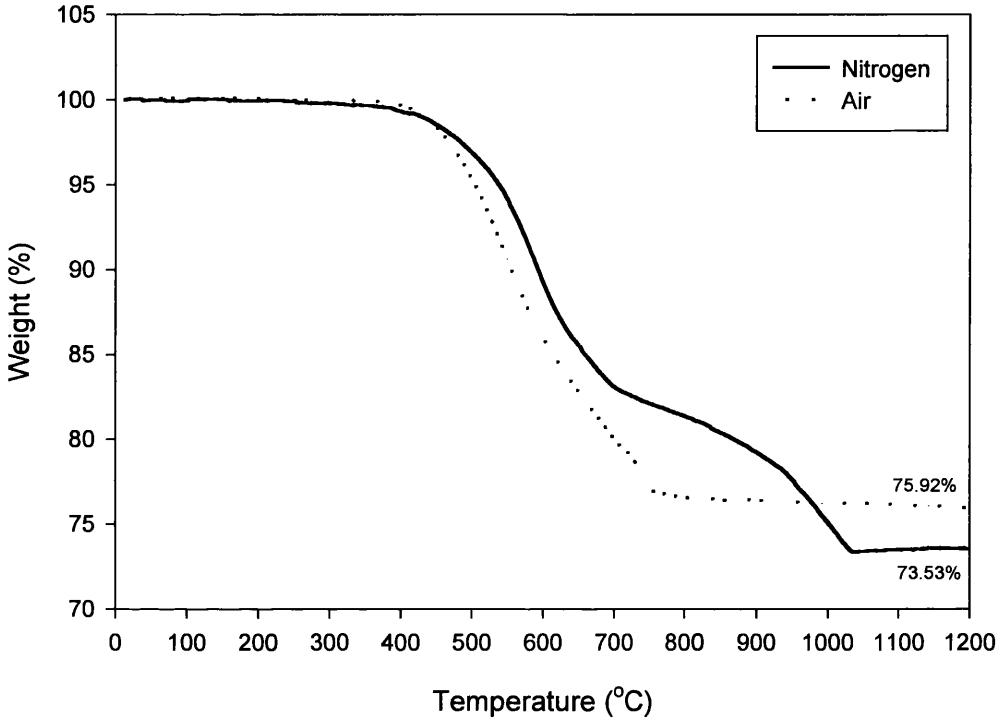

Figure 7.6 TGA traces of reacting Li_2CO_3 and Mn_2O_3 in 2:1 Li:Mn molar ratio in nitrogen and air.

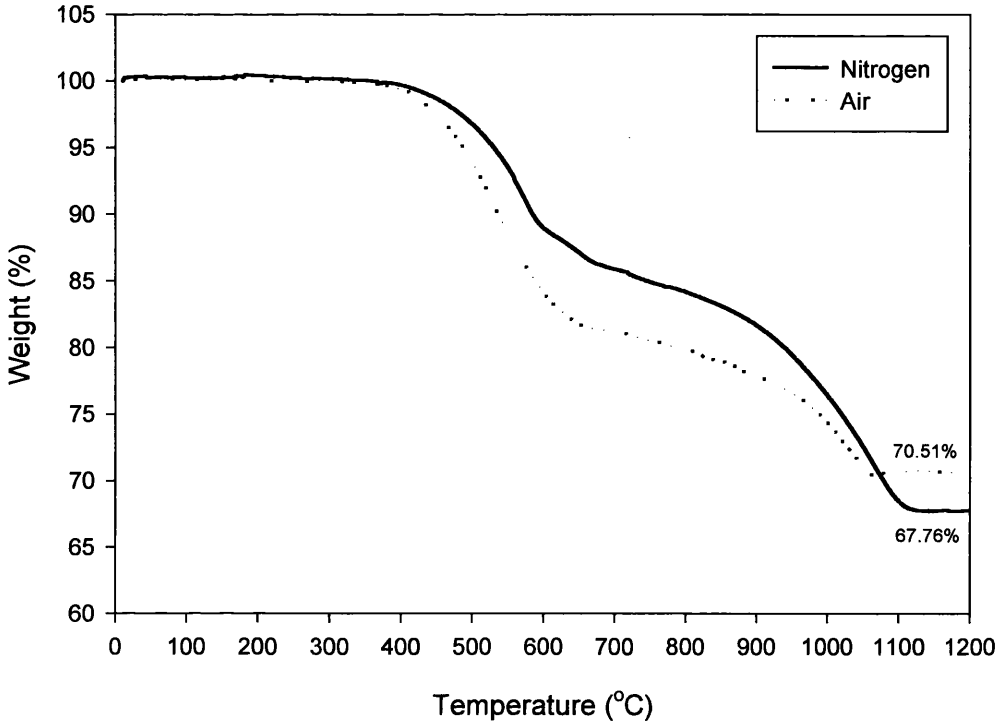

Figure 7.7 TGA traces of reacting Li_2CO_3 and Mn_2O_3 in 3:1 Li:Mn molar ratio in nitrogen and air.

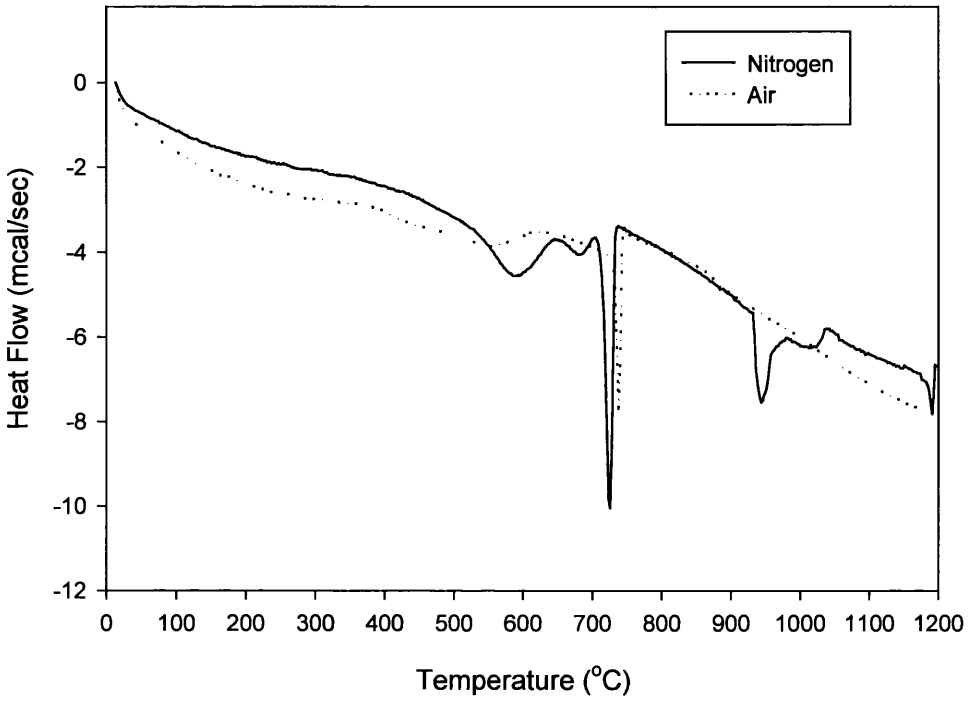

Figure 7.8 DSC traces of reacting Li_2CO_3 and Mn_2O_3 in 2:1 Li:Mn molar ratio in nitrogen and air.

7.5 Conclusion

This chapter described the attempted synthesis and identification of some members of the Li-Mn-O oxide system. The approach taken to achieve the above was to vary the lithium to manganese ration of the reactants Li_2CO_3 and Mn_2O_3. Ratios tried in this work were 1:1, 1:2 (used in Chapter 3), 1:3, 2:1 and 3:1.

A theoretical table was created listing some of the possible paths each ratio of reactants might take in nitrogen and air atmospheres.

Some of the paths suggested by the table were found to be correct and the target oxides were produced and positively identified. The most important one is the synthesis of the electrochemically active orthorhombic $LiMnO_2$ which was synthesized by using a ratio of 1:1.

$LiMnO_2$ is reported to be very sensitive to reaction conditions that might produce the electrochemically inactive phase of the lithiated spinel oxide $Li_2Mn_2O_4$. The oxide prepared using the method described in this chapter has been confirmed by x-ray diffraction analysis to have the orthorhombic unit cell with the dimensions a = 2.790 Å, b = 5.614 Å and c = 4.564 Å.

Other ratios were tried and the products were found to be mixed phases of various lithiated oxides, some of which were in need of more thorough investigation which is outside the scope of this thesis.

References

1 R.J. Gummow. A. DeKock, and M.M. Thackeray, *Solid State Ionics*, **69**, 59 (1994).

2 M.M. Thackeray, W.I.F. David, P.G. Bruce, and J.B. Goodenough, *Mat. Res. Bull.*, **18**, 461 (1983).

3 R.J. Gummow and M.M. Thackeray, *J. Electrochem. Soc.*, **141**, 1178 (1994).

4 J.M. Tarascon and D. Guyomard, *J. Electrochem. Soc.*, **138**, 2864 (1991).

5 T. Ohsuku, A. Ueda, and T. Hirai, *Chem. Express*, **7**, 193 (1992).

6 R.J. Gummow, D.C. Liles, and M.M. Thackeray, *Mat. Res. Bull.*, **28**, 1249 (1993).

7 P. Barboux, J.M. Tarascon, and F.K. Shokoohi, *J. Solid State Chem.*, **94**, 185 (1991).

Conclusion

In this chapter, an overall picture of the work described in this thesis will be drawn.

8.1 Conclusion

The last few years have seen an increase in the research into materials that can be used as electrode materials for lithium rechargeable batteries. Lithium manganese oxides have been given a great deal of attention due to their ease of manufacturing, cost effectiveness, environmental compatibility, in addition to their electrochemical activity [1]. Spinel lithium manganese oxide $LiMn_2O_4$ has been thoroughly investigated since its first preparation by Wickham and Croft in 1958 [2]. Despite all the research effort that has been directed towards the understanding of $LiMn_2O_4$, it still suffers from significant capacity fading upon cycling due to irreversible structure changes and storage losses, especially at high temperature. The effort is reflected by the vast number of ways that have been developed to prepare this oxide [3, 4, 5, 6, 7, 8, 9, 10, 11, 12, 13]. The work in this thesis is part of the effort to shed further light on $LiMn_2O_4$ and its related members of the spinel family.

In Chapter 3, an optimised method to prepare $LiMn_2O_4$ is proposed after a thorough investigation of the original firing technique. The oxide prepared by the new technique was confirmed to be the spinel lithium manganese oxide $LiMn_2O_4$ with a cubic unit cell with lattice constant of a = 8.24 Å. The prepared $LiMn_2O_4$ oxide was found to have a relatively high specific surface area of 7.6 ± 1.3 m^2 g^{-1}, which is desirable as the electrochemical activity is found to be dependent on the specific surface area of the material used in the electrode [14]. Thermal stability studies of the oxide prepared showed that the oxide is thermally stable up to about 700 °C.

Chapter 4 describes the preparation of a novel form of manganese dioxide λ-MnO_2 by the topotactic extraction of lithium from lithium manganese oxide $LiMn_2O_4$. The nature of the product of the extraction reaction was confirmed by x-ray powder diffraction, and the stoichiometry of the oxide has been determined using thermal analysis and found to be $MnO_{1.99}$.

The extraction of lithium was shown to follow a disproportionation mechanism where lithium ions and divalent surface manganese ions are released into solution.

Manganese dioxide λ-MnO_2 has been chemically reduced using cinnamic alcohol. The product of the reduction reaction was a single-phase cubic spinel MnOOH, as confirmed by x-ray diffraction and FTIR spectroscopy. The new phase manganese oxide hydroxide MnOOH was given the name λ-MnOOH to indicate its origin. The composition of the manganese oxide hydroxide was determined using thermal analysis and found to be $[MnO_{1.655}\cdot 0.345\ H_2O]\cdot 0.014\ H_2O$.

In Chapter 5, the kinetics of the extraction of lithium from $LiMn_2O_4$ were investigated. The investigation revealed that the oxidation of the normal spinel $LiMn_2O_4$ by the chemical extraction of Li^+ is a diffusion-controlled process. During the diffusion process, cations are migrating via interstitial sites. In this system, Li^+ is the only diffusing cation and migrates via tetrahedral interstitial sites. The activation energy for the oxidation of $LiMn_2O_4$ was found to be between 22.2 and 28.2 kJ mol^{-1}.

The lithium deficient λ-MnO_2 was originally prepared by extracting lithium ions from $LiMn_2O_4$ using a mildly acidic solution. The extraction of lithium ions is thought to

leave the spinel structure intact and lithium ions can be reversibly introduced back to form $LiMn_2O_4$. In Chapter 6, the possibility of re-inserting lithium into λ-MnO_2 was investigated.

Factors affecting the process e.g. reactants, temperature and length of reaction were determined. It was concluded that lithium could be inserted back into λ-MnO_2 only in the presence of manganese in the solution at room temperature.

In Chapter 7, attempts were described to synthesise and identify some members of the Li-Mn-O oxide system. The approach taken to achieve the above was to vary the lithium to manganese ratios of the reactants Li_2CO_3 and Mn_2O_3. Ratios tried in this work are 1:1, 1:2, 1:3, 2:1 and 3:1.

A method to prepare the electrochemically active orthorhombic $LiMnO_2$ was developed using a mixing ratio of 1:1.

$LiMnO_2$ is reported to be very sensitive to reaction conditions that might produce the electrochemically inactive phase of the lithiated spinel oxide $Li_2Mn_2O_4$. The oxide prepared using the method described in this thesis has been confirmed by x-ray diffraction analysis to have the orthorhombic unit cell with the dimensions a = 2.790 Å, b = 5.614 Å and c = 4.564 Å.

Other ratios were tried and the products were found to be mixed phases of various lithiated oxides and some were in need of more thorough investigation.

References

1 M.M. Thackeray, W.I.F. David, P.G. Bruce, and J.B. Goodenough, *Mat. Res. Bull.*, **18**, 461 (1983).

2 D. Wickham and W. Croft, *J. Phys. Chem. Solids*, **7**, 351 (1958).

3 J.M. Tarascon, E. Wang, F.K. Shokoohi, W.R. McKinnon, and S. Colson, *J. Electrochem. Soc.*, **138**, 2859 (1991).

4 J.H. Lee, J.K. Hong, D.H. Jang, Y.K. Sun, and S.M. Oh, *J. Power Sources,* **89**, 7 (2000).

5 D.G. Fauteux, A. Massucco, J. Shi, and C. Lampe-Onnerud, *J. Appl. Electrochem.*, **27**, 543 (1997).

6 W. Yang, G. Zhang, J. Xie, L. Yang, and Q. Liu, *J. Power Sources*, **81**, 412 (1999).

7 H.B. Park, J. Kim, and C.W. Lee, *J. Power Sources*, **92**, 124 (2001).

8 P. Kalyani, N. Kalaiselyi, and N. Muniyandi, *J. Power Sources*, **111**, 232 (2002).

9 I. Yamada, T. Abe, Y. Iriyama, and Z. Ogumi, *Electrochemistry Communications*, **5**, 502 (2003).

10 W.T. Jeong, J.H. Joo, and K.S. Lee, *J. Alloys and Compounds*, **358**, 294 (2003).

11 M. Nakayama, K. Watanabe, H. Ikuta, Y. Uchimoto, and M. Wakihara, *Solid State Ionics*, **164**, 35 (2003).

12 D. Shu, K.Y. Chung, W.I. Cho, and K.B. Kim, *J. Power Sources*, **114**, 253 (2003).

13 I. Taniguchi, C.K. Lim, D. Song, and M. Wakihara, *Solid State Ionics*, **146**, 239 (2002).

14 G. Pistoia and R. Rosati, *J. Power Sources*, **58**, 135 (1996).

Appendices

APPENDIX I

```
C*      ================================================================
C*      PROGRAM TO CALCULATE THE B.E.T VALUE FROM DATA COLLECTED USING
C*      THE CLASSICAL BET METHOD FOR SURFACE AREA MEASUREMENTS.
C*      JAFAR ALBADRAN  DEPT. OF CHEMISTRY      UW SWANSEA
C*      ================================================================
C*
        DIMENSION VA(10),VB(10),PC(10),PF(10),PSA(10),SPSA(10),V(10)
        DIMENSION PFPO(10)

C*      SETING THE INITIAL VALUES OF PO IS THE VAPOUR PRESURE OF THE
C*      LIQUID FROM THE GAS AT THE TEMPERATURE OF THE COOLING BATHE
C*      AROUND A(76.0 cm Hg). A REPRESENTS THE INITIAL MONOMETER
C*      READING (i) cm. K IS AN APPARATUUS CONSTANT FOR CONVERTING
C*      PRESSURE OF GAS IN cm Hg,AT ROOM TEMPERATURE T, TO VOLUMES OF
C*      GAS, V AT S.T.P. K=273V1/76 T.

        PO=76.0
        A=77.45
        V1=19.80
        T=297.0
        K=0.25
        R=0.0

C*      INTERING THE MONOMETER READINGS AS (II) CM, (III) CM
        PRINT*,' Enter the number of readings =>'
        READ*,N
       DO 100 I=1,N
          PRINT*,'Enter (ii) , (iii)  No.',I
          PRINT*
          READ 4,VA(I),VB(I)

4         FORMAT(2F10.4)
           PC(I)=A-VA(I)
           PF(I)=A-VB(I)
           PSA(I)=VB(I)-VA(I)
           SPSA(I)=PSA(I)+R
           V(I)=0.25*SPSA(I)
           PFPO(I)=PF(I)/PO
           R=SPSA(I)
100    CONTINUE
        PRINT*,'         ~~~~~~~~~~~~~~~~~~~~~~~~~~~~~~~~~'
        PRINT*,' Po = 76.0 cm Hg'
        PRINT*,' (i) = 77.4 cm'
        PRINT*,' V = 19.8 '
        PRINT*,' K = 0.25 '
        PRINT*
      PRINT*,'   (ii)/cm  (iii)/cm    Pc/cm      Pf/cm    Psa/cm
       $SPsa/cm        Vads    Pf/Po '
        PRINT*,'-------------------------------------------------------
       $-----------------------'

       DO 150 I=1,N
          PRINT 10,VA(I),VB(I),PC(I),PF(I),PSA(I),SPSA(I),V(I),PFPO(I)
10        FORMAT(7F10.3,F10.5)
150    CONTINUE
        PRINT*,'-------------------------------------------------------
       $-----------------------'
        STOP
        END
```

APPENDIX II

A program to calculate the BET values using the Single Point Method.

```
C*=====================================================================
C*              PROGRAM TO CALCULATE THE B.E.T VALUE
C*=====================================================================

        DIMENSION VA(20),VB(20),PC(20),PF(20),PSA(20),SPSA(20)
        DIMENSION PFPO(20),XY(20),X2(20),X(20),Y(20),XYA(20)
        DIMENSION YLR(20),YDIFF(20),V(20),PFPOM(20)
        DIMENSION VAT(20),VBT(20),PCT(20),PFT(20),PSAT(20),SPSAT(20)
        DIMENSION VT(20),PFPOT(20)

C*
C*     SETING THE INITIAL VALUES OF PO IS THE VAPOUR PRESURE OF THE
C*     LIQUID FROM THE GAS AT THE TEMPERATURE OF THE COOLING BATHE
C*     AROUND A(76.0 cm Hg). A REPRESENTS THE INITIAL MONOMETER
C*     READING (i) cm. K IS AN APPARATUUS CONSTANT FOR CONVERTING
C*     PRESSURE OF GAS IN cm Hg,AT ROOM TEMPERATURE T, TO VOLUMES OF
C*     GAS, V AT S.T.P. K=273V1/76 T.
C*

        PARAMETER (PO=76.0, A=75.0, V1=19.8, K=0.239)

        DATA N,M,R2/7,10,49.5/
        DATA (VA(I),I=1,7)/70.2,65.6,59.6,54.3,50.4,45.2,39.7/
        DATA (VB(I),I=1,7)/73.8,71.5,68.1,64.3,60.5,56.3,51.6/

        DATA (VAT(I),I=1,10)/50.0,44.8,39.5,35.1,30.2,26.2
     $,20.0,14.6,11.8,5.0/
        DATA (VBT(I),I=1,10)/74.9,74.85,74.80,74.1,73.3,72.2
     $,70.5,68.0,65.1,62.1/


        OPEN (5,FILE='BETLEST.RES',STATUS='OLD')

C*=====================================================================
C*                 INITIALISING THE VALUES
C*=====================================================================

        R=0.0
        S=0.0
        T=0.0
        D=0.0
        U=0.0
        R2=0.0
        S2=0.0
        T2=0.0
        D2=0.0
        U2=0.0

C*=====================================================================
C*      INTERING THE MONOMETER READINGS AS (II) CM, (III) CM
c*=====================================================================
C*
C*        PRINT*,' Enter the number of readings for cal. curve =>'
C*        READ*,N
C*
```

```
C*       DO 100 I=1,N
C*
C*          PRINT*,'Enter (ii) , (iii)  No.',I
C*          PRINT*
C*          READ 4,VA(I),VB(I)
4          FORMAT(2F10.6)
C*
C*       CALCULATING THE Pf ,Pc ,Psa ,SUM Psa ,Vads(E-6) and Pf/Po
C*       FOR THE CALIBRATION CURVE

         DO 100 I=1,N

            PC(I)=A-VA(I)
            PF(I)=A-VB(I)
            PSA(I)=VB(I)-VA(I)
            SPSA(I)=PSA(I)+R
            V(I)=0.25*SPSA(I)
            PFPO(I)=PF(I)/PO

            X(I)=PFPO(I)+T
            Y(I)=V(I)+S
            XY(I)=(PFPO(I)*V(I))+U
            X2(I)=(PFPO(I)**2)+D

            R=SPSA(I)
            T=X(I)
            S=Y(I)
            U=XY(I)
            D=X2(I)

C*       CALULATING THE A AND B VALUES FOR LINEAR REGRRESION EQUASION
C*       Y=A+B*X

            B=(N*U-T*S)/(N*D-T**2)
            AD=(S-B*T)/N

100     CONTINUE


         WRITE(5,*)'              ~~~~~~~~~~~~~~~~~~~~~~~~~~~~~~~~~~'
         WRITE(5,*)' Po = 76.0 cm Hg'
         WRITE(5,*)' (i) = 77.4 cm'
         WRITE(5,*)' V = 19.8 '
         WRITE(5,*)' K = 0.25 '
         WRITE(5,*)
       WRITE(5,*)' (ii)/cm  (iii)/cm    Pc/cm      Pf/cm    Psa/cm
      $ SPsa/cm       Vads    Pf/Po '

1      WRITE(5,*)'-----------------------------------------------------
      $-----------------------'

       DO 150 I=1,N

        WRITE(5,10)VA(I),VB(I),PC(I),PF(I),PSA(I),SPSA(I),V(I),PFPO(I)
10         FORMAT(7F10.4,F10.5)

150    CONTINUE

       WRITE(5,*)'-----------------------------------------------------
      $-----------------------'
       WRITE(5,*)
```

```
c*      WRITE(5,*)' N     SUMX     SUMY     SUMXY     SUMX2    A    B '
c*      WRITE(5,*)
c*      WRITE(5,15)N,T,S,U,D,AD,B
c*  15    FORMAT(I2,6F10.5)
c*      WRITE(5,*)

c*=================================================================
c*       Entering the values for the sample to be calculated
c*=================================================================

C*      print*,'Enter the number of readings for the sample =>'
C        READ*,M
C      print*,'Enter the intial value for SPsa/cm ==>'
C
C        READ*,R2
C        DO 200 J=1,M
C        PRINT*,'Enter (ii) , (iii)  No.',J
C        PRINT*
C        READ 4,VA(J),VB(J)
C
C*   CALCULATING THE Pc , Pf, Psa, SUM Psa ,Vads(E-6) and Pf/Po
C*   THE SAMPLE UNDER TEST

        DO 200 J=1,M

          PCT(J)=A-VAT(J)
          PFT(J)=A-VBT(J)
          PSAT(J)=VBT(J)-VAT(J)
          SPSAT(J)=PSAT(J)+R2
          VT(J)=0.25*SPSAT(J)
          PFPOT(J)=PFT(J)/PO
          R2=SPSAT(J)

200    CONTINUE

C*      CALCULATING LINEAR REGRESION VALUES USING ( Y=A+B*X ) AND
C*      FINDING THE DIFFERENCE BETWEEN THE SAMPLE ISOTHERM AND THE
C*      CALIBRATION CURVE.

        DO 250 J=1,M

            YLR(J)=AD+B*PFPOT(J)
            YDIFF(J)=VT(J)-YLR(J)

C*     SOLVING THE MULILAYER B.E.T. EQUATION,BY PLOTING (Pf/Po-f)/Vads
C*     VIS Pf/Po

           PFPOM(J)=PFPOT(J)/((YDIFF(J))*(1-PFPOT(J)))

250   CONTINUE

        WRITE(5,*)
        WRITE(5,*)'-------------------------------------------------
     $------------------------'
      WRITE(5,*)' (ii)/cm  (iii)/cm     Pc/cm     Pf/cm     Psa/cm
     $  SPsa/cm     Vads    Pf/Po '
       WRITE(5,*)'-------------------------------------------------
     $------------------------'

      DO 300 J=1,M
```

```
       WRITE(5,10)VAT(J),VBT(J),PCT(J),PFT(J),PSAT(J),SPSAT(J),VT(J)
     $,PFPOT(J)

300    CONTINUE

       WRITE(5,*)'-------------------------------------------------'
       WRITE(5,*)'  Pf/Po   Vads(calib.)   Vads(sample)   Vads(diff.)'
       WRITE(5,*)'-------------------------------------------------'

       DO 500 J=1,M

          WRITE(5,7)PFPOT(J),YLR(J),VT(J),YDIFF(J)
7         FORMAT(F10.5,F10.3,3X,F10.3,5X,F10.3)
8          format(F10.5,5X,(E12.5))

500    CONTINUE

          WRITE(5,*)
          WRITE(5,*)'----------------------------'
          WRITE(5,*)' Pf/Po     (Pf/Po-Pf)/Vads  '
          WRITE(5,*)'----------------------------'

C***      open(4,file='bet.dat',status='new')

        DO 600 J=1,M

          WRITE(5,8)PFPOT(J),PFPOM(J)
C***          write(4,8)pfpot(j),pfpom(j)

600    CONTINUE

C*=====================================================================
C*      LEASTSQUARE METHOD TO CALULATE THE SLOPE AND THE INETRCEPT
C*=====================================================================

        SX=0.
        SY=0.
        SX2=0.
        SY2=0.
        SXY=0.

        DO 700 J=1,M

           SX=SX+PFPOT(J)
           SY=SY+PFPOM(J)
           SX2=SX2+PFPOT(J)*PFPOT(J)
           SY2=SY2+PFPOM(J)*PFPOM(J)
           SXY=SXY+PFPOT(J)*PFPOM(J)

700     CONTINUE

        XBAR=SX/M
        YBAR=SY/M
        X2BAR=SX2/M
        Y2BAR=SY2/M
        XYBAR=SXY/M

        U11=XYBAR-XBAR*YBAR
        SIGX2=X2BAR-XBAR*XBAR
        SIGY2=Y2BAR-YBAR*YBAR
```

```
      R=U11/SQRT((SIGX2*SIGY2))
      AA=U11/SIGX2
      B=YBAR-U11*XBAR/SIGX2
      EA=SQRT((SIGY2*(1.-R*R))/(M*SIGX2))
      EB=EA*(SQRT(X2BAR))

      WRITE(5,*)
      WRITE(5,11)AA,EA
11    FORMAT(' Slope=',F10.6,'  Error in slope= ',F10.7)
      WRITE(5,*)
      WRITE(5,6)B,EB
6     FORMAT(' Intercept=',F10.6,' Error in intercept=',F10.7)
      WRITE(5,*)
      WRITE(5,9)R
9     FORMAT( ' Correlation Coefficient=',F9.6)
      WRITE(5,*)

C*    FROM THE SLOPE AND THE INTERCEPT WE CAN CALCULATE THE (VM),THE
C*    QUANTITY OF GAS NEEDED TO COVER THE SURFACE OF THE AMPLE,WHICH
C*    IS CORESPOND TO MONOLAYER OF ADSORBED N2 MOLECULES.

      VM=1/(AA+B)
      WRITE(5,*)'VM= ',VM
      WRITE(5,*)

C*    FROM THE RELATION PV=NRT WE COULD FIND OUT THE NUMBER OF MOLES
C*    OF N2 USED.

      TMOLES=(1.01*(VM/10))/(8.314*298)
      WRITE(5,*)'No. OF MOLES = ',TMOLES
      WRITE(5,*)

C*    TO CALCULATE THE NUMBER OF MOLECULES OF N2 GAS WE MULTIPLY THE
C*    NUMBER OF MOLES BY AVOGADRO NUMBER.

      GASN2=TMOLES*6.023E23
      WRITE(5,*)'No. OF N2 GAS MOLECULES = ',GASN2
      WRITE(5,*)

C*    CALULATE THE TOTAL AREA OF N2 ADSORBED BY MULTIPYING THE UMBER
C*    OF MOLECULES BY THE AREA OCCUPIED BY A SINGLE N2 MOLECULES
C*    LAYER

      AREA=GASN2*1.624E-19
      WRITE(5,*)'THE TOTAL AREA OCCUPIED BY A SINGLE LAYER =',AREA
      WRITE(5,*)

C*    THE TOTAL AREA OF THE SAMPLE SURFACE IN M2/KG

      TOTAL=AREA/1.1831E-3
      WRITE(5,*)'THE SURFACE AREA OF THE SAMPLE IN M2/KG =',TOTAL
      WRITE(5,*)

30    STOP
      END
```

APPENDIX III

A MathCAD program to correct samples' d-values based on d-values of KCl.

```
================================================================
X-ray Correction for the Experimental Values Using KCl as a Standard
J. Albadran Department of Chemistry UWS          10.12.92
================================================================

Sample Name: Lambda=MnO2                    Date: 8/1/1993

================================================================
Enter the experimental d-values for KCl in the first column and d-
values for the Sample in the second column by putting the cursor on
the last value and type (,) and enter the next value. After that,
change the values of i and j depending on the Number of readings.
The third column contains the theoretical values for KCl.
================================================================

I := 0,1 ..5      j:= 0,1 ..7      λ:=1.54050  for CuKα radiation
```

$X_i :=$

3.15
2.225
1.815
1.572
1.408
1.283

$Y_j :=$

4.64
2.43
2.32
2.02
1.85
1.551
1.423
1.360

$\sin^2\Theta lit_i :=$

599.435
1199.472
1799.016
2397.746
2996.935
3598.593

$$H_i := \frac{\lambda}{x_i\, 2} \qquad Hs_j := \frac{\lambda}{Y_j\, 2}$$

$$\Theta 4_i := \lfloor \mathrm{asin}(H_i) \cdot 57.29578 \rfloor \cdot 4 \qquad \Theta 4s_j := \lfloor \mathrm{asin}(Hs_j) \cdot 57.29578 \rfloor \cdot 4$$

$$\sin^2\Theta_i := H_i^2 \cdot 10^4 \qquad delta_i := \sin^2\Theta lit_i - \sin^2\Theta_i$$

$$vs := lspline(\Theta 4, delta) \qquad \mathrm{inter}_j := \mathrm{interp}(vs, \Theta 4, delta, \Theta 4s_j)$$

$$\sin^2\Theta s10_j := \sin\left[\frac{\frac{\Theta 4s_j}{57.29578}}{4}\right]^2 \cdot 10^4 \qquad \sin^2\Theta corr_j := \sin^2\Theta s10_j + \mathrm{inter}_j$$

$$dcorr_j := \frac{\lambda}{2\sqrt{\sin^2\Theta corr_j \cdot 10^{-4}}}$$

$dcorr_j :=$

4.626
2.428
2.319
2.02
1.851
1.552
1.422
1.359

APPENDIX IV

A Computer Program for Diffraction Pattern Analysis

This computer program was constructed to aid the determination of unit cell dimensions from mm, $\sin^2\Theta$ or d-values and to simulate diffraction patterns of compounds when their unit cell dimensions are known. The program generates all (hkl)-values, for mm<180, of a given unit cell. The unit cell must have symmetry which is higher than triclinic, since the program is based on the following equations.

$$mm\ (i.e.\ 4\Theta) = 4\ Sin^{-1}(\sqrt{\sin^2\Theta})\frac{180}{\Pi}$$

$$\sin^2\Theta = \frac{\lambda^2}{4d^2}$$

and $$d = \left[\left(\frac{h^2}{a^2} + \frac{l^2}{c^2} - \frac{2hl\cos\beta}{ac}\right)\frac{1}{\sin^2\beta} + \frac{k^2}{b^2}\right]^{-\frac{1}{2}}$$

Thus with input data of the wavelength of the radiation, λ, and the cell dimensions a, b, and c (in angstroms) and β (in radians), the program will calculate mm, $\sin^2\Theta$ and d-values for (hkl)-values within the limits h=0-10, k=0-10, l=0-10 and 4Θ<180mm.

Program listing

```
c*      master monoclinic system analysis
c*      PUT IN UNIT CELL DIMENSIONS AND LAMBDA IN ANGESTROMS AND
C*      RADIANS.90 DEGREES IS EQUAL TO 1.57089 RADIANS.
C*
1       READ 2,A,B,C,BETA,WL
        IF(A)8,8,0
2       FORMAT (5F10.5)
        DIMENSION D(11,11,11),SIN2THETA(11,11,11),IH(11),K(11),L(11)
        DIMENSION SIN2THETA(11,11,11)
        DIMENSION IH(11),K(11),L(11)
     1,THETA4(11,11,11)
C*      THE FOLLOWING DEFINITIONS ARE TO SHORTEN EXECUTION TIME.
        SB=SIN(BETA)
        SB2=SB*SB
        CB=COS(BETA)
        A2=A*A
        B2=B*B
        C2=C*C
        WL24=WL*WL/4
C* HKL VALUES FROM 0 TO 10 ARE TO BE CALCULATED.
C* H,K AND L TAKE THE VALUE 0, 0 IS NOT ALLOWED AS A SUBSCRIBT THUS:
        DO 3 IHX=1,11
        IH(IHX)=IHX-1
        DO 3 KX=1,11
        K(KX)=KX-1
        DO 3 LX=1,11
        L(LX)=LX-1
C       WHEN H=0,K=0,AND L=0, SIN2THETA IS INCALCULABLE THUS:
        IF(IHX+KX+LX.EQ.3) GO TO 3
        D(IHX,KX,LX)=1./(((((IH(IHX)*IH(IHX))/A2+(L(LX)*L(LX))/C2-2
      1*IH(IHX)*L(LX)*CB/(A*C))/SB2)+(K(KX)*K(KX))/B2)**0.5)
        SIN2THETA(IHX,KX,LX)=WL24/(D(IHX,KX,LX)*D(IHX,KX,LX))
C* BECAUSE THE ARGUMENT OF ASIN MUST BE <1 THUS:
        IF(SIN2THETA(IHX,KX,LX).GT.1.0) GO TO 3
    THETA4(IHX,KX,LX)=ASIN(SQRT(SIN2THETA(IHX,KX,LX)))*4.*180./3.14159
3       CONTINUE
        PRINT 4
4       FORMAT(5X,'H',5X,'K',5X,'L',7X,'D VALUES',7X,'SIN2THETA',6X,
      1 'M4THETA')
        DO 5 IHX=1,11
        DO 5 KX=1,11
        DO 5 LX=1,11
C*      THIS IS INCLUDED TO CUT DOWN UNWANTED DATA PRINT-OUT.
        IF (THETA4(IHX,KX,LX).GT.180.0) GO TO 5
        IF (THETA4(IHX,KX,LX).LE.0.0) GO TO 5
        PRINT 6,IH(IHX),K(KX),L(LX),D(IHX,KX,LX),SIN2THETA
      1(IHX,KX,LX),THETA(IHX,KX,LX)
5       CONTINUE
6       FORMAT (3(4X,I2),2(5X,F10.7),4X,F12.6)
        PRINT*
        PRINT*
        PRINT*
        GO TO 1
8       STOP
        END
```